IOWA STATE UNIVERSITY
Digital Repository

2007

The effect of surface roughness parameters on contact and wettability of solid surfaces

Yilei Zhang
Iowa State University

Follow this and additional works at: http://lib.dr.iastate.edu/rtd

Part of the Electrical and Electronics Commons, and the Mechanical Engineering Commons

The effect of surface roughness parameters on contact and wettability of solid surfaces

by

Yilei Zhang

A dissertation submitted to the graduate faculty

in partial fulfillment of the requirements for the degree of

DOCTOR OF PHILOSOPHY

Co-majors: Mechanical Engineering; Electrical Engineering

Program of Study Committee:
Sriram Sundararajan, Co-major Professor
Gary Tuttle, Co-major Professor
Pranav Shrotriya
Vikram L. Dalal
Scott Chumbley

Iowa State University

Ames, Iowa

2007

UMI Number: 3274876

UMI®

TABLE OF CONTENTS

iv

ABSTRACT

Surfaces of materials strongly affect functional properties such as mechanical, biological, optical, acoustic and electronic properties of materials, particularly at the micro/nano scale. Surface effects stem from the interplay of surface morphology and surface chemical properties. This dissertation focuses on 1) modeling the effect of surface roughness parameters on solid-solid contact and solid-liquid interaction as well as; 2) developing a surface engineering method that can generate random surfaces with desired amplitude and spatial roughness parameters for tribological and biomimetic applications.

Autocorrelation length (ACL) is a surface roughness parameter that provides spatial information of surface topography that is not included in amplitude parameters such as root-mean-square roughness. A relationship between ACL and the friction behavior of a rough surface was developed. The probability density function of peaks and the mean peak height of a profile were given as functions of its ACL. These results were used to estimate the number of contact points when a rough surface comes into contact with a flat surface, and it was shown that the larger the ACL of the rough surface, the less the number of contact points. Based on Hertzian contact mechanics, it was shown that the real area of contact increases with increasing of number of contact points. Results from microscale friction experiments (where friction force is proportional to real area of contact) on polished and etched silicon surfaces are presented to verify the analysis.

A versatile surface processing method based on electrostatic deposition of particles and subsequent dry etching was shown to be able to independently tailor the amplitude and spatial roughness parameters of the resulting surfaces. Statistical models were developed to connect process variables to the amplitude roughness parameters center line average, root mean square and the spatial parameter, autocorrelation length of the final surfaces. Process variables include particle coverage, which affected both amplitude and spatial roughness

parameters, particle size, which affected only spatial parameters and etch depth, which affects only amplitude parameters. The autocorrelation length of the final surface closely followed a power law decay with particle coverage, the most significant processing parameter. Center line average, root mean square followed a nonlinear relation with particle coverage and particle size. Experimental results on silicon substrates agreed reasonably well with model predictions.

This same hybrid surface engineering process was used to demonstrate adhesion and friction reduction. Microscale adhesion and friction tests were conducted on flat (smooth) and processed silicon surfaces with a low elastic modulus thermoplastic rubber (Santoprene) probe that allowed a large enough contact area to observe the feature size effect. Both adhesion and friction force of the processed surfaces were reduced comparing to that of the flat surfaces.

The process is also used to generate superhydrophobic engineering surfaces by mimicking the structure of lotus leaves. Tunable bimodal roughness (in both micro and nano scale) and a thin hydrophobic fluorocarbon film were generated on an engineering material surface by the hybrid process. These surfaces exhibit contact angles with water of more than 160º. A geometric model was developed to related air-trapping ability of hydrophobic surfaces with hillock features to process variables (hillock diameter, etching depth and coverage) and contact angle. The model is shown to be able to predict minimum coverage of hillocks required for air-trapping on hydrophobic rough surfaces. The model predictions agree with experimental observations reasonably well. This model can particularly be extended to utilizing statistical roughness parameters to predict air-trapping for rough hydrophobic surfaces.

CHAPTER 1. INTRODUCTION

Research background

A surface can be considered to be the transforming region from one material state to another. There are three common material states, solid, liquid and gas. Theoretically, a material surface is comprised of just several outermost atomic layers of the bulk. Solid surface properties can be categorized as both physical and chemical properties. Physical properties are those properties that do not depend on atomic elements, for example, surface morphology, which only depends on atomic arrangement. On the other hand, surface chemical properties depend on the elements, for example, surface energy, which is higher for silicon than that for wax.

Due to unbalanced atomic forces, surface atoms have more energy than bulk atoms, and react more readily with the environment. Atoms in surface layers are relaxed and arranged differently from the bulk to minimize energy. In addition, contaminations can also cause changes in surface morphology. In ambient conditions, atoms in surface layers are always physically and chemically changed by environment, for example, through oxidation and adsorption and hence experiments may often be conducted under high vacuum.

In manufacturing processes, surface morphology can be affected by many sources, for example, inaccuracies in the machine tools, deformation under cutting forces, vibrations of the machine or workpiece, which will lead to irregularity in millimeter scale; and rupture of the material during the chip removal, which will cause micro scale irregularity. In other words, surface morphology is scale dependent. In many engineering applications, it is convenient to categorize surface morphology as surface roughness, waviness and lay at the micrometer, millimeter and meter scale respectively, as shown in Fig. 1. In the nanoscale (nanometer scale), surface roughness is associated with atomic structure, where the location of a single atom is important. Surface morphology strongly affects surface phenomena, for

example, friction, adhesion, contact angle, photon absorption and light reflection. Research areas in which roughness plays a prominent role range from quality assurance, tribology (friction, lubrication and wear), biomechanics, hydrodynamics, to oceanography and selenology[1,2].

This thesis will focus on surface roughness of solid materials and its effects on solid-solid and solid-liquid interactions in ambient conditions. First, surface roughness is described using statistical roughness parameters and the effect of a spatial roughness parameter, autocorrelation length on contact and friction behavior is analyzed, via a statistical contact
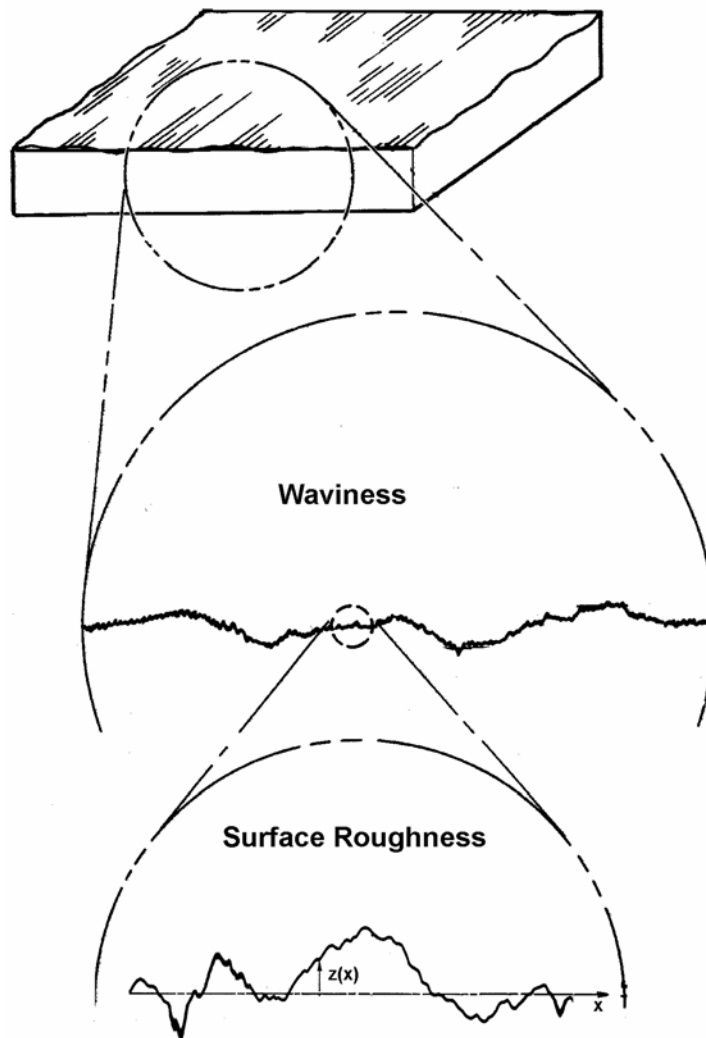
Figure 1. Illustration of self-affine property of surface roughness

model. Then, a novel hybrid surface processing method that combined electrostatic deposition and plasma etching is described that can generate random surfaces with desired spatial and amplitude roughness parameters. This process is shown to generate surfaces with reduced adhesion and friction. Finally, the hybrid processing method and statistical modeling of surface morphology was used in the study of hydrophobic rough surface wetting. In the following sections, the current state in surface roughness modeling, surface micro/nano patterning and surface wetting will be reviewed.

Surface roughness modeling

Roughness measurement

Roughness modeling starts from the measurement of height variation of profiles (one-dimension, 1D) or surfaces (two-dimension, 2D). Generally the measured height data are in discrete format and the distance between two data points (sampling distance) is constant. Profiles are easier to measure and many surfaces are generated from parallel profiles. Stylus instruments are widely used in profile measurements. Over the last decade, micro/nanoscale roughness measurements are performed using scanning probe microscopy (SPM) due to its high resolution[1]. The basic principle of these instruments is similar: a probe scans along a profile and its interactions with the substrate are recorded and analyzed to obtain profile height information. The interactions may be contact forces for many stylus instruments and atomic force microscopy; or tunneling current for scanning tunneling microscopy. Resolution of profile height measurement depends on probe size, which is usually in the micron-millimeter scale for stylus instruments and in the nano- to microscale for SPM. There are also some other measuring methods, for example, optical methods, which may apply geometrical optics or physical optics; contact methods, electrical methods, and fluid methods[2].

Due to the finite nature of the probe size, it may not be able to follow irregularities that are separated by a distance smaller than the probe size. This means that the measured

irregularities have a small wavelength cut-off. This lower limit may also be introduced when analog signals are sampled into digital signals. On the other hand, the total length of measurement is the large wavelength cut-off. This means that the measured irregularities are actually sampled signals from a profile by a band pass filter, whose higher frequency limit and lower frequency limit are decided by instrument and scanning length respectively. The appropriate selection of the two limits should be based on the application, for example, friction study of a large industrial bearing may only need a high frequency limit of surface roughness at the micron scale while friction study of a microfabricated bearing requires a much larger high frequency limit of surface roughness, which may be beyond the capability of a common stylus instrument.

Roughness parameters

The modeling of profile roughness starts from the definition of a mean line, which is parallel to the geometrical profile such that the area of solid above it is equal to the area of void below it (as the dot-dashed line shown in Fig. 2). Roughness parameters can be divided into average roughness parameters, statistical parameters, random process parameters and fractal parameters. The two widely used average roughness parameters are centre line average (CLA, R_a) and root mean square (RMS, R_q). These parameters are calculated only based on measured data set. If a distribution function of height data can be obtained, for example, estimated from the histogram of measured data, statistical roughness parameters can be defined, such as bearing area curve, skewness and kurtosis. Both skewness and kurtosis are measures of inefficiency in a statistical sense, which means their values are sensitive to both effects of surface properties and sampling artifact. Further, if the sequence of measured data points is considered (i.e. profiles or surfaces are treated as a 1D or 2D random process), stochastic parameters such as autocorrelation length (ACL) and a structure function can be defined, which provide spatial information of roughness.
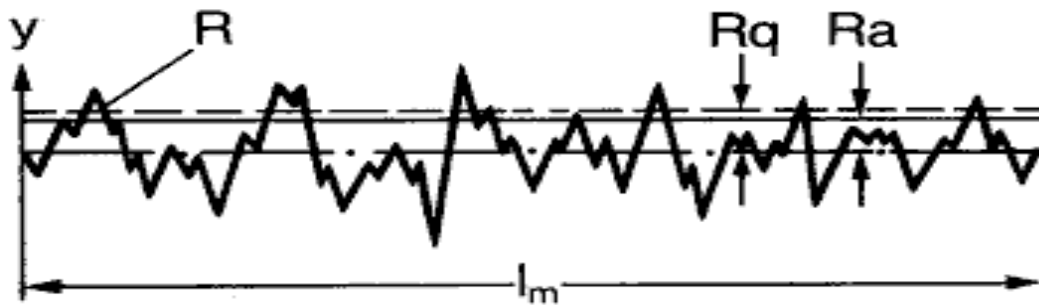
Figure 2. A 1D profile with its mean line shown as the dot-dashed line.

Since roughness is scale dependent, roughness parameters based on measured data are also scale dependent. This makes it impossible to compare roughness parameters without knowing scale information, for example, sampling distance. Fractal methods provide scale-independent roughness parameters such as the fractal dimension and Hurst exponent, by assuming surface morphology is self-affine[3]. However this assumption is not true because engineering surfaces cannot be self-affine in all scales[4].

Roughness parameters can also be divided into amplitude parameters and spatial parameters based on what information they can provide. Amplitude parameters focus on height information, such as CLA, RMS, skewness and kurtosis. Spatial parameters provide lateral information, for example, peak density, zero crossing density and ACL. Compared to amplitude parameters, the effect of spatial parameters on engineering applications, for example, tribology, is not obvious, thus they are not well studied.

The study of spatial parameters are often based on correlation function and sampling distance. Longuet-Higgins (1957) studied a random, moving surface, which was assumed to obey Gaussian distribution and be isotropic. There is no limitation on the form of correlation function, but the energy spectrum was assumed to be circular symmetry about the origin. Furthermore, if the spectrum has predominantly one wavelength, a number of statistical properties of the random surface, for example, the average density of maxima per unit area, can be obtained as functions of the wavelength in simplified forms[5]. Whitehouse and Archard

(1970) showed that the waveform of a random signal can be completely defined by two parameters: its height distribution and its autocorrelation function. Then the statistical distribution of asperities' heights and curvatures were given based on this representation, which can be used to study surface contact[6]. Whitehouse and Philips (1978) used discrete random process analysis to express tribological parameters in terms of just two points on the measured autocorrelation function and the RMS value of the surface with the relaxation that autocorrelation function can have a general form[7]. Whitehouse, Philips (1982) extended their analysis to 2-D surfaces which can be expressed in terms of between four and seven points on the autocorrelation function depending on the type of surfaces[8]. The nature and magnitude of the difference between results from the discrete analysis and those from continuous theory was discussed in details. Greenwood (1984) predicted the properties of the peaks and summits of a rough surface based on the assumption that the surface is two-dimensional random noise and found the predictions in non-dimensional form dependent only to a minor degree on the surface parameters while the absolute values are strongly dependent on the sampling interval[9].

Contact models

Solid-solid contact is very common in mechanical and electrical systems, for example, rolling bearing, and electrical switch. For rough surfaces, the real area of contact is much smaller than the nominal area of contact as shown in Fig. 3. The reduction of contact area affects friction, adhesion, wear and other tribological phenomena as well as electrical conductivity. The real area of contact is not only a function of surface roughness, but also a function of applied normal load. For elastic contact, real area of contact increases with an increase of normal load.
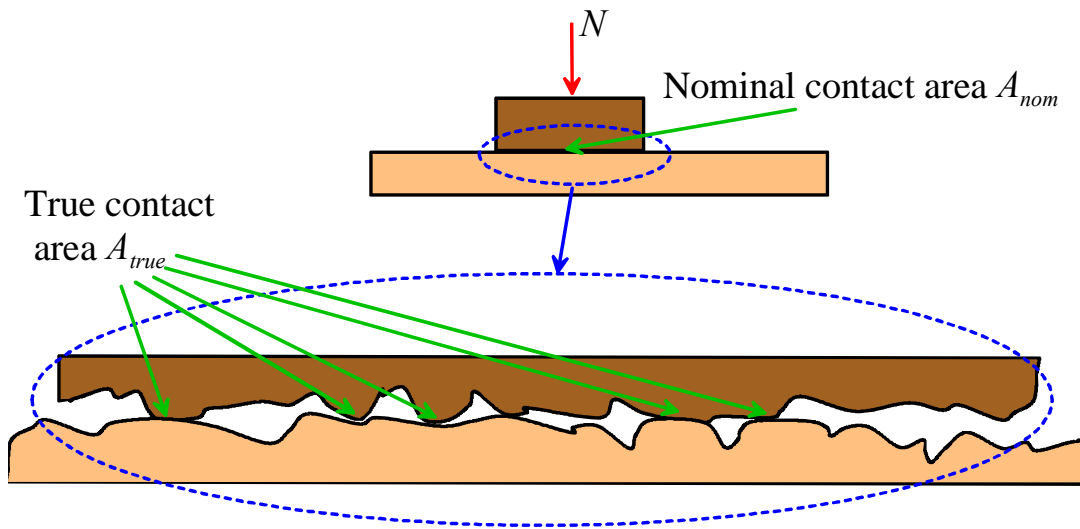
Figure 3. The real area of contact is much smaller than the nominal contact area.

One early developed model of contact mechanics is the Hertzian model, which is restricted to frictionless surfaces and perfectly elastic solids[10]. Based on Hertzian mechanics, several models have been developed by releasing its restrictions, for example, the inclusion of lateral forces and the introduction of plasticity and viscoelasticity. During the study of adhesion forces between rubber and substrates, surface energy was introduced to explain the finite size of contact area at zero normal load, which is the Johnson-Kendall-Roberts (JKR) theory[10]. As pointed by Tabor, JKR theory ignored attractive forces outside the contact area. Derjaguin, Muller and Toporov developed a contact model, which assumed that molecular forces act in a ring-shaped zone around the contact area and decrease quickly[10]. The shortcoming in DMT theory is the neglect of the deformation due to attractive forces close to the edge of the contact area. By analogy to fracture mechanics, Maguis et al. showed that JKR theory is consistent with linear elastic fracture mechanics; then showed the analytic formulae of the JKR-DMT transition[10].

For contact of two rough surfaces, it was shown that this case can always be approximated to the contact of a flat surface with a rough surface with small errors. Then, the

contact of a rough surface with a flat surface could always be studied as the contact of lots of smooth spheres (peaks on the rough surface) with a flat surface. From contact mechanics models, the relation between normal load and contact area of a smooth sphere and a flat surface could be obtained. The summation of normal load and contact area for every single sphere forms the macro load and macro real area of contact. Depending on the definition of surface peaks and treatment of peaks distribution and shape, there are lots of models to describe the macro relation between load and real contact area. Here we only review elastic contact models based on stochastic roughness parameters, particularly RMS and ACL.

Greenwood and Williamson assumed a statistical amplitude distribution function (Gaussian, exponential or others) of surface peaks and a constant radius of peak curvature[11]. Thus the total real area of contact at a given intersection of the rough surface into the flat surface can be calculated from the peak amplitude distribution. For Gaussian amplitude distribution, the density function depends on the RMS of surface roughness. Their simulated results showed a good linear approximation between applied normal load and real area of contact, which agrees with Amontons' law. After that, more complex models have been developed based on the Greenwood-Williamson (GW) theory by treating peaks as ellipsoids, or by introducing a distribution of peak size[3]. Whitehouse and Archard assumed a normal distribution and an exponential form ACF of surface heights. Then using 3-points peak definition, the amplitude distribution function of surface peaks can be written as a function of ACL. Following the same procedure of GW theory, the real area of contact can be derived. In the Whitehouse and Archard theory, curvature of peaks is a variable[6]. Nayak assumed that the surface heights, slopes and curvatures possess a multi-Gaussian probability density and derived the statistical peak distribution based on surface amplitude moments[12].

All the above models assumed isotropic surface morphology. For anisotropic Gaussian surfaces, Longuet-Higgins[5] developed a general description and the corresponding anisotropic surface contact model based on this general description is very complicated.

Bush[13] considered a simplified case with a pronounced grain in one direction and presented a theoretical analysis of the contact of such surfaces. In the following, we will only consider the isotropic surfaces.

From the above literature review on surface roughness modeling, it is clear that amplitude roughness parameters, particularly RMS, are widely used and accepted in surface characterization and tribological study. On the other hand, spatial roughness parameters, such as ACL, has been included in Whitehouse and Archard's model, but not widely applied in engineering applications, partly because relating ACL to real area of contact or surface forces is non-trivial. Thus it is worthwhile to develop a simplified contact model that can reveal the importance of ACL on surface characterization and engineering applications.

Surface micro/nano structure modification

Manufacturing processes have a profound effect on the surface roughness of the final material and can hence impact the surface-related behavior of the material. Experimental and analytical models have been developed to predict surface roughness for some manufacturing processes, for example hard turning and grinding[14,15]. There is also classification of manufacturing processes based on ranges of surface roughness parameters that result (for example, RMS, as shown in Fig. 4). Surface roughness could be formed during removing materials, adding materials or rearrange materials. Here we will review some surface processing techniques according to the three categories.

Material removing processes

Grinding, lathing, laser machining and top-down microfabrication techniques generate surface by removing materials. There are many sources that contribute to surface roughness formation during material removing, for example, rupture of materials, vibration or random errors during processing.

Grinding is a very common machining process, which utilizes lots of small hard particles to scratch on a material surface. Because particle size and shape are random and material remove by a single particle is also random, the generated surface morphology is a summation of many independent random variables. From Central Limit theory, we know that height distribution of ground surfaces should follow Gaussian function. By using ideal conic

Former designations of surface roughness	Arithmetical mean roughness Ra	0.025	0.05	0.1	0.2	0.4	0.8	1.6	3.2	6.3	12.5	25	50	100
	Maximum peak Ry Rmax.	0.1 −S	0.2 −S	0.4 −S	0.8 −S	1.6 −S	3.2 −S	6.3 −S	12.5 −S	25 −S	50 −S	100 −S	200 −S	400 −S
	Standard values of standard length (mm)	0.25				0.8			2.5		8		25	
	Triangular indication	▽▽▽▽				▽▽▽			▽▽		▽		−	

Working method	0.025	0.05	0.1	0.2	0.4	0.8	1.6	3.2	6.3	12.5	25	50	100
Forging								Precision					
Casting								Precision					
Die casting								————					
Hot rolling								————					
Cold rolling				————									
Drawing								————					
Extruding								————					
Tumbling			————										
Sandblasting								————					
Rolling					————								
Face cutter grinding							Precision						
Planing								————					
Carving (Slotting)								————					
Cutter grinding							Precision						
Precision boring					————								
Filing							Precision						
Round grinding				Precision			Fine		Medium		Rough		
Boring							Precision						
Drilling									————				
Reaming						Precision							
Broach grinding						Precision							
Shaving								————					
Grinding			Precision	Fine			Medium		Rough				
Hone finishing			Precision										
Super finishing		Precision											
Buffing			Precision										
Paper finishing			Precision										
Lapping		Precision											
Liquid honing			Precision										
Burnishing				————									
Surface rolling				————									
Electric discharge carving								————					
Wire cut electric spark								————					
Chemical polishing						Precision							
Electrolytic abrasion		Precision											

Figure 4. Classification of processing methods based on CLA range of generated surfaces.

grains, ground surfaces have been modeled as a function of wheel microstructure, process kinetic conditions and material properties[15]. But it is hard to tune those parameters in order to generated random surfaces with desired roughness parameters.

Laser micromachining is another powerful surface processing techniques, which could be applied to glass, ceramic, titanium and other materials that are hard to process with traditional machining techniques, like grinding. The interaction between laser beam and material is complex and we will only consider thermal effects. By adsorbing laser energy, material around focus point is heated up and evaporated. There will be debris formed from melted material or sputtering. Thermal shock and other thermal effects may cause surface morphology change too. Thus generated surface roughness depends on both material and laser properties and is hard to control. Laser micromachining is a sequential process and not suitable for large surface processing.

Chemical and physical etching is widely used in the semiconductor industry as well as in fabrication of microelectronic mechanical systems (MEMS). These processes have the ability to generate micro/nano scale surface structures. Many generated micro/nano patterns using photolithography are periodic because those processes are designed to generate a batch of identified structures. Periodic patterns are different from surface roughness because they are not random and they are designed to achieve certain functions.. Because the selection of surface roughness scale depends on the application, sometimes microfabricated periodic patterns are still treated as surface roughness for macro applications, for example the study of texture effects on lubrication.

The nanoscale or atomic scale roughness could be generated by removing atoms one by one. During chemical etching, etchant reacts with atoms on surfaces and the generated new compounds are removed by fluid or vacuum. Thus the arrangement of atoms on surfaces and the exposure of atoms to etchant as well as etchant density could affect the formation and remove of new compounds. Anisotropic etching could be achieved on crystal because of

different atomic density in different directions. Hydrogen bubbles generated during KOH etching of silicon were believed to cause pyramid formation on etched surface because they can block etchant in certain direction[16]. During physical etching, ion or electron bombarded onto a surface and kick out atoms on the surface. The removing process is random and the generated surface is random too. Certainly physical and chemical etch could be combined into one process, for example, reactive ion etch, where physical bombardment of electrons assists the chemical reaction. Generally it is hard to tune spatial roughness structures because the difficulty to control etchant position.

Material adding processes

Electroplating, thin film deposition and other bottom-up techniques form surfaces by adding materials. Atomic flat surface can be generated by well controlled deposition process, such as atomic layer deposition (ALD). During ALD, precursors are separated from the substrate throughout the coating process and film growth is self-limited and based on surface reactions. This helps remove pin-hole and avoid grain formation.

In many other thin film deposition techniques, such as chemical vapor deposition (CVD), or physical vapor deposition (PVD), there are so many precursors available that pin-hole or grains are always formed on the substrate. By controlling temperature, gas supplement rate and other conditions, grain size and surface morphology can be varied. Electroplating is a process that can coat an electrically conductive object with metals using electrical current to improve its abrasion and wear resistance, corrosion protection and other properties. It is also used to deposit solder bumps in flip-chip packaging and surface roughness can be reduced by an addition of a surface active agent[17]. But generally the variation of surface morphology by deposition is very limited because deposition processes are slow and lack of precise control in spatial structures.

Similar to electroplating, electrostatic deposition uses electrostatic force to hold molecules (particles) onto the oppositely charged substrate. This step can be repeated to form multi-layer coating as long as the negative charged coating and the positively charged one can be added. In general, this multi-layer coating process is called layer-by-layer (LbL) deposition, where other kind of holding forces can be used, for example, hydrogen-bonding[18]. Surface morphology of coated surfaces depends on molecule (particle) shape, defects formation during deposition and interactions among molecules (particles)[18]. Surface morphology can be controlled by varying molecular type, geometry, environment and molecular interactions[18]. But electrostatic force is not strong enough to hold large particles, thus the modification of surface morphology may not be very useful in real applications.

Molding techniques

Materials may be reorganized to form new surfaces, for example, by heating and cooling, chemical reactions. Inject molding is widely used in industry to obtain plastic and metal parts, where molten materials are injected at high pressure into a mold and separated from the mold after cooling. Surface morphology of injection molding of thermoplastic polymers generally depends on polymer crystallinity, crystal structure and dimensions controlled by the molding process[19]. PDMS micromold techniques utilize polymer solidification to generate solid surfaces. The control of generated surface roughness is difficult.

Although there is a large range of processes across scales that can be used to vary the final roughness of a material, in general the level of control is very small. In addition, there appears to be a lack of ability to tune both amplitude and spatial roughness parameters independently and precisely.

Wetting

Similar to solid-solid contact, wetting is the contact between solid and liquid. Liquid may form a droplet or spread on the solid surface depending on the interfacial properties, such as solid surface roughness, surface energy and liquid surface tension. Currently understood effects of surface roughness on the formation of droplet on a solid surface will be described next.

Superhydrophobicity

Contact angle is the primary measurement to determine wettability, which measures the angle between the solid surface and the surface of a liquid droplet on the surface, as shown in figure 6. When a surface shows a contact angle less than 90° with water, it is considered to be hydrophilic surface; otherwise, it is considered to be a hydrophobic surface. Particularly, when contact angle is larger than 150°, the behavior is termed to be superhydrophobic (super-water repellant). Superhydrophobic surfaces are found in nature on the leaf surfaces of many plants such as the lotus and colrabi[20]. These surfaces also exhibit self-cleaning capability by which rolling water droplets remove dirt and debris from their surfaces.
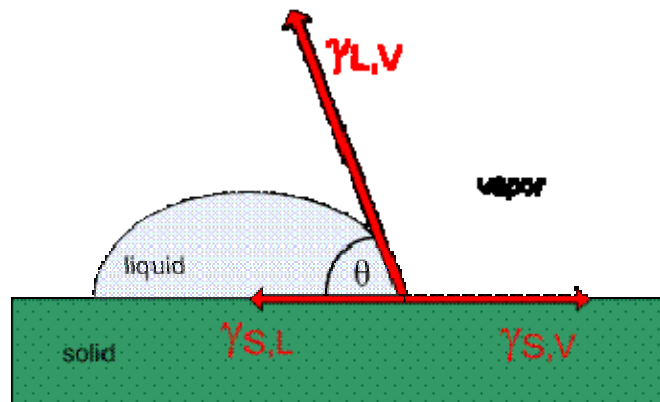

Figure 6. Illustration of contact angle.

Contact angle modeling on rough surfaces

The wetting behavior of superhydrophobic surfaces is governed by both their chemical composition and geometric microstructures. The relation between contact angle and surface energy was developed by Thomas Young[21], which could be written as $\gamma_{LV} \cos \theta = \gamma_{SV} - \gamma_{SL}$, where θ is contact angle, γ_{LV}, γ_{SV} and γ_{SL} are interfacial energy for liquid-vapor, solid-vapor, and solid-liquid respectively. Obviously, no surface roughness effect was considered in Young's equation.

Considering that surface roughness increases the interfacial area between solid and liquid, Wenzel proposed a correction factor r for contact angle on rough surfaces, which is equal to the ratio of rough interfacial area over flat interfacial area under the droplet[22]. The equation is as the following: $\cos \theta^* = r \cos \theta$, where θ^* and θ are contact angle of a droplet on a rough surface and contact angle of the same droplet on the same surface without roughness that is calculated using Young's equation.

Wenzel's model assumes no air-trapping under droplet, which may not necessary be true. Cassie and Baxter[23] built another model to estimate contact angle on rough surface with air-trapping based on the one calculated using Young's equation without considering roughness and air-trapping. He also created an area ratio ϕ_S of liquid-air interface to the whole interface. The equation could be written as the following: $\cos \theta^* = -1 + \phi_s (1 + \cos \theta)$, where θ^* and θ are contact angles with and without considering air-trapping.

Both Wenzel's model and Cassie and Baxter's model use area ratio as correction factor for contact angles, which are not standard surface roughness parameters and not provided in surface characterization. And they did not provide a criterion to predict whether air-trapping could be formed. Thus, it is important and necessary to develop a criterion that can evaluate air-trapping ability of hydrophobic rough surfaces and correct contact angle based on common roughness parameters, such as RMS, ACL, etc..

Preparing methods of superhydrophobic surfaces

Nature serves as a good guide to obtain superhydrophobicity. Several methods have been employed to generate engineering surfaces that can mimic the structure and chemistry of natural superhydrophobic surfaces [24]. Polymer coatings or layer-by-layer deposited particles with both low surface energy and micro structures can be attached to the bulk to achieve superhydrophobic properties[25-30]. Microfabrication techniques are widely used to generate predetermined micro roughness while aligned carbon nanotubes have been utilized for nano scale roughness [31,32]. Since many engineering materials are hydrophilic, a further step is needed to coat the roughened substrates with a hydrophobic layer self assembled monolayers [33], polymer films[34] or diamond-like carbon films[35]. It is of interest to develop processing methods that allow a high degree of control over the resulting surface structure and that can simultaneously impart hydrophobicity to render a material superhydrophobic.

Objectives, research plan and thesis organization

The objectives of this research are (a) to obtain a better understanding of the effects of surface spatial roughness on solid-solid contact, particularly including real area of contact, friction and adhesion; and (b) to develop a micro/nano surface processing techniques that can generate random surfaces with desired spatial and amplitude roughness parameters; and (c) to generate superhydrophobic surfaces and model effects of surface roughness on air-trapping. The overall research plan to achieve these objectives is shown in Fig. 7. The rest of this thesis is organized according to the research activities performed as outlined below.

To achieve objective (a), Whitehouse and Archard's statistical contact model was used as a starting point to study effects of spatial roughness parameter (autocorrelation length) on peak amplitude distribution; then Hertzian mechanics was used to develop relations between autocorrelation length and surface forces. Chapter 2 covers these research activities
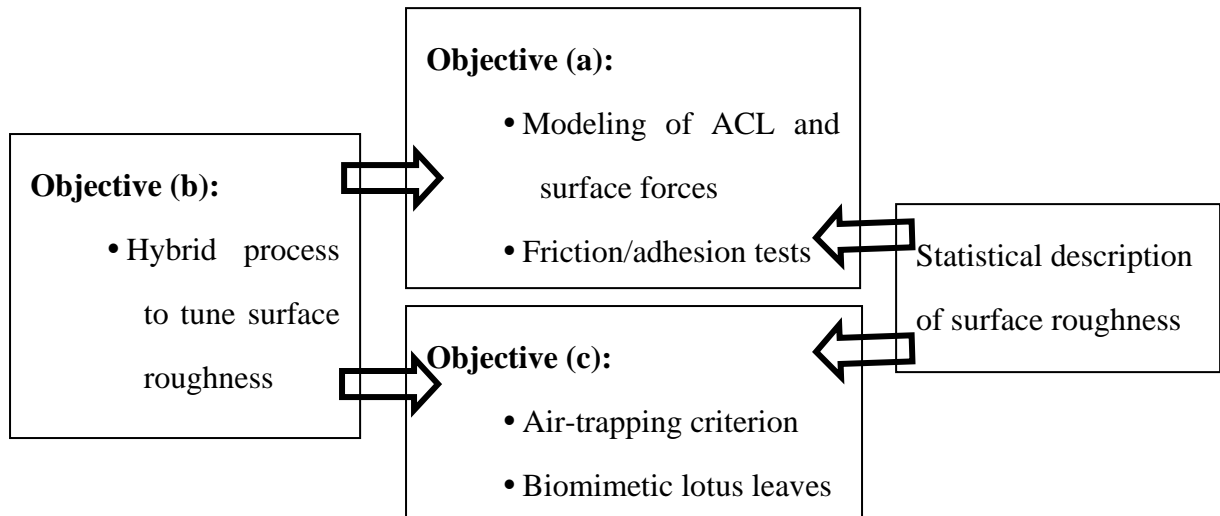
Figure 7. Overall structures of research plan.

in depth. A simplified statistical contact model will be introduced and confirmed with experimental data.

To achieve objective (b), micro/nano fabrication techniques were integrated to develop a novel hybrid process to achieve controlled surface roughness modification. Chapter 3 will discuss a hybrid surface processing method based on electrostatic deposition of colloidal particles and plasma etching, which can tune autocorrelation length of generated surfaces. Special attention was given to generate random patterns based on random deposition of colloidal particles. Generated surfaces were measured to model roughness parameters using process variables. Chapter 4 will show that the developed surface processing method can tune surface amplitude roughness parameters, such as RMS, CLA as well. This process was used to generate surfaces with reduced adhesion and friction as discussed in Chapter 5.

This process was also used to achieve superhydrophobic surfaces for objective (c) as described in Chapter 6. Based on geometrical requirement for air-trapping formation, relations between roughness parameters and superhydrophobicity were also developed as discussed in Chapter 7. Finally Chapter 8 will cover the conclusions and future work.

Experimental details of the developed process are given in Appendix A. Appendix B is the matlab codes used in Chapter 3.

References

[1]   B. Bhushan, *Principles and applications of tribology* (John Wiley & Sons, 1999).

[2]   T. R. Thomas, *Rough surfaces* (Longman Group Limited, New York, 1982).

[3]   J. A. Greenwood and J. J. Wu, Meccanica 36, 617-630 (2001).

[4]   D. J. Whitehouse, Wear 249, 345-353 (2001).

[5]   M. S. Longuet-Higgins, Proceedings of the Royal Society of London, Series A, Mathematical and Physical Sciences 250, 157-174 (1957).

[6]   D. J. Whitehouse and J. F. Archard, Proceedings of the Royal Society of London, Series A, Mathematical and Physical Sciences 316, 97-121 (1970).

[7]   D. J. Whitehouse and M. J. Phillips, Philosophical Transactions of the Royal Society of London, Series A, Mathematical and Physical Sciences 290, 267-298 (1978).

[8]   D. J. Whitehouse and M. J. Phillips, Philosophical Transactions of the Royal Society of London, Series A, Mathematical and Physical Sciences 305, 441-468 (1982).

[9]   J. A. Greenwood, Proceedings of the Royal Society of London, Series A, Mathematical and Physical Sciences 393, 133-157 (1984).

[10]   D. Maugis, *Contact, adhesion, and rupture of elastic solids* (springer, Berlin, 2000).

[11]   J. A. Greenwood and J. B. P. Williamson, Proceedings of the Royal Society of London, Series A, Mathematical and Physical Sciences 295, 300-319 (1966).

[12]   P. R. Nayak, wear 26, 305-333 (1973).

[13]   A. W. Bush, R. D. Gibson, and G. P. Keogh, Journal of Lubrication Technology-Transactions of the ASME 101, 15-20 (1979).

[14]   T. Ozel and Y. Karpat, International Journal of Machine Tools & Manufacture 45, 467-479 (2005).

[15]   R. L. Hecker and S. Y. Liang, International Journal of Machine Tools & Manufacture 43, 755-761 (2003).

[16]   S. A. Campbell, K. Cooper, L. Dixon, R. Earwaker, S. N. Port, and D. J. Schiffrin, Journal of Micromechanics and Microengineering 5, 209-218 (1995).

[17]   J. Y. Kim, J. Yu, J. H. Lee, and T. Y. Lee, Journal of Electronic Materials 33, 1459-1464 (2004).

[18]   J. Seo, J. L. Lutkenhaus, J. Kim, P. T. Hammond, and K. Char, Macromolecules 40, 4028-4036 (2007).

[19]   R. Pantani, I. Coccorullo, V. Speranza, and G. Titomanlio, Progress in Polymer Science 30, 1185-1222 (2005).

[20]   W. Barthlott and C. Neinhuis, Planta 202, 1-8 (1997).

[21]   T. Young, Philosophical Transactions of the Royal Society of London 95, 65-87 (1805).

[22]   R. N. Wenzel, Industrial and Engineering Chemistry 28, 988 (1936).

[23]   A. B. D. Cassie and S. Baxter, Transactions of the Faraday Society 40, 546 (1944).

[24]   X. J. Feng and L. Jiang, Advanced Materials 18, 3063-3078 (2006).

[25]   J. Ji, J. Fu, and J. Shen, Advanced Materials 18, 1441-1444 (2006).

[26]   S. Wang, L. Feng, and L. Jiang, Advanced Materials 18, 767-770 (2006).

[27]   N. Zhao, J. Xu, Q. D. Xie, L. H. Weng, X. L. Guo, X. L. Zhang, and L. H. Shi, Macromolecular Rapid Communications 26, 1075-1080 (2005).

[28]   G. Zhang, D. Y. Wang, Z. Z. Gu, and H. Mohwald, Langmuir 21, 9143-9148 (2005).

[29]   Q. D. Xie, G. Q. Fan, N. Zhao, X. L. Guo, J. Xu, J. Y. Dong, L. Y. Zhang, Y. J. Zhang, and C. C. Han, Advanced Materials 16, 1830-+ (2004).

[30]   A. Nakajima, A. Fujishima, K. Hashimoto, and T. Watanabe, Advanced Materials 11, 1365 (1999).

[31]   L. B. Zhu, Y. H. Xiu, J. W. Xu, P. A. Tamirisa, D. W. Hess, and C. P. Wong, Langmuir 21, 11208-11212 (2005).

[32]   K. K. S. Lau, J. Bico, K. B. K. Teo, M. Chhowalla, G. A. J. Amaratunga, W. I. Milne, G. H. McKinley, and K. K. Gleason, Nano Letters 3, 1701-1705 (2003).

[33]   J. Genzer and K. Efimenko, Science 290, 2130-2133 (2000).

[34]   A. Hozumi and O. Takai, Thin Solid Films 303, 222-225 (1997).

[35]   R. Hatada and K. Baba, Nuclear Instruments & Methods in Physics Research Section B-Beam Interactions with Materials and Atoms 148, 655-658 (1999).

CHAPTER 2. THE EFFECT OF AUTOCORRELATION LENGTH ON THE REAL AREA OF CONTACT AND FRICTION BEHAVIOR OF ROUGH SURFACES

A paper published in *Journal of Applied Physics*

Yilei Zhang and Sriram Sundararajan

Mechanical Engineering Department, Iowa State University, Ames, Iowa 50011, USA

Abstract

Autocorrelation length (ACL) is a surface roughness parameter that provides spatial information of surface topography that is not included in amplitude parameters such as Root Mean Square roughness. This paper presents a relationship between ACL and the friction behavior of a rough surface. The influence of ACL on profile peak distribution is studied based on Whitehouse and Archard's classical analysis (Proceedings of the Royal Society of London, Series A, Mathematical and Physical Sciences 316, 97-121, 1970) and their results are extended to compare profiles from different surfaces. The probability density function of peaks and the mean peak height of a profile are given as functions of its ACL. These results are used to estimate number of contact points when a rough surface comes into contact with a flat surface and it is shown that the larger the ACL of the rough surface, the less the number of contact points. Based on Hertzian contact mechanics, it is shown that real area of contact increases with increasing of number of contact points. Since adhesive friction force is proportional to real area of contact, this suggests that the adhesive friction behavior of a surface will be inversely proportional to its ACL. Results from microscale friction experiments on polished and etched silicon surfaces are presented to verify the analysis.

Keywords: surface roughness, friction, autocorrelation length, silicon

Introduction

It is well known that surface roughness plays an important role in the friction behavior of an interface[1-3]. If a surface can be described by a Gaussian random process, statistical parameters describing the surface height variation can be completely defined based on its height distribution and autocorrelation function, that is, the surface is totally determined in a statistical sense. A lot of work has been done to derive surface roughness descriptors that can be practically used for both 1-D (profile) and 2-D (surface) situations[4-10]. A Gaussian distribution of ordinates has been experimentally shown to be valid for many engineering surfaces[4]. Another common assumption is that the autocorrelation function has an exponential form, which has also been verified experimentally[5-7]. In order to simplify calculation, surfaces are assumed to be isotropic, even though it is believed that at least in principle the same analysis can be extended to anisotropic surfaces[5]. Special emphasis has been placed on the distribution of peaks[4-11] because when two surfaces approach each other, the peaks will undergo contact first, and the distribution of peaks will decide the real area of contact. This reasoning is true especially in predominantly elastic contacts and is utilized in many friction models[4,12,13].

It is well known that both height parameters and spatial functions are needed to describe the height distribution and texture of a rough surface[14]. Autocorrelation function and autocorrelation length (ACL) have been widely used in surface related studies[15-19] to provide spatial information in addition to amplitude parameters, such as Root-Mean-Square roughness. Generally, ACL is used to measure how quickly a random event decays or the distance over which two points can be treated as independent in a random process.

In early friction studies, Rabinowicz had deduced the size of contact junctions based on a simple model of the sliding process using autocorrelation analysis, where the junctions were assumed to have the same size, but different shear strengths[20]. However, a detailed analysis of ACL and its relation, if any, to friction behavior is lacking. Other recent works

suggest that the correlation length affects sub-surface stresses in coatings[21] as well as adhesion of thin elastic films[22]. The main objective of this paper is to analyze the effects of ACL on real area of contact and adhesive friction force based on peak analysis. A physical understanding of ACL that is suitable for tribological applications is proposed based on statistical description of rough surfaces and Hertzian contact mechanics. Results from microscale friction experiments of silicon samples with different ACL are provided to verify the analysis.

Theory

ACL and Number of Contact Points

The mathematical definition of the autocorrelation function of a profile $h(x)$ of length L is given as:

$$C(\tau) = \lim_{L \to \infty} \frac{1}{L\sigma^2} \int_0^L [h(x) - m][h(x + \tau) - m]dx \qquad \textbf{1}$$

where τ is a spatial separation, m and σ^2 is the mean value and variance of the profile respectively. An exponential form of autocorrelation function is used to approximate the autocorrelation function, and for most engineering surface this can be written as:

$$C(\tau) = \exp(-\tau / \beta^*) \qquad \textbf{2}$$

where β^* is equal to the ACL. ACL is typically defined as the distance at which the value of the autocorrelation function is $1/e$ of its original value.

The Gaussian distribution of ordinates on a profile is given by:

$$f(y) = \frac{1}{\sqrt{2\pi}} \exp(-\frac{y^2}{2}), \qquad \textbf{3}$$

where y is the normalized ordinate, i.e., h/σ, and σ is the standard deviation of the ordinate distribution.

Peaks on a profile can be defined as points that are higher than both of its left and right neighbors. So the probability of an ordinate y_0 being a peak at a height between y and $y + dy$ is in the following form:

$$\text{Prob}[y_{left} < y, y < y_0 < y + dy, y_{right} < y],$$

Whitehouse and Archard[5] derived the probability density function of an ordinate being a peak at height y using the jointed probability density of the three ordinates. They gave the following simplified result for this function based on the assumption that the correlation function is exponential:

$$f^*(y, \rho) = \frac{1}{4\sqrt{2\pi}} \left[1 + erf\left(\frac{y}{\sqrt{2}} \sqrt{\frac{1-\rho}{1+\rho}} \right) \right]^2 \exp\left(-\frac{1}{2} y^2 \right) \qquad \textbf{4}$$

where $\rho = \exp(-\frac{\lambda}{\beta^*})$, λ is the interval between two sampling points and β^* is the ACL as defined in Eq. 2. The mean value of the peak heights density curve[5] is given as:

$$\bar{y}^*(\rho) = \frac{1}{2N} \left(\frac{1-\rho}{\pi} \right)^{\frac{1}{2}} \qquad \textbf{5}$$

where N, the normalizing factor, is the ratio of number of peaks to number of ordinates, given by

$$N = \frac{1}{\pi} atan\left(\sqrt{\frac{3-\rho}{1+\rho}} \right) \qquad \textbf{6}$$

From Eq. 5 it is clear that both the peak height density function and the mean peak height are functions of ACL and sampling interval.

Whitehouse and Archard's analysis was for one profile from a surface measured with different sampling intervals. Now we consider profiles from different surfaces that obey a normal distribution and that are sampled at the same interval. We also assume every profile has an exponential autocorrelation function with different ACL values. Since Whitehouse and Archard's conclusions are given in a statistical sense, it does not matter whether the profiles are from one surface with different sampling intervals or from different surfaces with
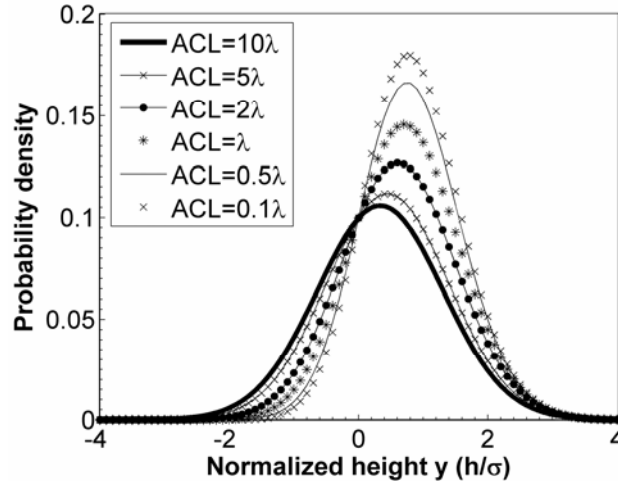
Figure 1. **Probability of an ordinate being a peak at height *y*. σ is the standard deviation of ordinates.**

the same sampling interval as long as all surfaces satisfy the three assumptions made by them: 1) normal distribution of ordinates; 2) exponential autocorrelation function and 3) isotropic topography. This makes it possible to compare peak distribution of profiles from different surfaces using only ACL if sampling intervals are kept constant for the comparison. Figure 1 plots the peak density function for profiles with different ACL in terms of a constant sampling interval λ. From the figure it is clear that a profile with a larger ACL has a broader peak distribution and the mean peak height is closer to the mean line than a profile with a smaller ACL. Figure 2 plots the normalized mean height of peaks ($\bar{h}/\sigma$) as a function of ACL at a constant sampling distance λ. It can be seen that as the ACL decreases, the mean peak height moves away from the mean line up to around 0.85σ, where σ is the standard deviation of the normal distribution of ordinates.

From Fig. 1 it can be found that at a given height above the mean line, an ordinate on a profile with smaller ACL always has a higher probability of being a peak than an ordinate on a profile with larger ACL. For profiles with a given length *L* and sampling interval λ, the total number of ordinates should also be the same. Thus the total number of peaks n_δ above a
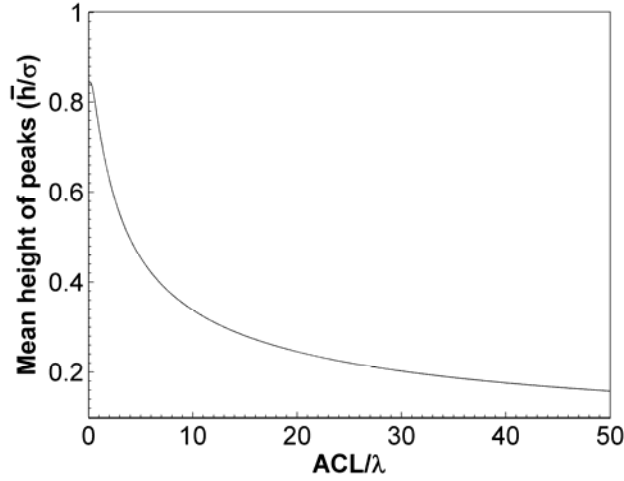
Figure 2. **The variation of mean height of peaks with ACL for constant sampling distance** λ.

given normalized height δ is proportional to the area under the peak density plot measured from δ to infinity as follows,

$$n_\delta = \frac{L}{\lambda}\int_\delta^\infty f^*(y,\rho)dy,$$ **7**

This means the total number of peaks above a given height for any profile is only a function of ACL. For example, considering two profiles with different ACL, say, $\beta_1^* > \beta_2^*$, we will have $n_{\delta 1} < n_{\delta 2}$. Thus profile 2 will have more peaks at any given height δ above the mean line than profile 1.

Since peaks will come into contact first when two surfaces approach each other, the total number of contact points under a given load will be equal to the number of peaks above a determined height if no peaks merge together under the load. Based on the above peak analysis, the relation between number of contact points and ACL is shown in Fig. 3, where peaks higher than 2σ are set to be in contact. It is clear that a larger ACL leads to a smaller number of contact points while a smaller ACL leads to a larger number of contact points. Since all surfaces are isotropic, the above conclusion for 1D profile should still be true for 2D surface in a qualitative sense.
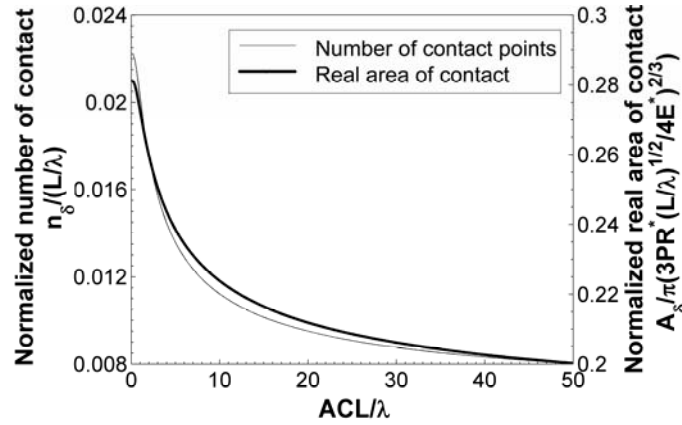
Figure 3.　　　**Variation in number of contact points and real area of contact with ACL for a rough surface in contact with a flat surface at a given load. Peaks higher than 2σ are assumed to come into contact.**

ACL and Real Area of Contact at low loads

When two solid surfaces come into contact, surface roughness causes contact to occur at discrete contact spots, and the total area of which is a small fraction of the nominal area of contact. This real area of contact dictates tribological behavior of the interface and is used in many friction and wear models[12-14]. Various studies have been conducted to evaluate real area of contact via analytical and numerical methods[4,12,23-28], the earliest being the Greenwood and Williamson's analysis[4]. Researchers have also developed methods to experimentally evaluate real area of contact using for example, contact resistance[29], ultrasonic[30,31] or optical methods[32]. However, experimental determination of real area of contact in various systems still remains non-trivial. Real area of contact can also be estimated using contact mechanics models that build upon Hertz[4], Johnson-Kendall-Roberts (JKR)[33], Derjaguin-Muller-Toporov (DMT)[34] or Maugis[35] mechanics. Here we employ a Hertzian-mechanics-based model to estimate real area of contact. For simplification, we assume one of the two contacting surfaces is perfectly flat while the other one is rough and its peaks can be treated as spheres with the same radius.

First, in the case of a simple sphere with radius R, elastic modulus E_1 in contact with a flat surface with elastic modulus E_2, Hertzian contact theory gives the real area of contact as,

$$A_i = \pi \left(\frac{3PR^*}{4E^*} \right)^{2/3} \qquad\qquad 8$$

where P is the normal load, R^* is the equivalent radius given by R in this case, E^* is the equivalent Young's modulus $\frac{1}{E^*} = \frac{1-v_1^2}{E_1} + \frac{1-v_2^2}{E_2}$ and v_1, v_1 are Poisson's ratio for both surfaces respectively. The real area of contact is thus proportional to $P^{2/3}$.

Second, we assume the number of contact points at a total load P to be n. Considering the load to be low and thus, deformation to be small, we assume that the load is supported equally by all contact points with each contact point carrying a small load given by P/n. So the total real area of contact in this case can be obtained as

$$A = nA_i = n\pi \left(\frac{3PR^*/n}{4E^*} \right)^{2/3} = n^{1/3} \pi \left(\frac{3PR^*}{4E^*} \right)^{2/3} \qquad\qquad 9$$

Finally, let's compare the real area of contact of two rough surfaces with different ACL coming into contact with a flat surface. Assuming the number of contact points is n_δ, where δ is the normalized height above which peaks on the rough surface come into contact with the flat surface, we have

$$A_\delta = n_\delta^{1/3} \pi \left(\frac{3PR^*}{4E^*} \right)^{2/3} \qquad\qquad 10$$

Substituting our expression for number of peaks (n_δ) from Eq. 7, we obtain

$$A_\delta = \left(\frac{L}{\lambda} \int_\delta^\infty f^*(y,\rho)dy \right)^{1/3} \pi \left(\frac{3PR^*}{4E^*} \right)^{2/3}$$

$$= \pi \left(\frac{3PR^*}{4E^*} \sqrt{\frac{L}{\lambda}} \right)^{2/3} \left(\int_\delta^\infty f^*(y,\rho)dy \right)^{1/3} \qquad\qquad 11$$

Equation 11 suggests that the real area of contact at a given load is a function of δ and ρ, which in term is a function of ACL.

Since the load and deformation are small, we can assume that the height δ above which peaks come into contact with the flat surface under a given load are the same for both rough surfaces. It should be noted that height δ is normalized by the standard deviation of ordinate distribution σ, thus the same normalized height on both surfaces does not require the same value of interference. Figure 3 also plots the normalized real area of contact (Eq. 11) as a function of ACL for peaks higher than 2σ ($\delta = 2$). It can be seen that a surface with a smaller ACL will have a larger real area of contact than a surface with a larger value of ACL.

ACL and Adhesive Friction Force

The friction force between two solid surfaces in relative motion against each other is composed of an adhesive component and a deformation component. At low loads and elastic conditions, the adhesive component dominates and is given by:

$$F_f = A_r \tau_a \qquad\qquad \textbf{12}$$

where τ_a is the average shear strength of the contact and A_r is the real area of contact. This means that for a given material pair (constant τ_a), a larger real area of contact will lead to a larger adhesive friction force. It has been shown previously in section B that under low loads, a surface with larger ACL would exhibit a smaller real area of contact as compared to a surface with smaller ACL. Hence, for a given material and relatively low loads, a surface with larger ACL will exhibit a lower adhesive friction response than a surface with a smaller value of ACL.
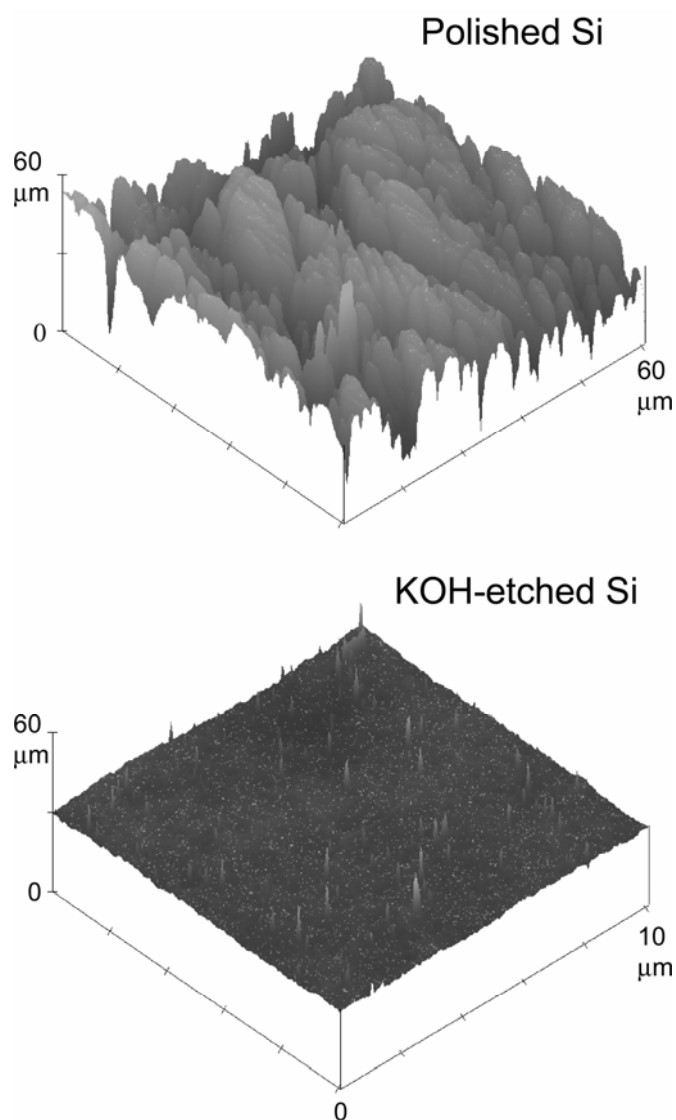
Polished Si

KOH-etched Si

Figure 4.   AFM surface height images of polished and KOH-etched silicon samples.

Experiment

We performed friction experiments on silicon samples with different surface roughness characteristics to verify our analysis. All silicon samples were made from n-type (100) silicon wafer from Virginia Semiconductor, Inc. (Fredericksburg, Virginia). Wafers were cut to 1.5×5 *cm*^{2} coupons. We prepared Si samples to exhibit different levels of roughness via polishing and etching techniques. Polished Si samples were obtained by

manually polishing the coupons with a 6 inch grinding machine (Adolph & Buehler, Chicago) in the following sequence: first, by using Grit. 1200 sandpapers at 250 rpm for 2 minutes followed by diamond suspension (grain size around 3 μm) for 5 minutes, and finally using silica colloidal (grain size around 0.05 μm) for another 4 minutes. After the polishing sequence, the samples were ultrasonically rinsed in de-ionized (DI) water for 10 minutes.

For chemically etched samples, the coupons were first dipped into BOE at room temperature for 1 minute to remove the native oxidized layer. This was followed by a rinse in DI water for 3 minutes. The coupons were then immersed in 25 $wt\%$ KOH solution for 10 minutes at temperature around 80 $\degree C$. The samples were subsequently ultrasonically rinsed in DI water for 5 minutes, following which they were immersed in 49% hydrofluoric acid for 15 seconds to remove possible alkalescence leftovers. Finally the samples were rinsed in DI water for 5 minutes. During the etching procedure, samples were kept wet to minimize attachment of particles to sample surfaces.
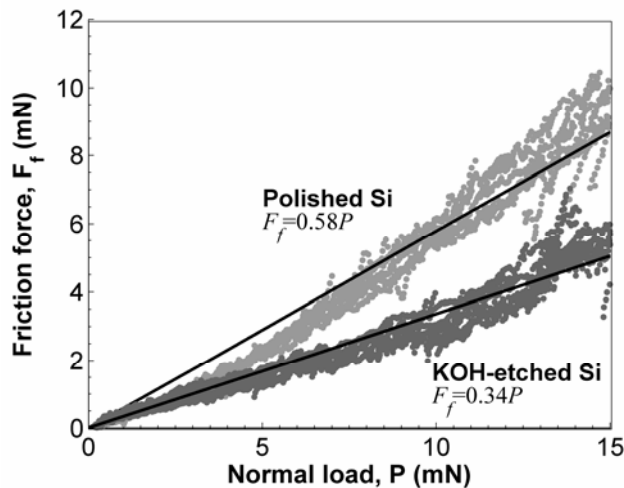

Figure 5.   **Microtribometer friction force data as a function of normal load for prepared Si samples. Data from seven runs are shown. Coefficient of friction values (slope) from linear fits of the data are shown. The R^2 values of the linear fits are 0.958 for polished Si and 0.933 for KOH-etched Si.**

Both samples were then scanned with an atomic force microscope (AFM, Dimension™ 3100, Nanoscope IV, Digital Instruments/Veeco Metrology, Santa Barbara) in contact mode using a silicon nitride tip (radius of 40 *nm* determined using a tip evaluation sample) to obtain surface topography. Figure 4 shows AFM topography maps of the prepared samples at a scan size of 10×10 *μm²*. On the AFM image of KOH etched sample, it can be seen that there are some small particles left on the sample surface. Since the particles are very small, their effect on the microscale friction measurement (described next) can be neglected. These particles were not included in the calculation of surface roughness parameters.

Friction forces were measured using a home-built microtribometer with a normal resolution of 15 *μN* and lateral resolution of 5 *μN* at 20 *°C* and relative humidity (RH) of 20*%* to minimize contribution due to a water layer. The probe was a silicon nitride ball with radius of 1.2 *mm*; a stroke length of 10 *mm* was used at a speed of 0.6 *mm/s*. The normal load was linearly increased from 0 to 15 *mN* during each stroke. Seven runs for every sample were performed. Figure 5 shows all the friction data for both samples. Both samples exhibited some stick-slip like variation at higher loads. It can be seen that the polished Si sample exhibits higher friction forces than the KOH-etched sample.

Table I: Average roughness parameters for polished and etched samples at 10um scan size obtained from AFM scans. Variations in values were typically ±10%.

	RMS (nm)	Mean peak-to valley height S_z (nm)	Skewness S_k	Kurtosis K	ACL (μm)
Polished Si	23.70	290	2.28	14	0.30
Etched Si	3.47	19	-0.05	2.67	1.07

The maximum nominal contact area between Si_3N_4 ball and silicon sample was calculated as $73 \ \mu m^2$ at $P = 15 \ mN$ using Eq. 8. We used $v_{Si_3N_4} = 0.25$ [36], $E_{Si_3N_4} = 307 \ GPa$ (from manufacturer: Hoover Precision Products, Cumming, GA), $v_{Si} = 0.234$ [37] and $E_{Si} = 178.6 \ GPa$ [37] for the calculation. We performed the AFM topography scans at $10 \times 10 \ \mu m^2$ in order to scan roughly the same area as the nominal contact area from which we could obtain surface roughness parameters. Table 1 lists the measured roughness parameters of the prepared surfaces. The parameters shown are Root-Mean-Square (RMS) roughness, average peak-to-valley height (S_z), skewness (S_k), kurtosis (K) and ACL. Note that the polished surface is distinctly rougher than the etched sample. For the polished sample, the large deviation of skewness and kurtosis from Gaussian distribution may be caused by the inherent inefficiency of these parameters[38]. Note that the polished Si sample exhibits much lower value of ACL ($0.30 \ \mu m$) than that of the etched sample ($1.07 \ \mu m$).

Discussion

In order to apply our ACL-based contact analysis to our experimental data, we verified that the surfaces satisfied three assumptions discussed in section A. The first assumption that ordinates obey a normal distribution was verified by observing the cumulative distribution of the surfaces as shown in Fig. 6. The plots show a large linear range, indicating that a large range of ordinates follow a normal distribution. For the polished sample, this is physically reasonable because polishing is accomplished by a large number of small particles with random shape. So the final height distribution of sample surface is a combination of random scratching and would follow normal distribution according to central limit theorem. For the etched sample, the chemical etching process is influenced greatly by bubbles generated on the sample surface, which are randomly distributed, thus resulting a normal distribution of surface heights[39,40]. The autocorrelation functions for both samples are plotted in Fig. 6, which can be approximated well with exponential functions, thus satisfying

the second assumption. Finally, it is clear that the assumption of an isotropic surface is valid for both surfaces since no directional patterns can be observed from the AFM images.

AFM pull-off forces were measured at low humidity (RH = 20%) to verify the adhesive properties of both samples were not modified during preparation. We ensured no
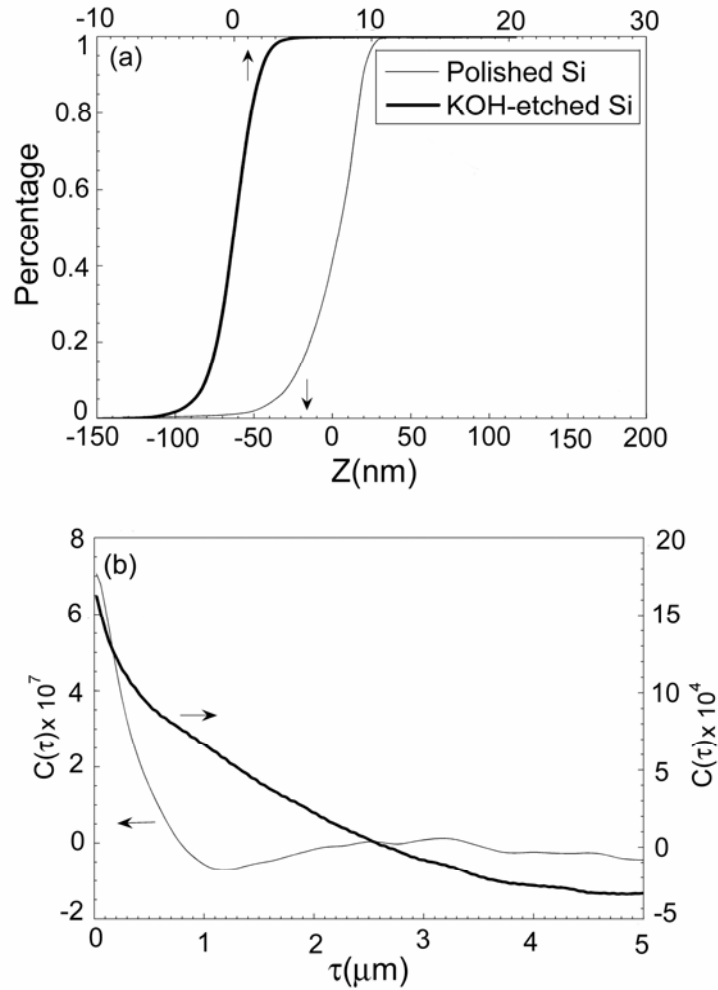

Figure 6.   (a) Cumulative distribution plots for prepared Si samples. Both plots exhibit large linear range, verifying that the surfaces follow a normal distribution. (b) Plots of autocorrelation function for the prepared silicon sample. Both functions can be considered to be exponential in form.

change in tip shape/radius for our probe during measurements using a tip characterizer sample. Hence variation in observed pull-off forces should only be caused by the adhesive properties of samples in the single-asperity contact. Figure 7 shows the adhesive force for both samples to be comparable.

Next, plasticity index was calculated for each surface pair to check whether the contact between Si_3N_4 and the silicon samples were in the elastic region. The plasticity index can be defined as follows [11]:

$$\psi = \frac{E^* \sigma^*}{H \beta^*},$$

13

where H is the hardness of softer material and in this case $H_{Si} = 11 \ GPa$ [41], E^* is the reduced elastic modulus, σ^* and β^* are the standard deviation of surface heights and ACL of the composite rough surface respectively. For surfaces with $\psi < 0.6$, deformations are predominantly elastic while for $\psi > 1$, plastic deformation would occur even at trivial loads. The average plasticity indexes obtained were $\psi = 0.91$ for the polished sample, in the indeterminate range, and $\psi = 0.037$ for the KOH-etched sample, which is clearly in the elastic region. These numbers coupled with the fact that no tracks were found after sliding in
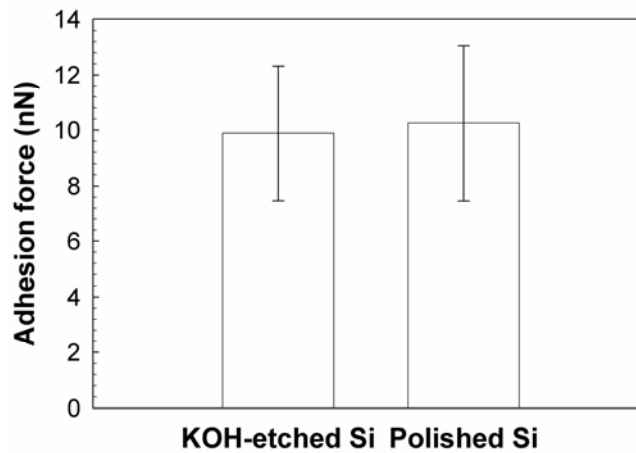

Figure 7. Adhesive force for etched and polished samples measured using AFM.

both samples, indicating that both samples undergo predominantly elastic deformation in our experiments.

Since the friction experiments were conducted under relative low external loads under elastic conditions, adhesion can be considered to be the dominant friction component. Hence the friction force is proportional to real area of contact and interfacial shear strength. For a given material interface and interfacial shear strength, it is believed that rougher surface will lead to smaller real area of contact and thus smaller adhesive friction force[14]. Since both samples are silicon and exhibit comparable pull-off force behavior, it is reasonable to expect comparable interfacial shear strengths for both samples. This is verified by single asperity friction experiments performed using the AFM on the samples (Fig. 8). During friction experiments with the AFM, we observed no changes in the radius of the probe. Hence the real area of contact can be assumed to be the same. Variation in friction forces will be caused by variation in the interfacial shear strength. The data show that although the KOH-etched
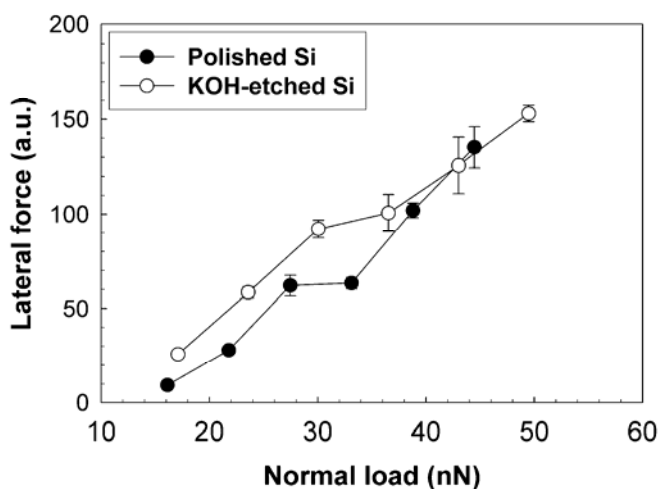

Figure 8. **Single asperity friction data for both samples obtained using AFM. The friction values are comparable at loads above 35 *nN*. This suggests that the interfacial shear strengths are comparable for both samples.**

sample exhibits slightly higher friction forces at low loads, the difference becomes negligible at higher loads. We believe therefore that the interfacial shear strengths of the samples are comparable.

From the AFM data (Table 1), the polished sample is much rougher than the etched one. The microtribometer friction data in Fig. 5 shows that the polished sample exhibits higher friction forces than the etched sample. Linear fits of the friction data for both samples are also plotted in Fig. 5 and the coefficients of friction (COF) are indicated. For the polished silicon sample, COF was found to be 0.5788 with 95% confidence bounds of (0.5760, 0.5817) while for KOH etched sample, COF was 0.3363 with 95% confidence bounds of (0.3344, 0.3383). Thus, COF for the rougher polished sample is higher than that for the smoother etched sample which is contradictory to expectations. The observed behavior can be explained using the ACL analysis presented earlier. From Table 1, the polished sample has a smaller ACL (0.30 μm) than that of the etched sample (1.07 μm). According to our analysis, the polished sample should therefore have more peaks in contact with the Si_3N_4 ball, which will lead to a larger real area of contact and hence larger adhesive friction force than the KOH-etched sample.
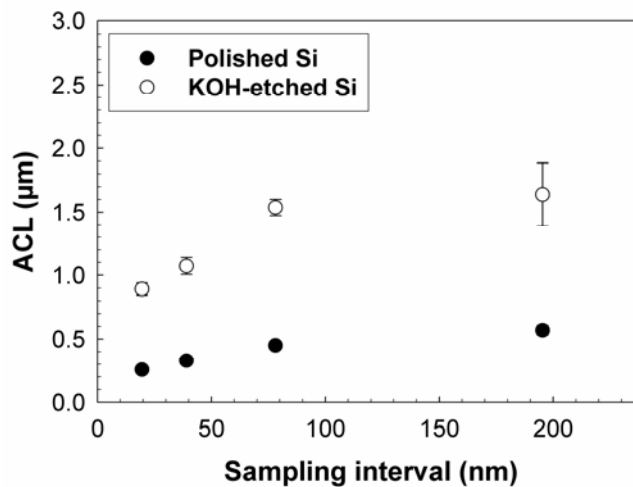

Figure 9. **Effect of sampling interval on ACL of the prepared samples.**

Table II: Roughness parameters and coefficient of friction for TMAH and TMAH+IPA etched samples at 10um scan size reported in Ref. 42.

	RMS (nm)	Mean peak-to-valley height S_z (nm)	Skewness S_k	Kurtosis K	ACL (μm)	Coefficient of Friction
TMAH	2.98	24	-0.27	3.2	1.47	0.27
TMAH+IPA	2.81	19	-0.091	2.6	0.99	0.36

It should be noted that measurements of roughness parameters depend on the sampling interval λ. Figure 9 shows the dependence of ACL on the sampling interval for our polished and KOH-etched samples measured from AFM scans. With an increase of sampling interval, ACL increases for both samples with the KOH-etched sample always exhibiting a larger ACL than the polished sample. However the difference in ACL between the two samples decreases with a decrease in sampling interval, which may be caused by the influence of the AFM tip size. For a small sampling interval that is comparable to, or even smaller than the size of AFM tip, peaks that are included in the statistical model will be lost in the measurement and both samples will appear to have similar structure and have an almost equal ACL. In this study, however, the qualitative results of ACL analysis should be true. This can be shown by the fact that even though ACL changes greatly with sampling length, the polished sample always has a smaller value than that of the etched one at all resolutions.

Data from friction experiments conducted previously[42] on silicon samples etched with different etchants also support our predicted trend between ACL and adhesive friction. In this study, friction tests were conducted using a Si_3N_4 ball-on-flat microtribometer at 0.6 *mm/s* over a 10 *mm* stroke length with a load increasing from 0.2 *mN* to 100 *mN*. Table 2 lists the reported surface roughness parameters and coefficient of friction of silicon samples etched using tetramethyl ammonium hydroxide (TMAH) and TMAH with isopropyl alcohol (IPA)

additive. Note that although both surfaces show comparable RMS roughness, the sample etched with TMAH+IPA shows significantly lower ACL than the sample etched with pure TMAH. The friction behavior is consistent with our analysis — the sample with higher ACL shows lower friction behavior. Our predicted relationship between correlation length, real area of contact and adhesive friction is also supported by other analytical studies of elastic film adhesion based on self-affine roughness models[22,43].

Conclusions

A relation between autocorrelation length (ACL) and real area of contact at low loads was presented based on statistical analysis of surface height data and Hertzian contact mechanics. The analysis showed that a surface with smaller ACL tends to have more peaks at any given height above the mean line than for surfaces with larger ACL, and hence a larger real area of contact. This relation was verified by microscale friction data on silicon surfaces exhibiting different values of ACL. The predominant friction mechanism in the tests was adhesive, resulting in the friction force being directly proportional to real area of contact. The data showed the sample with lower ACL displayed higher friction behavior than surfaces with higher ACL. This study showed that ACL can be an effective surface parameter for peak analysis, real area of contact calculation and adhesive friction force estimation. Further studies to directly measure the real area of contact as a function of ACL are being conducted.

Acknowledgements

References

1 F. P. Bowden and D. Tabor, Philosophical Transactions of the Royal Society of London, Series A, Mathematical and Physical Sciences **169,** 391-413 (1939).

2 J. F. Archard, Proceedings of the Royal Society of London, Series A, Mathematical and Physical Sciences **243,** 190-205 (1957).

3 B. N. J. Persson, *Sliding friction, physical principles and applications*, second ed. (Springer-Verlag Berlin and Heidelberg Gmbh & Co. K, 2000).

4 J. A. Greenwood and J. B. P. Williamson, Proceedings of the Royal Society of London, Series A, Mathematical and Physical Sciences **295,** 300-319 (1966).

5 D. J. Whitehouse and J. F. Archard, Proceedings of the Royal Society of London, Series A, Mathematical and Physical Sciences **316,** 97-121 (1970).

6 D. J. Whitehouse and M. J. Phillips, Philosophical Transactions of the Royal Society of London, Series A, Mathematical and Physical Sciences **290,** 267-298 (1978).

7 D. J. Whitehouse and M. J. Phillips, Philosophical Transactions of the Royal Society of London, Series A, Mathematical and Physical Sciences **305,** 441-468 (1982).

8 J. A. Greenwood, Proceedings of the Royal Society of London, Series A, Mathematical and Physical Sciences **393,** 133-157 (1984).

9 M. S. Longuet-Higgins, Proceedings of the Royal Society of London, Series A, Mathematical and Physical Sciences **250,** 157-174 (1957).

[10] P. R. Nayak, Wear **26,** 305-333 (1973).

[11] R. A. Onions and J. F. Archard, Journal of Physics D: Applied Physics **6** (1973).

[12] W. R. Chang, I. Etsion, and D. B. Bogy, Journal of Tribology **109,** 257263 (1987).

[13] B. N. J. Persson, Physical Review Letters **87** (2001).

[14] B. Bhushan, *Principles and applications of tribology* (John Wiley & Sons, 1999).

[15] R. Schmolke, R. Deters, P. Thieme, R. Pech, H. Schwenk, and G. Diakourakis, Materials Science in Semiconductor Processing **5,** 413-418 (2003).

[16] G. Fishman and D. Calecki, Physical Review Letters **62,** 1302-1305 (1989).

[17] M. Rasigni, G. Rasigni, and J. P. Palmari, Physical Review B **23** (1981).

[18] M. Rasigni and G. Rasigni, Physical Review B **15,** 1915-1919 (1979).

[19] V. N. Koinkar and B. Bhushan, Journal of Applied Physics **81** (1996).

[20] E. Rabinowicz, Journal of Applied Physics **27,** 131-135 (1955).

[21] A. Kadiric, R. Sayles, X. Zhou, and E. Ioannides, Journal of Tribology **125,** 720-730 (2003).

[22] G. Palasantzas and J. T. M. D. Hosson, Physical Review E **67** (2003).

[23] S. Kucharski, T. Klimczak, A. Polijaniuk, and J. Kaczmarek, Wear **177,** 1-13 (1994).

[24] B. N. J. Persson, F. Bucher, and B. Chiaia, Physical Review B **65** (2002).

[25] W. Yan and K. Komvopoulos, Proceedings of the institution of mechanical engineers part J-Journal of Engineering Tribology **212,** 19-32 (1998).

[26] R. Sayles, Tribology International **29,** 639-650 (1996).

[27] S. Lee and N. Ren, Tribology Transactions **39,** 67-74 (1996).

[28] K. Johnson, Wear **190,** 162-170 (1995).

[29] J. A. Greenwood, British Journal of Applied Physics **17,** 1621-1632 (1966).

[30] K. Kendall and D. Tabor, Proceedings of the Royal Society of London, Series A, Mathematical and Physical Sciences **323,** 321-340 (1971).

[31] R. Dwyer-Joyce, B. Drinkwater, and A. Quinn, Journal of Tribology **123,** 8-16 (2001).

[32] B. Bhushan, J. C. Wyant, and C. Koliopoulos, Applied Optics **24,** 1489-1497 (1985).

[33] R. W. Carpick, N. Agrait, D. F. Ogletree, and M. Salmeron, Journal of Vacuum Science and Technology B **14,** 1289-1295 (1995).

[34] M. Enachescu, R. J. A. v. d. Oetelaar, R. W. Carpick, D. F. Ogletree, C. F. J. Flipse, and M. Salmeron, Physical Review Letters **81,** 1877-1880 (1998).

[35] D. Maugis, *Contact, adhesion, and rupture of elastic solids* (springer, Berlin, 2000).

[36] M. Bauccio, *ASM Engineered Materials Reference Book*, second ed. (ASM International, Material Park, OH, 1994).

[37] Y. Matsuoka, Y. Yamamoto, K. Yamada, S. Shimada, M. Tanabe, A. Yasukawa, and H. Matsuzaka, Journal of Micromechanics and Microengineering **5,** 25-31 (1995).

[38] T. R. Thomas, *Rough surfaces* (Longman Group Limited, New York, 1982).

[39] M. Elwenspoek, Journal of the Electrochemical Society **140,** 2075-2080 (1993).

[40] A. S. Louro and J. R. Senna, in *Real-time, In-situ microscopic observation of bubbles and roughening in KOH etching of silicon*, 2001, p. 261-270.

[41] B. Bhushan and X. Li, Journal of Material Research **12,** 54-63 (1996).

[42] S. Chandrasekaran, J. Check, S. Sundararajan, and P. Shrotriya, Sensors and Actuators A, in press (2005).

[43] G. Palasantzas and J. T. M. D. Hosson, Journal of Applied Physics **93,** 893-897 (2003).

CHAPTER 3. GENERATING RANDOM SURFACES WITH DESIRED AUTOCORRELATION LENGTH

Yilei Zhang and Sriram Sundararajan

Department of Mechanical Engineering, Iowa State University, Ames, Iowa, 50011

Abstract

A versatile surface processing method based on electrostatic deposition of particles and subsequent dry etching is shown to be able to tailor the autocorrelation length of a random surface by varying particle size and coverage. An explicit relation between final autocorrelation length, surface coverage of the particles, particle size and etch depth is built. The autocorrelation length of the final surface closely follows a power law decay with particle coverage, the most significant processing parameter. Experimental results on silicon substrates agree reasonably well with model predictions.

81.65.Cf

Introduction

Surface roughness characteristics consist of amplitude and spatial parameters and can often dominate the functional properties of an interface1, making the ability to design surfaces with desired roughness characteristics of great importance. Recent physical models have established that spatial parameters, especially autocorrelation length (ACL), can greatly impact surface functions such as optical properties of a waveguide[2], subsurface stresses in coatings[3], adhesion of thin elastic films[4] as well as contact mechanics and friction behavior[5]. The autocorrelation length is derived from the autocorrelation function (ACF) and is a measure of the degree of randomness of the surface. For surfaces that can be described by self-affine fractal scaling, the ACL is used in conjunction with the Hurst exponent to better

characterize the degree of randomness[4,6]. This letter presents a surface patterning method with the ability to tune the ACL of the final surface. We show that electrostatic deposition[7] of colloidal particles can be used to transfer random patterns onto a surface, which then act as masks during subsequent dry etching. This ensures that the resulting surfaces are random in nature rather than periodic, allowing for the assumption of a Gaussian distribution of the surface heights or peaks and exponential form of ACF, which are conditions obeyed by many engineering surfaces[1,8] and assumed in classical analyses[8,9]. The distribution of particle-dependent features on the surface is modeled as a random telegraph signal (RTS)[10], rather than using popular random sequential adsorption based techniques[11,12]. This approach allows us to build an explicit relation between the autocorrelation length of the final surface and the process parameters: surface coverage and size of the particles and etch depth. Experimental results on silicon surfaces demonstrate the validity of our model and approach.

Methods

The proposed process is shown schematically in Fig. 1. We used a silicon substrate and colloidal silica particles to illustrate the process and verify the dependence of ACL on particle coverage. A clean silicon (100) surface with a negatively charged native oxide layer was achieved using a Piranha etch (3:1 solution of H_2O_2 and H_2SO_4). A poly (diallyldimethyl ammonium) chloride (PDDA) monolayer was deposited via dip-coating to form a uniformly polycationic layer. Silica spheres with an average particle size of 1μm was mixed with MilliQ water and sonicated for 20 minutes to form a colloidal solution into which the silicon substrate is immersed. The negatively charged silica particles are randomly attracted to the positively charged PDDA monolayer on the silicon surface. The coverage of particles on the substrate was varied by controlling the immersion time. After immersion, the samples were rinsed in MilliQ water flow for 5 min to remove loosely held silica particles, and then dried in clean nitrogen flow to ensure that a monolayer of randomly dispersed particles remained
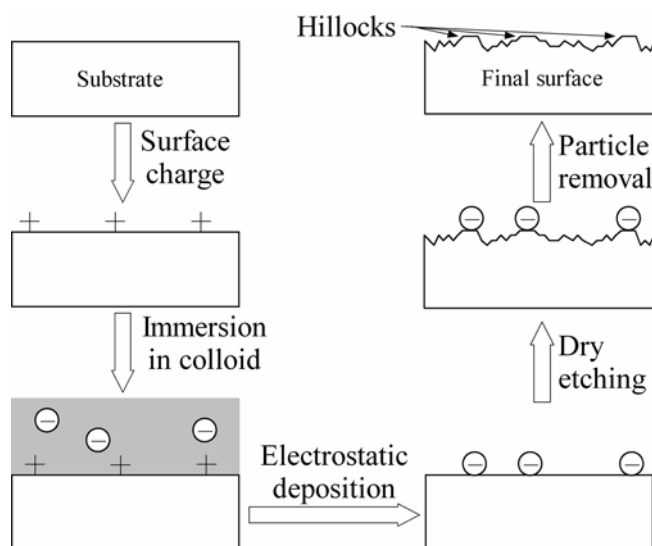
Figure 1. Process sequence to achieve desired autocorrelation length using electrostatic deposition of particles and subsequent dry etching.

on the PDDA coated surface. Next, the samples were dry etched in a reactive ion etch (RIE) chamber (CF_4+O_2) for 25 min. During this line-of-sight etching process, particles act as temporary masks that result in "hillock"-like features on the substrate. The remaining silica particles were then removed using 49% hydrofluoric acid.

Results and discussion

Figure 2 shows the final surface topography of three samples with different coverage (15%, 33% and 53%) obtained using an atomic force microscope (AFM). We note that the hillock-like features reflect clustering of particles that occur during the drying process. Figure 2d shows the details of a hillock, which has a shape and dimensions decided by the diameter of the particles used and the RIE etching time. For a given particle size and etching time, all hillocks had comparable dimensions. We note that the height of hillocks increases with the etching time and reaches a maximum value when silica particles are totally etched away.
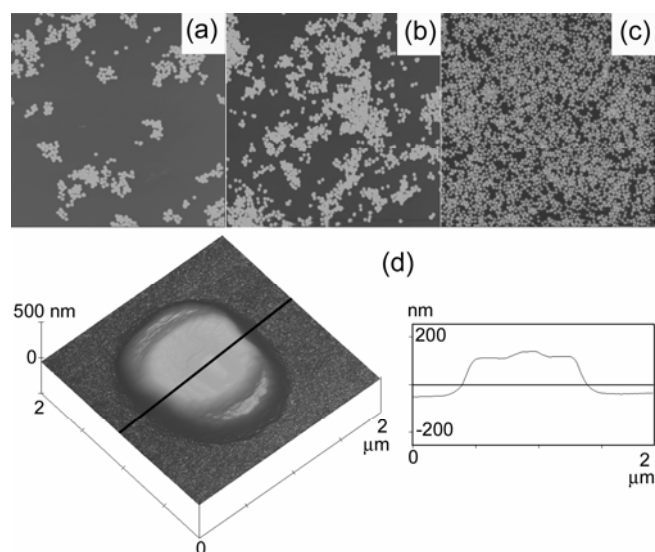
Figure 2. AFM images (60μm × 60μm, vertical scale = 500 nm) of final surfaces with (a) 15%, (b) 53% and (c) 33% coverage of hillocks. (d) Details of a single hillock. Approximate width is 1 μm (particle diameter) and height is about 120 nm.

Figure 3 plots the experimental data of ACL as a function of particle coverage from four samples at different scan sizes (20 μm - 80 μm) obtained from AFM images. Here the ACL is defined, according to traditional use in surface science and engineering, as the distance over which the ACF decays to 1/e of its original value[13]. The values shown are average ACLs of the surfaces[14]. It is clear that for a given particle size and etch depth, ACL decreases with an increase of coverage from 0.2 to 0.6. Below a coverage of 0.2, ACL starts decreasing because at very low coverage, the effect of hillocks becomes negligible and the surface is dominated by RIE etching features. As a result, the practical coverage for this process would be above 0.2. At lower coverages, the clustering effect, which becomes prominent, results in large scatter in the ACL values, as evidenced from Fig. 3. Although the clustering effect could be minimized by using different solvent or drying methods[15], we chose to retain the phenomenon due to its ability to achieve larger values of ACL compared to surfaces without clustering, especially at lower coverage. Thus, clustering allows a larger achievable range of ACL.
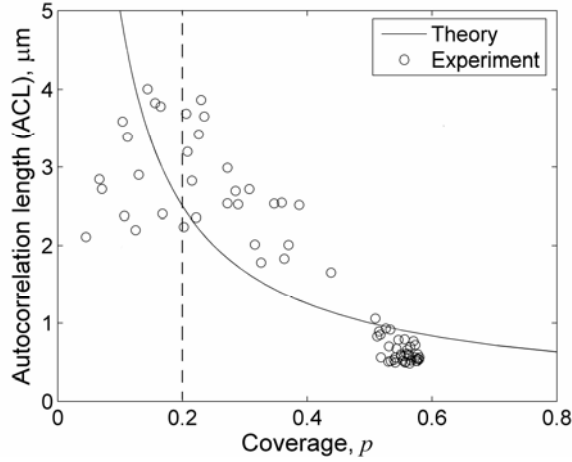
Figure 3. Comparison of theoretical prediction from Eq. 3 (solid line) and experimental data (open circles) on silicon surfaces at a given particle size and etch depth.

We present a statistical model to link the ACL of the final surface to the process variables. We treat the final surface as a superposition of two independent structures: that from the dry etching process (such as RIE) and that from the hillocks caused by particle coverage. For simplification, we model the two structures as two one-dimensional (1D) random processes and the final surface as a superposition of the two random processes. RIE is known to generate sidewall surfaces with exponential ACF[16]. It is therefore reasonable to assume that the ACF of a flat surface processed by dry etching also follows an exponential relation:

$$R_1(\tau) = \sigma^2 e^{-\tau / \beta_1^*} \qquad\qquad \textbf{1}$$

where σ^2 is the variance of the surface profile, β_1^* is its ACL, and τ is the shift in distance.

Since for a given particle size and etch depth, all hillocks would be identical, the entire hillock structure is decided by the dispersion of hillocks. For a 1D situation, a flat substrate is simplified as a straight line and hillocks are simplified as square pulses randomly scattered along the straight line. Designating the height of a hillock as *a* and the vertical zero point to be at the half height, we can denote regions with pulses as having height *a/2* and regions without pulse as having a height of *-a/2*. The observed clustering can be accounted

for by allowing the width of the pulse to be a random variable, i.e., the number of hillocks present inside pulse is a random variable. Since the probability to find the next pulse increases with an increase of distance from an existing pulse and since the intervals between any two pulses are independent, we may assume that the number of pulses in a given profile length follow the Poisson law with an arrival rate λ. A random process that satisfies these features is the random telegraph signal (RTS)[10], which has been widely used in electrical engineering, for example, to model the source/drain channel current with the presence of defects[17]. The ACF for such an RTS is $R_2(\tau) = a^2 e^{-2\lambda\tau}/4$. The arrival rate λ of the Poisson process can be estimated by $\lambda = n/L$, where n is the total number of hillocks (irrespective of whether clustering occurs or not) along a profile with length L. On the other hand, the coverage of pulses along the profile p_1 can be calculated as $p_1 = nd/L = \lambda d$, or $\lambda = p_1/d$, where d is the diameter of a hillock and typically much smaller than the profile length L. Since a profile can be treated as the extreme case of an area with the same length whose width approaches zero, the coverage of pulses p_1 along a profile should be equal to the coverage of hillocks p over the area. Thus, we have $\lambda = p_1/d = p/d$ and can rewrite the ACF of the pulse signal in terms of the area coverage of hillocks as:

$$R_2(\tau) = a^2 e^{-2p\tau/d} / 4 \qquad\qquad \textbf{2}$$

Following our assumption of structure independence, the ACF of the final surface can be written as the superposition of the ACFs of the two random process, that is, $R(\tau) = R_1 + R_2 = \sigma^2 e^{-\tau/\beta_1^*} + a^2 e^{-2p\tau/d} / 4$. The ACL of the final surface β^* satisfies $R(\beta^*) = R(0)/e$, which yields the following equation:

$$p/d = \{\ln(a^2/4) - \ln[(\sigma^2 + a^2/4)/e - \sigma^2 e^{-\beta^*/\beta_1^*}]\}/2\beta^* \qquad\qquad \textbf{3}$$

From Eq. 3, the autocorrelation length thus depends on the coverage of particles p, particle size d and etch depth a as well as the surface characteristics resulting from the dry etch process σ and β_1^*. In the case that $\beta^* \gg \beta_1^*$ and $\sigma \ll a/2$ (which is true for our experiment), Eq. (3) simplifies to a simple power law $\beta^* \approx d/2p$, which means that β^* is

most sensitive to the hillock size, d and distribution, p. This is reasonable because ACL is a spatial parameter and should not be significantly affected by amplitude changes resulting from a and σ. Based on Eq. (3), Fig. 4 plots numerical results of β^* as a function of both particle coverage p and particle size d, and shows behavior close to a power law decay of β^* with particle coverage p, while changing particle size d shifts the curve vertically.

The model's prediction for β^* as a function of particle coverage at a given particle size and etch depth for our experiments is plotted in Fig. 3. We obtained $\sigma = 7.65 \times 10^{-4}$ μm and $\beta_1^* = 0.151$ μm from RIE-etched bare Si(100) while a and d were known to be 0.12 μm and 1 μm respectively (from Fig. 2d). Overall, the model shows the decreasing trend of ACL clearly and provides reasonable estimation of experimental values, especially for coverage higher than 0.2. We note that the RTS model may not completely address the clustering phenomena and is most accurate at coverage close to 0.5^{10}.

Both former work[18] and our experimental results show a linear relation between coverage p and immersion time t in the colloidal solution, i.e., $p(t) \propto t$. Substituting this relation into the expression $\beta^* \approx d/2p$, we obtain $\beta^* \propto 1/t$. This inverse relationship can be used as a guideline to implement the process.
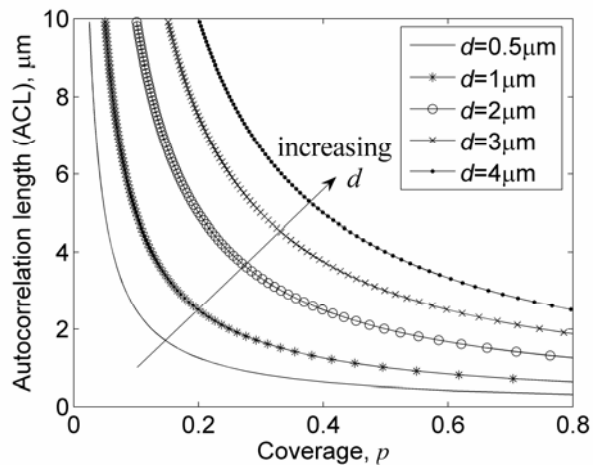

Figure 4. Autocorrelation length as a function of coverage p and particle size d as predicted by the model (Eq. 3).

We finally note that depending on the shape of particles and deposition conditions, there is an upper bound for the coverage. The largest coverage based on 2D random sequential adsorption model for disks is conjectured to be 0.5589, which has been supported by computer simulations[11] and experimental work[15]. But with the existence of clustering, the maximum coverage may be slightly larger. In the case of spherical particles, such as the silica particles used in our experiment, the extreme case is hexagonal closed packed (HCP) or cubic close packed (CCP), which provide the highest p of 0.7405.

Acknowledgements

References

[1]   T.R. Thomas, *Rough surfaces*. (Imperial College Press, London, 1999), p.98.

[2]   F.P. Payne and J.P.R. Lacey, Optical and Quantum Electronics **26**, 977 (1994).

[3]   A Kadiric, RS Sayles, XB Zhou et al., Journal of Tribology **125** (4), 720-730 (2003).

[4]   G. Palasantzas and J.Th.M. De Hosson, Physical Review E **67**, 021604 (2003).

[5]   Yilei Zhang and Sriram Sundararajan, Journal of Applied Physics **97**, 10356 (2005).

[6]   B.B. Mandelbrodt, *The Fractal Geometry of Nature*. (Freeman, New York, 1982).

[7]   R. K. Iler, Journal of Colloid and Interface Science **21**, 569 (1966); H. W. Deckman and J. H. Dunsmuir, Applied Physics Letters **41** (4), 377 (1982).

[8]   J.A. Greenwood and J.B.P. Williamson, Proceedings of the Royal Society of London, Series A, Mathematical and Physical Sciences **295** (1442), 300-319 (1966).

[9]   D.J. Whitehouse and J.F. Archard, Proceedings of the Royal Society of London, Series A, Mathematical and Physical Sciences **316** (1524), 97-121 (1970).

[10]   Henry Stark and John W. Woods, *Probability and Random Processes with Applications to Signal Processing*. (Prentice-Hall, Inc., Upper Saddle River, New Jersey, 2002).

[11]   J. W. Evans, Reviews of Modern Physics **65** (4), 1281 (1993).

[12]   J Talbot, G Tarjus, P.R. Van Tassel et al., Colloids and Surfaces A: Physicochemical and Engineering Aspects **165**, 287-324 (2000).

[13]   Bharat Bhushan, *Principles and applications of tribology*. (John Wiley & Sons, New York, 1999).

[14]   From an AFM scan, a 2-D autocorrelation image can be constructed. The projected area enclosed by a contour at a height equal to 1/e of its maximum value is set to equal a circle. The radius of this circle is defined as the average ACL.

[15]   George Y. Onoda and Eric G. Liniger, Physical Review A **33** (1), 715 (1986).

[16]   Kevin K. Lee, Desmond R. Lim, Hsin-Chiao Luan et al., Applied Physics Letters **77** (11), 1617 (2000); F. Ladouceur, J.D. Love, and T.J. Senden, IEE Proceedings-Optoelectronics **141** (4), 242 (1994).

[17]   M. Xiao, I. Martin, E. Yablonovitch et al., Nature **430**, 435 (2004).

[18]   Zbigniew Adamczyk, Lilianna Szyk-Warszynska, Maria Zembala et al., Colloids and Surfaces A: Physicochem. Eng. Aspects **235**, 65-72 (2004).

CHAPTER 4. METHOD TO GENERATE SURFACES WITH DESIRED ROUGHNESS PARAMETERS

A paper accepted by *Langmuir*

Yilei Zhang and Sriram Sundararajan

Department of Mechanical Engineering, Iowa State University, Ames, Iowa, 50011

Abstract

A surface engineering method based on electrostatic deposition of microparticles and dry etching is described and shown to be able to independently tune both amplitude and spatial roughness parameters of the final surface. Statistical models were developed to connect process variables to the amplitude roughness parameters center line average, root mean square and the spatial parameter, autocorrelation length of the final surfaces. Process variables include particle coverage, which affects both amplitude and spatial roughness parameters, particle size, which affects only spatial parameters and etch depth, which affects only amplitude parameters. Correlations between experimental data and model predictions are discussed.

Introduction

Surface energy and surface forces are often closely related to surface topography. Physically, surface topography is decided by the atomic arrangement at the surface of a material, which in turn may be decided by material properties, processing method as well as environment. Surface topography may be changed by external forces (e.g. during wear), or internal forces (e.g. residual stress). Under stable conditions, surface topography can be described by surface roughness parameters, which include both spatial and amplitude parameters[1]. Amplitude roughness parameters describe height information. For example, central line average (CLA) is an average value measuring points departing from a center line;

and root mean square (RMS) is the standard deviation of profile ordinates. Spatial parameters describe spatial surface information. For example, autocorrelation length (ACL) is the distance over which points on a profile can be treated as independent. In engineering, the ACL is often defined as the distance over which the autocorrelation function decays to $1/e$ of its original value[2]. Besides these commonly used parameters, other parameters are also used to describe surface topography, including statistical parameters for peaks[3] as well as fractal dimension and Hurst exponent for self-affine surfaces[4-6].

Surface roughness parameters are widely used to connect surface topography to a variety of surface phenomena. For example, the amplitude parameters, CLA and RMS have been observed to affect adhesion[7, 8], friction[9, 10], wear[11] as well as optical loss in waveguide[12]. The spatial parameter, autocorrelation length (ACL), has been used to model optical properties of a waveguide[12], substrate stresses in coating[13], adhesion of thin elastic films[6] as well as real area of contact and friction behavior of rough surfaces[14].

In order to systematically study roughness effects and use them for specific applications, it is of interest to develop a processing method that can generate surfaces with desired roughness parameters. Commonly used processing methods, like grinding and polishing, either lead to a large range of roughness variation or lack of the ability to control both amplitude and spatial roughness parameters[15]. Most micro/nano scale fabrication methods, like wet/dry etch, micro-molding or pulsed laser machining, are generally used to realize deterministic structures or may not suitable for processing large areas because of the sequential nature of operation. Recently, we have shown that a micro-particle based surface processing method using electrostatic deposition and dry etching can generate random surfaces with desired ACL[16]. This method is able to generate random surfaces that are not deterministic (i.e. random) and has the advantage of being applicable to large areas, which can potentially translate to high throughput. In this paper, this method is shown to be able to
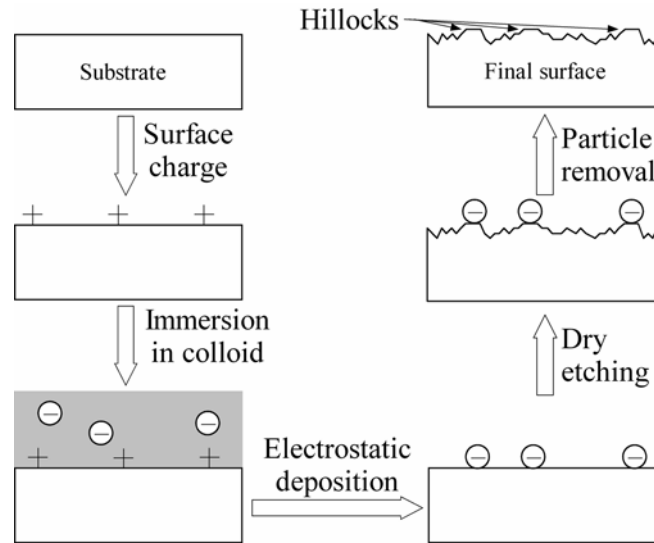
Figure 1. Process sequence involving electrostatic deposition of particles and subsequent dry etching to generate random rough surfaces.

tune *both* amplitude and spatial parameters of the final surface by controlling the process variables of particle size, particle coverage and etch depth.

Experimental Details

Surface processing Technique

The proposed process is shown schematically in Fig. 1. We used a silicon substrate to illustrate the process. First, a clean silicon (100) surface with a negatively charged native oxide layer was achieved using a Piranha etch (3:1 solution of H_2O_2 and H_2SO_4). Next, a uniformly ionic layer is realized. A poly (diallyldimethyl ammonium) chloride (PDDA) monolayer was deposited onto the Si (100) surface via dip-coating to form a polycationic layer in our experiment. Next, the sample is exposed to a colloidal solution of particles which exhibit an inherent charge opposite to that of the ionic layer on the substrate. In our experiment, silica spheres with desired particle size were mixed with MilliQ water and sonicated for 20 minutes to form a colloidal solution into which the silicon substrate is
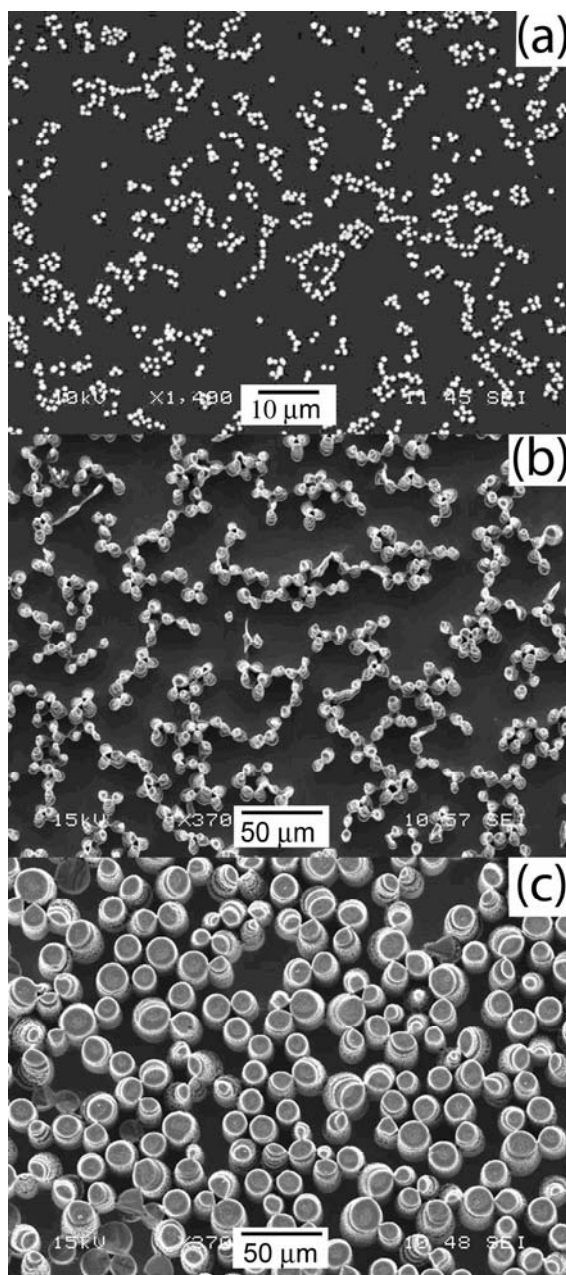
Figure 2. Scanning electron microscopy (SEM) images of final surfaces processed using silica microparticles of various diameters and using different etch depths. (a) microparticle diameter ~ 1 μm, reactive ion etch depth ~ 100 nm; (b) microparticle diameter ~ 10 μm, deep reactive ion etch (DRIE)

immersed. The negatively charged silica particles are randomly attracted to the positively charged PDDA monolayer on the silicon surface. The coverage of particles on the substrate
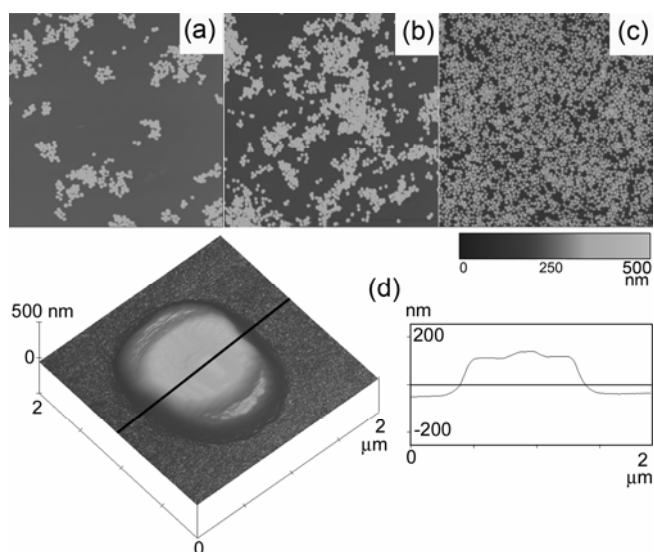
Figure 3. Atomic force microscopy images (60 μm × 60 μm) of final surfaces processed using 1 μm diameter silica microparticles and around 120 nm etch depth for different particle coverages: (a) 15%, (b) 33% and (c) 53% coverage of hillocks. (d) Details of a single hillock.

can be varied by controlling the immersion time[17]. The coverage typically increases linearly with an increase in immersion time. After immersion, the samples were rinsed in MilliQ water flow for 5 min to remove loosely held silica particles, and then dried in clean nitrogen flow to ensure that a monolayer of randomly dispersed particles remained on the PDDA coated surface. Next, the samples were etched in a reactive ion etch (RIE) chamber (CF_4+O_2) for 25 min. For large etch depth, deep reactive ion etch (DRIE) can be used, which is fast and capable of generating high-aspect-ratio structures with C_4F_8 and SF_6 feed gases. During this line-of-sight etching process, particles act as temporary masks that result in "hillock"-like features on the substrate. The remaining silica particles were then removed using 49% hydrofluoric acid. To remove fluorocarbon carry-over generated during dry etch, all samples were cleaned in Piranha etch for half an hour followed by MilliQ water rinsing.

The process variables that affect the final surface topography are particle size, particle coverage and etch depth. Figure 2 shows the final topography as a function of particle size

and etch depth measured using scanning electron microscopy. Figure 3 (a-c) shows the final topography of surfaces as a function of particle coverage measured using atomic force microscopy. Figure 3 (d) shows the topography and cross-section of a single 'hillock'. The hillock has the shape and dimensions decided by the diameter of the particles used and the etch time. These results indicate that the topography of the final surface can be tuned by varying the process variables.

Surface Roughness Measurement

Topography of final surfaces with etch depth below 1 μm were obtained using an atomic force microscope, AFM (Dimension 3100, Veeco Instruments, Santa Barbara, CA) in contact mode with a commercial Si_3N_4 probe (radius ~ 50 nm) at a scan size of 60 μm × 60 μm with 256 × 256 data points. All surface roughness parameters reported were obtained from the AFM images. Topography of surfaces with etch depth in excess of 1 μm were obtained using scanning electron microscopy, SEM (JEOL JSM-606LV) without any conductive coating.

Results and Discussion

Figure 4 shows the effect of particle coverage and etch depth on the amplitude parameters center line average (CLA) and root mean square (RMS) of the final surfaces. Both parameters increase with an increase in etch depth. Also, both parameters increase with increasing coverage upto coverage of 50%, beyond which the parameters appear to decrease with an increase in coverage. We note that the upper limit of coverage for spherical particles on flat substrates is 74%, which corresponds to coverage for hexagonal closed packed (HCP) or cubic close packed (CCP) structure[16]. The amplitude parameters showed no dependence on particle size.
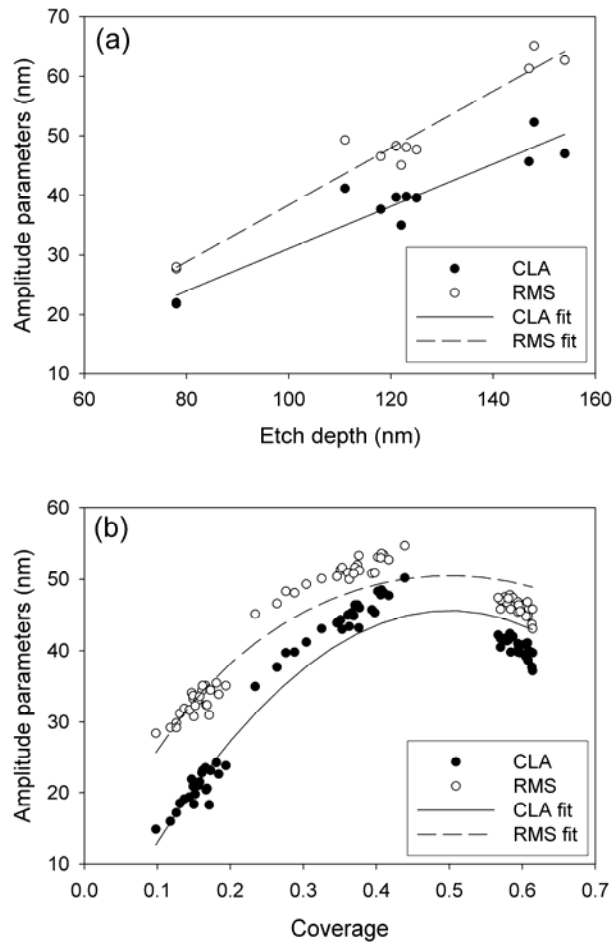
Figure 4. Amplitude parameters, CLA and RMS of processed surfaces as function of (a) etch depth and (b) particle coverage. Model predictions are also shown.

We present a statistical model to relate the amplitude parameters to the process variables. An inspection of the final surfaces shows that their roughness (Fig. 5 (a)) includes two independent components- one caused by the particles, which result in the 'hillock' structures and the other caused by dry etching. For a one-dimensional case, details of a typical profile are shown in Fig. 5 (b) obtained using atomic force microscope, which includes the two components of roughness described above. Figure 5 (c) shows a schematic that simplifies the roughness as a superposition of two random processes. The roughness caused by the particles is approximated as a random pulse signal, where the pulse width is
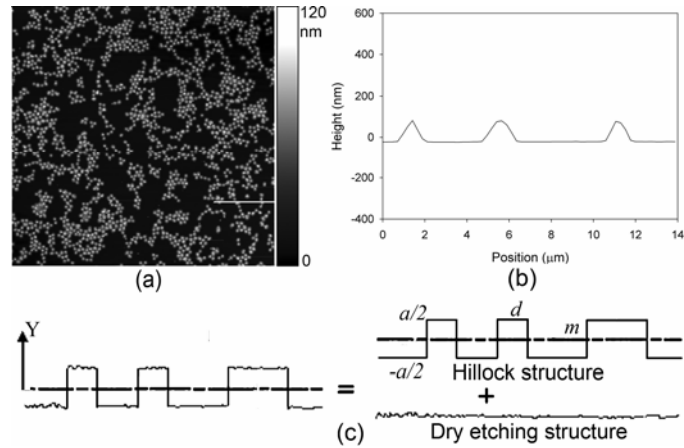
Figure 5. (a) Atomic force microscope image (60 μm × 60 μm) of a final surface processed using 1 μm silica sphere and 100 nm etch depth. (b) Details of a profile from a region of the AFM image showing hillock structure and roughness due to etching. (c) Schematic showing the decomposition of the roughness of generated surfaces into two components: the hillock structure approximated by a pulse and the dry etching structure.

decided by the particle size, d. This representation assumes that the profile goes through the center of all particles. This assumption is reasonable when the particle size is much smaller than the profile length. Generally, dry etched surfaces result in random surfaces that are very smooth with small height variations of several nanometers or less[18]. If this height variation caused by dry etching is much smaller than the dry etching depth, which is generally true for all our experiments, the roughness caused by particles will dominate amplitude roughness parameters of the final surface. We will therefore only consider roughness caused by particles in the following model.

Referring to Fig. 5 (b), if we denote the profile length as L, and the sampling interval as s, the total number of heights measured N can be written as L/s. If we denote the coverage of particles as p, the etch depth as a, and the center of the pulse height as the zero position,

then pN points will have ordinates (heights) of $a/2$ and $(1-p)N$ points will have ordinates of $-a/2$. The ordinate of the center line m can be estimated as follows:

$$
\begin{aligned}
m &= \frac{1}{N}\sum_{1}^{N} y_i \\
&= \frac{1}{L/s}\left(a/2 \times pL/s - a/2 \times (1-p)L/s\right) \qquad \textbf{1} \\
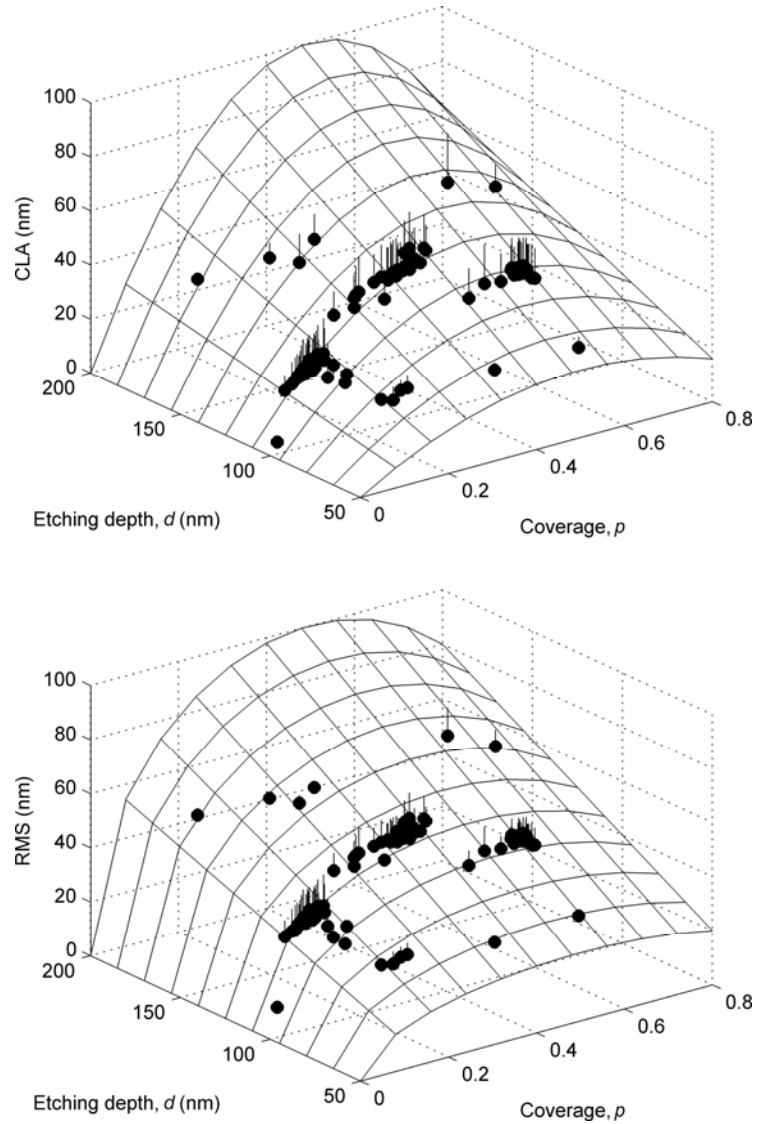&= ap - a/2
\end{aligned}
$$

Figure 6. Model envelopes (grid) and experimental data (solid circles) for amplitude parameters, CLA and RMS as a function of particle coverage and etch depth. Drop-down lines on the data points represent the difference between theory and experiment.

With the center line defined, the amplitude parameters CLA (R_a) and RMS (σ) can be written as follows.

$$
\begin{aligned}
R_a &= \frac{1}{N}\sum_1^N |y_i - m| \\
&= p(a/2 - m) + (1-p)(m + a/2) \\
&= 2ap(1-p)
\end{aligned}
\tag{2}
$$

$$
\begin{aligned}
\sigma &= \sqrt{\frac{1}{N}\sum_1^N (y_i - m)^2} \\
&= \sqrt{p(a/2-m)^2 + (1-p)(m+a/2)^2} \\
&= a\sqrt{p - p^2}
\end{aligned}
\tag{3}
$$

Both CLA and RMS are linearly proportional to etch depth a and are non-linearly dependent on particle coverage p, which match with the trends seen experimentally in Fig. 4. Figure 6 compares the experimental results of CLA and RMS as a function of both particle coverage and etch depth with the model predictions. The model matches the experimental data quite well. We note that coverage p for the experiments are over an area, whereas the model describes a profile. However, the profile is a limiting case of an area and the coverage remains the same. Amplitude parameters generally depend only on the distance of ordinates from the mean line as well as the number of ordinates at a given distance from the mean line. Both these measures are adequately accounted for by the height of the hillocks, a and the coverage, p. Hence particle size does not figure into the relations above. This means that these estimations can be used for different particle size combinations. The expressions derived for this approach can also be applied in cases for which the dry etching may contribute to the roughness in a non-negligible manner (such as materials with inhomogenities and grain boundaries). In these cases, if the background roughness due to etching can be described mathematically using process and material parameters, then our approach can still be used and the final expression for amplitude roughness will include the superposition of two contributing terms – that of the hillock structures and that of the background. Certainly this superposition implies that the hillock structures and the background are independent.

In our previous work, we developed a model relating process variables to the spatial parameter, autocorrelation length (ACL)[16]. We provide a brief description of the model and focus on the results. Briefly the final surface was treated as a superposition of the ACL due to the particle-based structures and that of the dry etching (as shown in Fig. 5 (c)). Dry etching is known to generate random roughness with an exponential autocorrelation function (ACF) on a silicon substrate[19]. For other substrates, in addition to dry etching, grain boundaries or other inhomogeneous features may contribute towards the representation of the ACF form. As long as the ACF for these features can be represented or quantified, the following approach to predict the ACL of the final surface can be applied. The particles were modeled as pulses as described previously in the amplitude parameter model. The occurrence of particles (pulses) along a given profile length is treated as a random process, specifically as a random telegraph signal (RTS), in which pulse width is a variable following Poisson distribution. For conditions in which the particle size is small compared to the profile length, this Poisson approximation is reasonable. The RTS has an exponential autocorrelation function as well[20]. Following our assumption of structure independence, the ACF of the final surface can be written as the superposition of the ACFs of the two random processes. The relation between the ACL of the final surface β^* and process variables is then given as the following equation[16]:

$$p/d = \{\ln(a^2/4) - \ln[(\sigma^2 + a^2/4)/e - \sigma^2 e^{-\beta^*/\beta_1^*}]\}/2\beta^* \qquad \textbf{4}$$

The final autocorrelation length thus depends on the coverage of particles p, particle size d, etch depth a as well as RMS roughness and autocorrelation length of the surface resulting from the dry etching process, σ and β_1^* respectively. In the case that $\beta^* \gg \beta_1^*$ and $\sigma \ll a/2$ (which is true for particle sizes in the micron range), Eq. (4) simplifies to a simple power law $\beta^* \approx d/2p$, which means that β^* is most sensitive to the hillock size, d and particle coverage, p. This is reasonable because ACL is a spatial parameter and should not be significantly affected by amplitude changes resulting from a and σ.
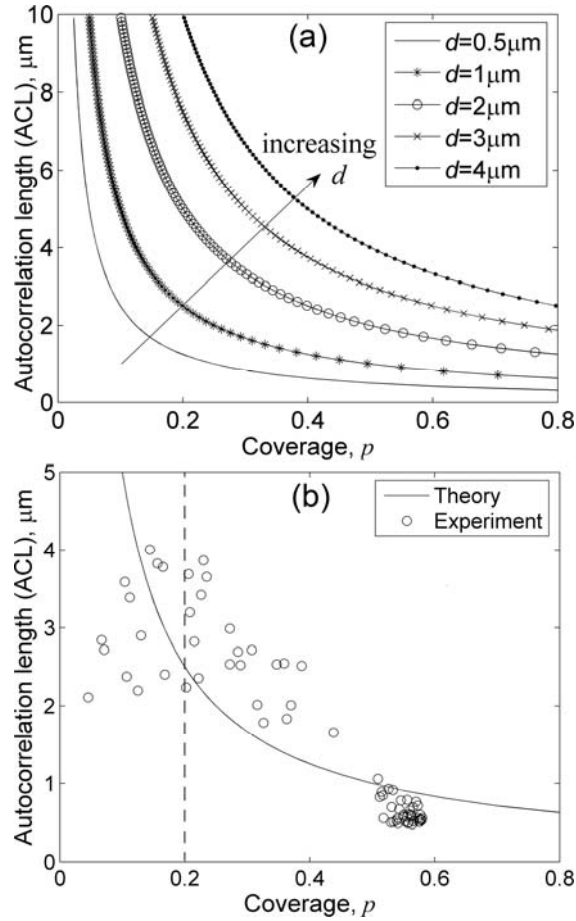
Figure 7. (a) Model prediction (Eq. 4) of the effect of particle size, *d* and coverage, *p* on the spatial roughness parameter, autocorrelation length (ACL). (b) Comparison of model prediction and experimental data for a particle size of 1 μm, etch depth of 80 nm and various coverages.

Figure 7 (a) shows the effect of the process variables on the spatial parameter, autocorrelation length (ACL) based on Eq. 4. Figure 7 (b) shows comparison between the experimental and the model predictions. We did not have enough data points to compare against the prediction for particle size. We note that significant scatter in ACL is seen at lower values of coverage which is attributed to particle clustering and implies that the proposed method may only be applicable for particle coverage larger than 20%. In the RTS model, clustering effect is partly captured by treating pulse length as a Poisson process,

which allows particles to cluster together to form one pulse. This clustering phenomenon is not completely captured by our model and we are currently investigating the use of an explicit structure function into our ACF description (rather than an RTS function) to include the effect of clustering. Furthermore clustering can be minimized by employing techniques such as using functionalized particles [21] or controlling drying conditions[22].We chose to retain clustering phenomenon due to its ability to achieve larger values of ACL compared to surfaces without clustering, i.e., clustering allows a larger achievable range of ACL in our experiments.

From these models it can be seen that particle coverage affects both amplitude and spatial parameters. Etch depth strongly affects the amplitude parameters, whereas particle size affects only spatial parameters. This allows potential independent tailoring of amplitude and spatial parameters if desired. For example, for a given particle size, the particle coverage can be used to tailor the autocorrelation length by varying immersion time in the colloidal solution. Then, the etch depth can be selected to obtain a target value of center line average or root mean square.

Conclusions

A surface engineering process that comprises electrostatic deposition of microparticles and dry etching was shown to be able to tailor the surface structure and roughness parameters of an engineering material. This method has the potential to generate random surfaces with independent control of both amplitude and spatial roughness parameters. Models relating the key process variables- particle size, coverage and etch depth to amplitude and spatial roughness parameters were developed. The experimental results agreed with the model predictions fairly well for amplitude parameters while some discrepancies were observed in the case of autocorrelation length due to the effects of clustering which are not fully captured in our model.

Acknowledgements

References

[1]   T. R. Thomas, *Rough surfaces*, Imperial College Press, London **1999**.

[2]   B. Bhushan, *Principles and applications of tribology*, John Wiley & Sons, **1999**.

[3]   J. A. Greenwood, J. B. P. Williamson, *Proceedings of the Royal Society of London, Series A, Mathematical and Physical Sciences* **1966**, *295*, 300.

[4]   J. Aue, J. T. M. D. Hosson, *Applied Physics Letters* **1997**, *71*, 1347.

[5]   W. Yan, K. Komopoulos, *Journal of Applied Physics* **1998**, *84*, 3617.

[6]   G. Palasantzas, J. T. M. D. Hosson, *Physical Review E* **2003**, *67*, 021604.

[7]   K. N. G. Fuller, D. Tabor, *Proceedings of the Royal Society of London, Series A, Mathematical and Physical Sciences* **1975**, *345*, 327.

[8]   S. C. Lee, A. A. Polycarpou, *J. Tribol.-Trans. ASME* **2004**, *126*, 334.

[9]   G. G. Adams, S. Muftu, N. M. Azhar, *J. Tribol.-Trans. ASME* **2003**, *125*, 700.

[10]   G. Gassin, E. Heinrich, H. A. Spikes, *Tribology Letters* **2001**, *11*, 95.

[11]   K. Miyoshi, R. L. C. Wu, A. Garscadden, P. N. Barnes, H. E. Jackson, *Journal of Applied Physics* **1993**, *74*, 4448.

[12]   F. P. Payne, J. P. R. Lacey, *Optical and Quantum Electronics* **1994**, *26*, 977.

[13]   A. Kadiric, R. Sayles, X. Zhou, E. Ioannides, *Journal of tribology* **2003**, *125*, 720.

[14]   Y. Zhang, S. Sundararajan, *Journal of Applied Physics* **2005**, *97*, 10356.

[15]   P. G. Benardos, G. C. Vosniakos, *Int. J. Mach. Tools Manuf.* **2003**, *43*, 833.

[16]   Y. Zhang, S. Sundararajan, *Applied Physics Letters* **2006**, *88*, 141903.

[17]   Z. Adamczyk, L. Szyk-Warszynska, M. Zembala, M. Lehocky, *Colloids and Surfaces A: Physicochem. Eng. Aspects* **2004**, *235*, 65.

[18]   E. Gogolides, V. Constantoudis, G. P. Patsis, A. Tserepi, *Microelectron. Eng.* **2006**, *83*, 1067.

[19]   K. K. Lee, D. R. Lim, H.-C. Luan, A. Agarwal, J. Foresi, *Applied Physics Letters* **2000**, *77*, 1617.

[20]   H. Stark, J. W. Woods, *Probability and Random Processes with Applications to Signal Processing*, Prentice-Hall, Inc., Upper Saddle River, New Jersey **2002**.

[21]   M. A. B. R. H. P. Howard A. Ketelson, *Polymers for Advanced Technologies* **1995**, *6*, 335.

[22]   G. Y. Onoda, E. G. Liniger, *Physical Review A* **1986**, *33*, 715.

CHAPTER 5. ADHESION AND FRICTION STUDIES OF SILICON SURFACES PROCESSED USING A MICROPARTICLE-BASED METHOD

Yilei Zhang and Sriram Sundararajan

Department of Mechanical Engineering, Iowa State University, Ames, Iowa 50011

Abstract

A surface processing method that combines electrostatic deposition of microparticles and dry etching is utilized to modify the surface topography of silicon surfaces to reduce adhesion and friction force. Microscale adhesion and friction tests were conducted on flat (smooth) and processed silicon surfaces with a low elastic modulus thermoplastic rubber (Santoprene) probe that allowed a large enough contact area to observe the feature size effect. Both adhesion and friction force of the processed surfaces were reduced comparing to that of the flat surfaces.

Keywords: adhesion, friction-Reducing, roughness effects, surface modification

Introduction

As systems are miniaturized, surface forces such as adhesion and friction, become increasingly dominant compared to volume forces, such as gravity and electromotive forces. This is of course due to the fact that the surface area-to-volume ratio is significantly larger at smaller length scales (micro-and nanoscale) than at larger (macroscale) ones. Increased surface forces can hinder relative motion between surfaces and bodies in micro/nanoscale systems such as microparticles on a surface [1]. They can also drastically affect the reliability of microsystem fabrication [2] and operation [3]. A promising method to overcome these

issues is to modify the surface, both chemically and physically, in such a way as to reduce the effect of surface forces. Coatings and films are frequently used to change surface energies. Examples include the use of near frictionless diamond-like carbon coating for tribological applications [4] and self-assembled monolayers as anti-stiction coatings [5]. Physical modification of surface structure can change the real area of contact, and hence reduce contact area dependent phenomena such as adhesion and friction. Theoretical modeling of real area of contact as a function of surface roughness has been conducted based on statistical analyses [6-8] and self-affine models [9]. Various techniques have been used to physically modify surface structure and roughness including reactive ion etching [10], laser micromachining [11], and microparticle deposition [12]. Electrostatic deposition was developed in 1960's [13] and has been used to transfer random or periodic patterns [12]. In this paper, we utilize a processing method based on electrostatic deposition of microparticles and dry etching [14] to generate silicon surfaces with random 'hillock' features. The versatility of both electrostatic deposition and dry etching make the process applicable to many substrates. Microscale adhesive and friction forces of the processed surfaces are measured and compared to that of flat (unprocessed and smooth) silicon surfaces.

Experimental details

Materials and surface processing

The surface engineering process used to modify surface structure is shown schematically in Fig. 1. We used n-type (100) silicon wafers from Virginia Semiconductor, Inc. (Fredericksburg, Virginia) as substrates. Wafers were cut to coupons around 2×3-cm^2. The samples were cleaned using acetone and 18-MΩ MilliQ water in ultrasonic tank before immerging into Piranha etch (3:1 solution of H_2O_2 and H_2SO_4) for at least 1 hour. This would
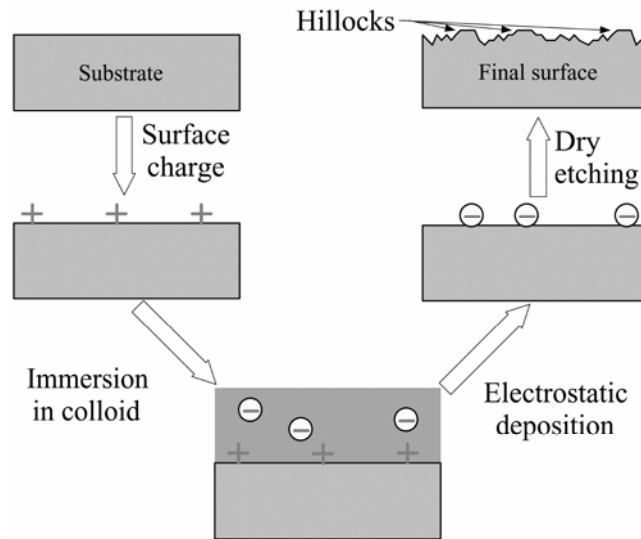
Figure 1. Surface engineering process based on electrostatic deposition of microparticles and dry etching to realize random rough surfaces with reduced contact area. A silicon substrate and a silica colloidal solution with 20 μm diameter particles were used in our experiments.

generate negatively charged thin oxide layer on silicon samples. The negatively charged coupons were subsequently immersed into 0.1mM Poly (diallyldimethyl ammonium) chloride (PDDA) (Sigma-Aldrich, St. Louis, MO) for 5 min, then rinse in MilliQ water for 5 min to remove excessive PDDA, leaving behind a polycation monolayer on top of the silicon substrate. A silica colloidal solution was used. The colloid was obtained by sonicating MilliQ water and silica spheres (18 – 22 μm in diameter, average = 20 μm) from GFS chemicals, Inc (Powell, Ohio). In the colloid, silica spheres are negatively charged. By immersing silicon samples with PDDA polycationic layer into the colloid, negatively charged silica spheres are randomly attracted to samples via electrostatic attraction. By varying immersion time, the coverage of silica spheres can be modified [14]. After immersion, the samples were dipped into acetone and vibrated for 2 minutes to remove loosely held silica spheres prior to being dried in air. Subsequent dry etching was performed using deep reactive ion etching (DRIE, Alcatel) with SF_4 and C_4F_8 during which the silica spheres acted as masks. Then samples
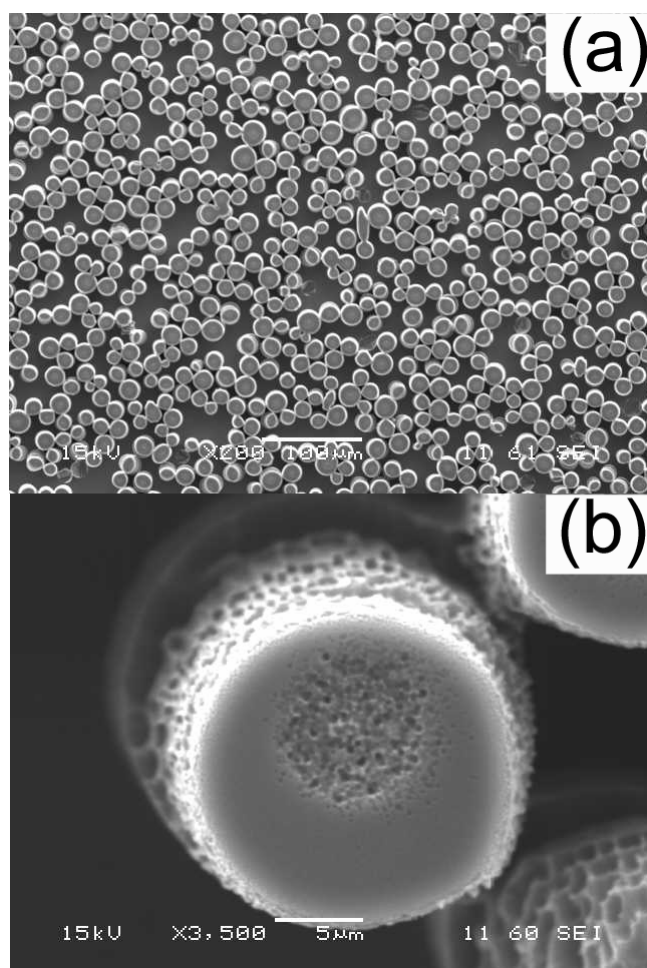
Figure 2. A scanning electron microscope image of (a) final etched surface with hillock features (scale bar is 100 mm) and. (b) details of a hillock surface which displays nanoscale roughness due to the etching process.

were rinsed in acetone and Piranha etch to remove any remaining photoresist to yield the final surface with 'hillock' features at the locations of the particles as shown in Figure 2. Figure 2 (a) shows a surface obtained using the 20 μm-diameter particles at 57% particle coverage that was used in this study. The heights of the hillock showed very little variation and were around 25 μm. The average hillock diameter was about 15 μm, which is slightly lower than the average particle size used due to slight undercutting during the etching process. Although a large proportion of the hillocks exhibited diameters close to this average value, some hillocks showed diameters ranging from 10 – 30 μm, most likely due to the variation in

particle size. The hillock size and height can thus be easily modified by varying the particle size and dry etching time. The authors have shown that the autocorrelation length of the final surface can be tuned as well by varying particle coverage and size [14]. The autocorrelation length of the processed surface in this study was measured to be around 3 μm. Figure 2(b) shows a close-up of the top surface of each hillock. The top of the hillocks are relatively flat with some regions exhibiting nanoscale roughness (RMS ~ 70 nm) caused by the dry etching process.

Adhesion and friction tests

Adhesion and friction tests were conducted on flat and processed silicon samples using a home-built reciprocating microtribometer with a normal load resolution of 15 μN and a lateral load resolution of 5 μN [15]. The probe was a thermoplastic rubber (Santoprene) ball with a diameter of 0.164 inch (Hoover Precision Products, Cumming, GA). Santoprene was used as the probe material to take advantage of its small Young's modulus and realize a large area of contact under the small normal loads used. A large contact area is necessary in order to cover enough hillock features and hence capture any effect on the contact area. Assuming elastic deformation and Hertzian contact mechanics [16], a lower limit of the contact radius (r) between the spherical probe and substrate can be estimated according to the following equation,

$$r = \left(\frac{3PR^*}{4E^*} \right)^{1/3} \qquad\qquad \textbf{1}$$

where P is the normal load, R^* is the equivalent radius given by R in this case, and E^* is the equivalent Young's modulus given by $E^* = \left[(1-v_1^2)/E_1 + (1-v_2^2)/E_2 \right]^{-1}$, where E_1, E_2 and v_1, v_2 are Young's modulus and Poisson's ratio for tip and substrate, respectively. As a thermoplastic elastomer, Santoprene has a Poisson's ratio around 0.5 and Young's modulus around 113 MPa at small strains according to the manufacturer. The values of Poisson's ratio

and Young's modulus used for silicon are 0.234 [17] and 178.6 GPa [17] respectively. The calculations resulted in a contact radius exceeding 50 µm for normal loads of 10 mN and higher. Keeping in mind that this is a lower bound, the contact area afforded by the probe should be large enough to include a significant number of the 15 µm-sized features of the processed surface.

For the adhesion test, the Santoprene ball was mounted onto a cantilever and vertical motion of the cantilever was controlled with step motors. The contact force is controlled by varying cantilever displacement and approach and retract velocities were set to be equal using the LabVIEW-based user interface. The pull-off force was obtained from the retracting force curve as the difference between the minimum force value and the baseline (far-field) value. For the friction tests, a stroke length of 10 mm was used with a speed of 0.6 mm/s. The normal load was linearly increased from 0 to 10 mN during each stroke. In order to minimize any water meniscus effects, all experiments were conducted in a nitrogen atmosphere inside an environmental chamber with relative humidity less than 6% and at a room temperature of 25 °C.
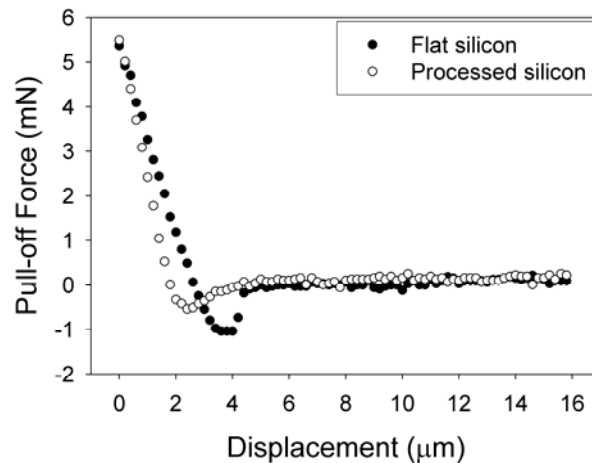

Figure 3. Typical retracting force curves between Santoprene probe and silicon surfaces at a retracting speed of 0.01 mm/s.

Results and discussions

Adhesion

Typical retracting force curves at a retracting velocity of 0.01 mm/s for the flat and processed sample are shown in Fig. 3. The processed sample generally showed lower adhesion than the flat sample, particularly at higher peak loads, as shown in Fig. 4. This can be attributed to the reduction of real area of contact between the Santoprene ball and the processed sample. When contacting with a rough substrate, a rubber probe can deform to form complete contact with the rough interface [18], filling in all the valleys. For relatively flat surfaces such as unprocessed silicon in our study, complete contact is achieved at even the lowest loads. For a rough surface whose roughness is approximated as a sine wave with amplitude 2h and wavelength λ, the required perpendicular pressure for complete contact can be estimated as $\sigma_0 = hE/\lambda$, where E is the Young's modulus for the rubber [18]. Applying this model to the processed, surface, the coverage p_1 of n hillocks of diameter d along a profile L can be calculated as $p_1 = nd/L$.. The wavelength λ, represented by L/n can then be estimated to be $d/p \sim 26$ μm, using d = 15 μm and p_1 = surface coverage p (0.57). Since the hillock heights are known (2h = 25 μm), the required perpendicular pressure for complete contact is estimated to be around 54 MPa. This value is much higher than the average pressure of 4.7 MPa estimated based on Hertzian contact mechanics under the maximum normal load 350 mN. Since the rubber does not make complete contact for the processed silicon surface, the lower pull-off force observed can be attributed to the fact that the presence of hillocks reduces the real area of contact with the probe. It is noted that the extent of complete contact can be easily tailored using the microparticle-based method by decreasing the coverage of hillocks and reducing dry etching time. It is also noted that the rubber probe probably makes complete contact with the tops of the hillocks including the regions with nanoscale roughness.
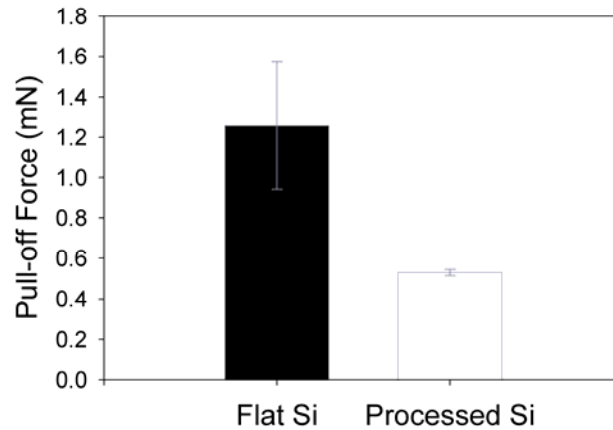
Figure 4. Pull-off forces measured on flat and processed silicon sample under peak load of 350 mN and retracting velocity of 0.01 mm/s.

For both flat and processed samples, it was found that the measured pull-off forces were a function of both the retracting velocity and the peak load. Rate dependent pull-off forces have been reported before [19], but we found it difficult to reliably distinguish the effects caused by the probe-sample interaction forces (adhesion) from the artifact caused by the stiffness of the cantilever [20], especially under high retracting velocities. To minimize any dynamic artifacts associated with the stiffness effect, we choose to use a very low retracting velocity of 0.01 mm/s. Under these conditions, the pull-off force can be considered to be representative of the probe-sample adhesion. At small retracting velocity, we found that the measured pull-off (adhesive) forces increased with an increase of the peak load. This may be attributed to the contact hysteresis effect between loading and unloading. Under higher peak load, the maximum real area of contact between the Santoprene ball and substrate increases and hence the probe deformation is larger than at smaller loads. The larger deformation may not be completely recovered at zero load, which can lead to higher contact area and hence a larger pull-off force due to increase adhesive interaction.

For the flat silicon sample, the Johnson-Kendall-Roberts (JKR) contact model can be used to describe the adhesion behavior between the smooth Santoprene ball and the flat
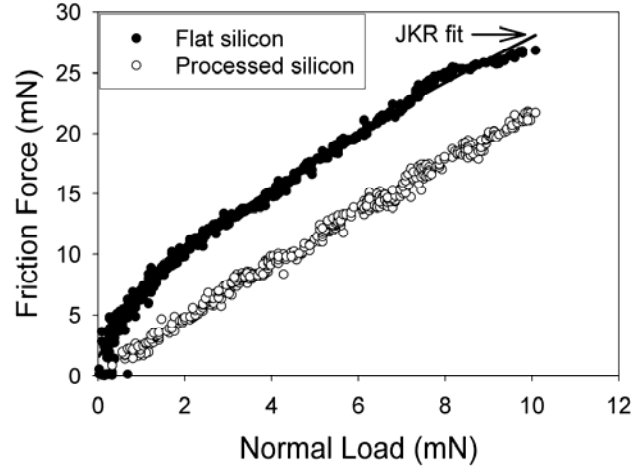
Figure 5. Friction force as a function of normal load for flat and processed silicon samples measured using a Santoprene probe. The friction response for the flat sample is non-linear and fits the JKR model quite well. The friction response of the processed silicon is linear according to Amonton's law.

silicon sample [21]. It is noted that the JKR model is not valid for the processed surface due to the significant roughness. According to the JKR model, the pull-off force depends only on interface energy and contact radius [22]. A rough estimation of the work of adhesion, w_{12}, between Santoprene and silicon can then be calculated based on the JKR model [22] as follows:

$$w_{12} = -2F_m /(3\pi R) \qquad\qquad \textbf{2}$$

where R is the ball radius and F_m is the separation force observed on the flat sample. The separation force under zero normal load F_m was estimated to be 0.32 mN, which was the pull-off force measured at the smallest peak normal load value (25 mN) that yielded pull-off forces above the noise level. This estimation is a little lower than Fuller and Tabor's measurement with a rubber ball on a Perspex plate [20] (1.4 mN for a ball with radius of 7.3 mm).

The calculation based on Eq. 2 yielded a w_{12} value of around 0.033 N/m, which falls in the range of typical van der Waals interaction energies [23]. We note that the actual

contact behavior of the interface may be much more complex and that a single parameter, like work of adhesion, may not be able to completely characterize the viscoelastic contact between the Santoprene ball and the silicon samples [24]. Furthermore, the work of adhesion can be a function of the unloading rate [19, 25].

Friction

Friction forces as a function of normal load for the two samples are shown Fig. 5. The processed sample clearly shows lower friction force than the flat samples. The high values of coefficients of friction observed (>2) are common for interfaces between rubber and hard surfaces, especially at low normal load and have been commonly reported [18, 26]. The friction force between rubber and a rough(hard) surface has two contributions commonly described as adhesion and hysteretic components [18, 27]. The adhesion component is significant especially at low loads, which is the case for our experiments. As discussed in the previous section, the adhesive component is lower for the processed sample due to the reduction in real area of contact as compared to the flat silicon sample. For a given sliding speed and material interface, the magnitude of the hysteretic component has been theoretically shown to generally increase with an increase in roughness of the hard substrate [18], except at extreme levels of roughness where it decreases. Assuming that the roughness of the processed silicon results in an increased hysteretic component compared to the flat silicon, the fact that the observed friction response of the processed silicon is lower than the flat silicon suggests that the adhesion component dominates the friction behavior, which is expected at our low loads.

If we assume an adhesive friction model for the contact between the elastomer and the flat sample, the friction force depends on both the interfacial shear stress and the real area of contact [28]. For a constant interfacial shear strength, the real area of contact and hence the friction force varies non-linearly with applied load for flat samples and can be predicted

by adhesion-based contact models such as the JKR model [21]. For rough surfaces, the friction force has been known to follow a linear dependency on normal load (Amontons' law) [29]. The experimental results are exactly consistent with these predictions as shown in Fig. 5 by the non-linear friction response of the flat silicon sample and the linear response of the processed (rough) silicon. Using the above estimated work of adhesion between Santoprene and silicon (w_{12}), the friction force (F_f) for the flat sample can be calculated based on JKR model [22] according to:

$$
\begin{aligned}
F_f = \tau A &= \tau \pi \left(\frac{3R^*}{4E^*} \right)^{2/3} P_{JKR} \\
&= \tau \pi \left(\frac{3R^*}{4E^*} \right)^{2/3} \left(P + 3\pi w_{12} R^* + \sqrt{6\pi w_{12} R^* P + (3\pi w_{12} R^*)^2} \right)^{2/3}
\end{aligned}
\qquad \textbf{3}
$$

where τ is the interfacial shear strength and P is the applied normal load. A nonlinear curve fit of the friction data on the flat sample gives $F_f = 0.564 P^{2/3}$ with an R^2 value of 0.9895, as plotted in Fig. 5. This fit yields a value of 3.8 MPa for the interfacial shear strength. This value seems reasonable when compared to values of 2-14 MPa reported for polyethylene samples [30] Our analysis assumed that the interfacial shear strength is constant and have assumed no load dependency as is sometimes assumed by researchers [31]. The coefficient of friction for the rough sample obtained using a linear fit was found to be 2.13.

Conclusions

In summary, electrostatic deposition of microparticles and dry etching were used to generate silicon surfaces with random hillock features. A Santoprene probe was used to capture the effect of the hillock features on the contact area. Both adhesion and friction measurements showed a reduction for the engineered surface comparing to flat surface. The static work of adhesion between the Santoprene probe and a silicon sample was estimated from the pull-off forces at low speed between the probe and flat silicon using JKR contact

theory. The work of adhesion between Santoprene ball and silicon substrate was calculated as 0.033 N/m and the interfacial shear strength of Santoprene was estimated to be 3.8 MPa.

Acknowledgements

References

[1]   B. Bhushan (Ed.). **Tribology Issues and Opportunities in MEMS**. Norwell, MA: Kluwer Academic Publishers; 1997.

[2]   M.J. Madou: Fundamentals of Microfabrication. 2nd edn. Boca Raton, Florida: CRC Press; 2002.

[3]   R. Maboudian and R.T. Howe, Tribology Letters 3 (1997) 215.

[4]   F.E. Kennedy, D. Lidhagen, A. Erdemir, J.B. Woodford and T. Kato, Wear 255 (2003) 854.

[5]   R. Maboudian, W.R. Ashurst and C. Carraro, Sensors and Actuators A Physical 82 (2000) 219.

[6]   Y. Zhang and S. Sundararajan, Journal of Applied Physics 97 (2005) 10356.

[7]   D.J. Whitehouse and J.F. Archard, Proceedings of the Royal Society of London, Series A, Mathematical and Physical Sciences 316 (1970) 97.

[8]   J.A. Greenwood and J.B.P. Williamson, Proceedings of the Royal Society of London, Series A, Mathematical and Physical Sciences 295 (1966) 300.

[9]   B.N.J. Persson, Physical Review Letters 87 (2001) 116101.

[10]   C.-C. Lee and W. Hsu, Journal of Vacuum Science & Technology B: Microelectronics and Nanometer Structures 21 (2003) 1505.

[11]   A. Kovalchenko, O. Ajayi, A. Erdemir, G. Fenske and I. Etsion, Tribology International 38 (2005) 219.

[12]   H.W. Deckman and J.H. Dunsmuir, Applied Physics Letters 41 (1982) 377.

[13]   R.K. Iler, Journal of Colloid and Interface Science 21 (1966) 569.

[14]   Y. Zhang and S. Sundararajan, Applied Physics Letters Accepted (2006)

[15]   J. Check, K.S.K. Karuppiah and S. Sundararajan, J Biomed Mater Res Part A 74A (2005) 687.

[16]   K. Johnson, Wear 190 (1995) 162.

[17]   Y. Matsuoka, Y. Yamamoto, K. Yamada, S. Shimada, M. Tanabe, A. Yasukawa and H. Matsuzaka, Journal of Micromechanics and Microengineering 5 (1995) 25.

[18]   B.N.J. Persson, Journal of Chemical Physics 115 (2001) 3840.

[19]   M. Ruths and S. Granick, Langmuir 14 (1998) 1804.

[20]   K.N.G. Fuller and D. Tabor, Proceedings of the Royal Society of London, Series A, Mathematical and Physical Sciences 345 (1975) 327.

[21]   J.N. Israelachvili: Intermolecular & Surface Forces. 2nd edn. San Diego: Elsevier Academic Press; 1991.

[22]   K.L. Johnson, K. Kendall and A.D. Roberts, Proceedings of the Royal Society of London, Series A, Mathematical and Physical Sciences 324 (1971) 301.

[23]   Y. Zhao, T. Tong, L. Delzeit, A. Kashani, M. Meyyappan and A. Majumdar, Journal of Vaccum Science and Technology B 24 (2006) 331.

[24]   Y.Y. Lin, C.Y. Hui and J.M. Baney, Journal of Physics D 32 (1999) 2250.

[25]   S. Perutz, E.J. Kramer, J. Baney, C.Y. Hui and C. Cohen, Journal of Polymer Science B 36 (1998) 2129.

[26]   **Coefficient of Friction - Santoprene Thermoplastic Vulcanizate Versus Steel, Aluminum and Polypropylene.** Manufacturer's specifications.

[27]   B.N.J. Persson, Surface Science 401 (1998) 445.

[28]   O. Ronsin and K.L. Coeyrehourcq, Proceedings of the Royal Society of London, Series A, Mathematical and Physical Sciences 457 (2001) 1277.

[29]   J.F. Archard, Proceedings of the Royal Society of London, Series A, Mathematical and Physical Sciences 243 (1957) 190.

[30]   B.J. Briscoe and D. Tabor, J Adhes 9 (1978) 145.

[31]   D.H. Gracias and G.A. Somorjai, Macromolecules 31 (1998) 1269.

CHAPTER 6. A HYBRID SURFACE ENGINEERING PROCESS TO GENERATE SUPERHYDROPHOBIC SURFACES WITH TUNABLE ROUGHNESS

A paper submitted to *Advanced Materials*

Yilei Zhang and Sriram Sundararajan

Department of Mechanical Engineering, Iowa State University, Ames, Iowa, 50011

Abstract

A versatile hybrid processing method that combines electrostatic deposition of microparticles and subsequent anisotropic plasma etching is described that can generate superhydrophobic engineering surfaces with tunable bimodal roughness and a thin hydrophobic fluorocarbon film. These surfaces exhibit contact angles with water of more than 160°.

Keywords: surface patterning, biomimetics, superhydrophobicity

Introduction

Superhydrophobic (super-water repellant) surfaces are found in nature on the leaf surfaces of many plants such as the lotus and colrabi[1]. These surfaces also exhibit self-cleaning capability by which rolling water droplets remove dirt and debris from their surfaces. Therefore, efforts to fabricate artificial superhydrophobic surfaces (exhibiting water contact angle greater than 150°) have received much attention, motivated by both fundamental research and their potential use in practical applications. The wetting behavior of superhydrophobic surfaces is governed by both their chemical composition and geometric microstructure. A careful check shows that lotus leaf has a combination of binary roughness structure (at the 10 - 20 μm and nano meter scale respectively) and epicuticular wax layer[1]. Both micro and nano scale roughness are helpful in increasing contact angle [2].

Several methods have been employed to generate engineering surfaces that can mimic the structure and chemistry of natural superhydrophobic surfaces [3]. Polymer coatings or layer-by-layer deposited particles with both low surface energy and micro structures can be attached to the bulk to achieve superhydrophobic properties[4-9]. Microfabrication techniques are widely used to generate predetermined micro roughness while aligned carbon nanotubes have been utilized for nano scale roughness [10, 11]. Since many engineering materials are hydrophilic, a further step is needed to coat the roughened substrates with a hydrophobic layer self assembled monolayers [12], polymer films[13] or diamond-like carbon films[14]. It is of interest to develop processing methods that allow a high degree of control over the resulting surface structure and that can simultaneously impart hydrophobicity to render a material superhydrophobic.

In this communication we describe a hybrid process, outlined in Fig. 1, which combines electrostatic deposition of particles and subsequent anisotropic plasma etching to generate superhydrophobic surfaces. The versatility of electrostatic deposition and plasma processing makes this process attractive to a wide range of substrates. During the etching process, particles on the surface act as temporary masks that result in microscale "hillock"-like features on the substrate. A nanoscale roughness typically seen when etching flat substrates using this process [15] will also be superimposed onto the hillocks. Controlling the particle size, particle coverage and etch time thus provide the ability to tune the amplitude and spatial roughness parameters [16] and hence the structure of the resulting surfaces. During the passivation process of the etch, C_4F_8 feed gas is ionized to form C_xF_y free radicals such as CF_2, CF_3 etc., which diffuse to the substrate and polymerize to form a thin Teflon-like fluorocarbon film[17]. This fluorocarbon film is hydrophobic, with contact angles of 109° having been reported on flat silicon[17]. These thin fluorocarbon coatings provide complete and uniform coverage at the nanoscale[18]. Uniformity in coating thickness and coverage can be enhanced by introducing a long passivation process at the end of the etch process.
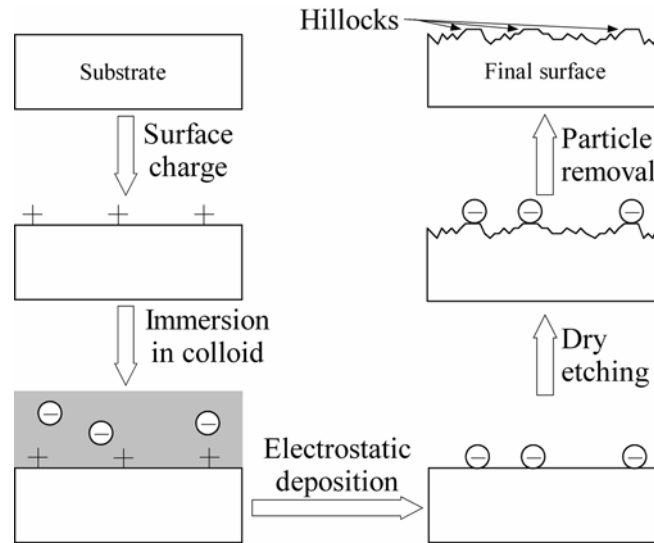
Figure 1. Surface engineering process based on electrostatic deposition of microparticles and anisotropic plasma etching to realize superhydrophobic surfaces. A silicon substrate and a silica colloidal solution with 20 μm diameter particles corresponding to microscale feature size found in lotus leaves were used in our experiments.

Surface properties

Figure 2 (a) shows the topography of final surfaces generated with 20 μm diameter silica particles at a coverage of around 57% obtained using scanning electron microscopy. The 'hillock'-like structures formed as a result of the particle masking during etching have an average diameter of about 15 μm. This is smaller than the average particle size used and may be caused by undercutting during the etching process due to the fact that the edges of silica spheres do not contact with substrates directly. Some hillocks showed diameters ranging from 10 to 30 μm, which most likely due to the variation in particle size. These 'hillocks' thus constitute a microscale roughness controlled by particle size and coverage. Details of a single hillock top surface show the presence of nanoscale features generated during plasma etching cycles as shown in Fig. 2 (b). The generated surfaces thus show a binary roughness structure similar to a lotus leaf structure.
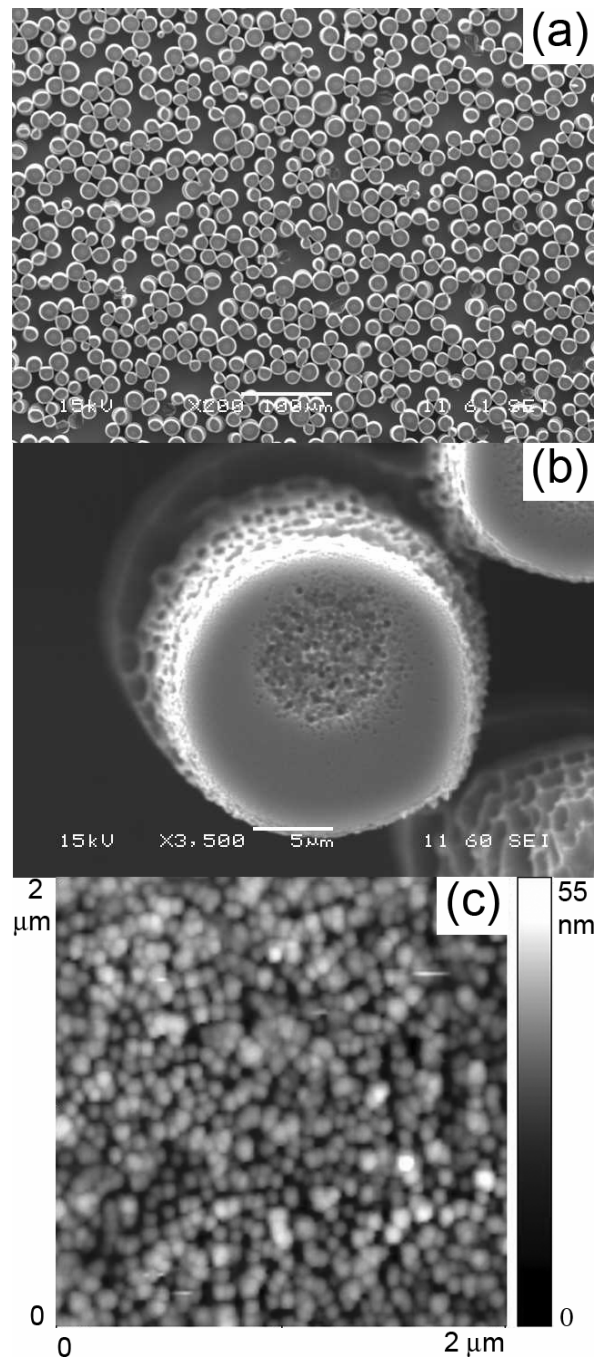
Figure 2. A scanning electron microscope image of (a) typical final etched surface with hillock features (scale bar is 100 μm) and (b) details of a single hillock which displays nanoscale roughness on the surface due to the etching process. (c) An atomic force microscopy topographical image of the nanoscale roughness on the hillock surface (RMS roughness = 6.37 nm for a 1×1 μm scan size).

Interestingly, there is an increased nanoscale roughness that is typically confined to a circular area on top of hillocks. Roughness outside the circular area is small with a root mean square around 2.03 nm for 1 μm scan size, which is comparable to the roughness of flat silicon surfaces etched using anisotropic plasma etching [15]. This implies that etching occurs underneath the particles. Roughness inside the circular area is much larger, and the root mean square is around 6.37 nm over a 1 μm scan size. Details of the topography inside this circular area are shown in Fig. 2 (c). Most of these roughened circular areas were observed near the centers of the hillocks, and therefore lead us to believe that they correspond to the areas under the centers of the particles during the etching process. Upon closer inspection, each circular area appears to consist of several concentric rings as shown in Fig. 3 (a). With an increase in etching time, the rings become broader and finally connect together to form the circular rough area. Fig. 3 (b) shows a cross section of the ring pattern, where the center is the deepest and the second deepest ring is located around 1.2 μm from the center. The largest ring has a diameter around 6 μm for 20 μm silica spheres. This ring structure is not common in routine plasma etching. We believe that the structure is the result of electron diffraction caused by the silica spheres during the etching process. Similar to optical diffraction, electrons may follow a Fresnel diffraction around a micro-sphere, leading to increased electron intensity on the silicon substrate beneath the sphere to form the pattern with concentric rings. The center of those rings has the highest electron intensity, similar to the bright spot (Poisson's spot) in the shadow of a sphere in a light beam. Since electrons enhance the reaction involved in silicon removal, higher electron intensity leads to more material removed [19], as demonstrated by the topography of the ring structures in Fig. 3. However this phenomenon requires a more careful study to fully understand the mechanisms involved.
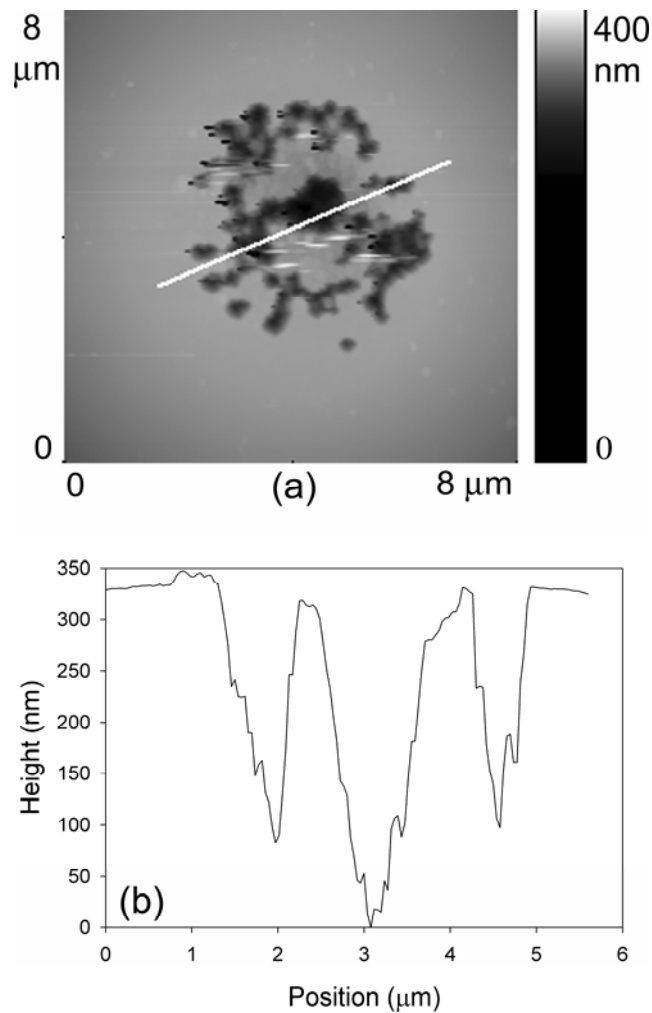
Figure 3. (a) AFM image of a hillock top which exhibits a ring pattern with increased roughness; (b) cross section of the ring pattern, which shows that the regions at the center and at a concentric ring are much deeper than area between and outside them.

Superhydrophobicity

Figure 4 shows the observed water contact angle behavior of the surfaces as a function of the key processing variables of particle size, particle coverage and etch depth, which directly affect size, coverage and height of the hillocks on the final surface. The figure shows that at higher coverage, contact angles as high as 160° are observed, which fall in the superhydrophobic region. Particle coverage appears to have the most significant impact on
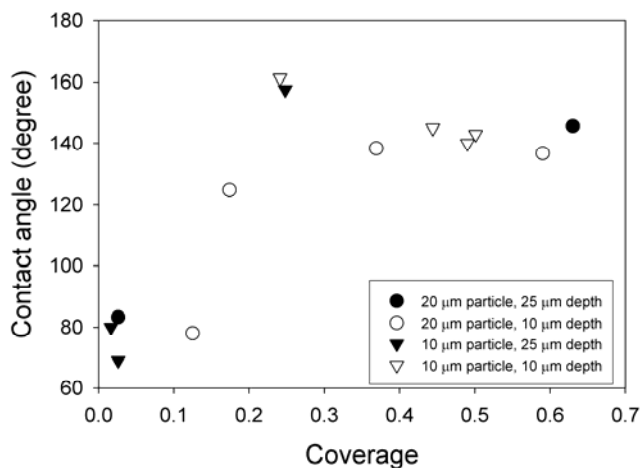
Figure 4. Water contact angle of the processed surfaces as a function of particle coverage, size and etch depth.

the observed contact angle behavior. There exists a threshold value of particle (hillock) coverage below which contact angle drops to around 70°. The superhydrophobic behavior observed is attributed to suspension of the water droplets and air trapping under the droplet caused by the binary roughness structure in conjunction with the hydrophobic CF_x coating. The failure to form air trapping at lower hillock coverage is believed to cause the sharp decrease in observed contact angles. Lower values of hillock coverage result in a lower density of hillocks and larger inter-hillock distances, which make it harder for droplet surface tension to support its weight. Based on our former work, lower particle coverage will lead to larger autocorrelation lengths of the final surfaces[16], which results in fewer peaks on the surfaces[20]. This implies that autocorrelation length could be utilized to model air trapping ability of hydrophobic rough surfaces and is a topic of our current study.

The range of particle (hillock) size investigated (10 and 20 µm) did not have any appreciable effect on contact angle. The apparent contact angle of a wafer droplet on a rough surface is controlled by interactions at the contact perimeter of a droplet rather than the contact area [21-23]. Interaction at the contact perimeter depends on several factors, such as perimeter length, rising angle of peaks along the perimeter, and lengths of air-liquid and

solid-liquid interfaces along the perimeter. Due to the random distribution of hillocks on the surface, the droplet perimeter should remain a circle and will not change appreciably with the size of the individual hillocks. Anisotropic plasma etching leads to a rising angle value of around 90° for all hillocks. At a constant coverage of the hillocks, varying hillock size may vary the number of solid-liquid or air-liquid contact regions, but will not change the ratio of their length along the perimeter [16]. We believe all these factors contribute to the comparable contact angles observed as a function of hillock size in our experiment. Varying etching depth from 10 to 25 μm does not affect contact angle very much. This suggests that a 10 μm depth is sufficient for air trapping, and a further increase is inconsequential. This observation is similar to the results reported using an SU-8 patterned surface, which suggests that pillar height above 15 μm will not change contact angle [24].

Conclusion

In conclusion, we have developed a novel surface engineering process that combines electrostatic deposition of particles and anisotropic plasma etching to generate superhydrophobic surfaces with binary roughness structure and a hydrophobic coating. Microscale particles act as a mask during etching to generate micro-scale roughness. They also cause electron diffraction to enhance the nanoscale roughness generated on top of the micron-scale features. The passivation processes during plasma etching produce a hydrophobic fluorocarbon layer on the surface. The combination of binary roughness structure and fluorocarbon layer shows water contact angles as high as 160°. Particle coverage studies show that there is a threshold value (~ 15% coverage) to sustain air trapping under droplets, which is believed to be the mechanism causing the observed superhydrophobic behavior.

Experimental

The details of the process are described as follows using a silicon substrate. First, a clean Si(100) surface with a negatively charged native oxide layer is achieved using a Piranha etch (3:1 solution of H_2O_2 and H_2SO_4). Next, a poly (diallyldimethyl ammonium) chloride (PDDA) monolayer was deposited onto the Si (100) surface via dip-coating to form a polycationic layer. Silica spheres with an average diameter of 20 μm were mixed with MilliQ water and sonicated for 20 minutes to form a colloidal solution into which the silicon substrate was immersed. This particle size corresponds to the micro scale feature size seen on lotus leaves[1]. The negatively charged silica particles are randomly attracted to the positively charged PDDA monolayer on the silicon surface. After immersion, the samples were rinsed in MilliQ water flow for 5 minutes to remove loosely held silica particles and dried in clean nitrogen flow to ensure that a monolayer of randomly dispersed particles remained on the substrate. The substrate was then etched using the Bosch process[25] (anisotropic plasma etch with $C_4F_8 + SF_6$ gases) in a deep reactive ion etch (DRIE, Alcatel 601E) chamber for a total time so as to achieve etch depths of tens of microns. Any remaining silica particles were then removed using 49% hydrofluoric acid followed by MilliQ water rinsing. The process variables that affect the final surface topography are particle size, particle coverage and etch depth. Particle sizes varying from nanometers to micrometers are commercially available or can be synthesized in a laboratory. The coverage of particles on the substrate can be varied by controlling the immersion time[26]. In our studies, the coverage typically increased linearly with an increase in immersion time. Etch depth can be well controlled by appropriately selecting etch conditions and time.

Topography of generated surfaces was obtained using scanning electron microscopy, SEM (JEOL JSM-606LV) without any conductive coating. Details of hillock topography were obtained using an atomic force microscope, AFM (Dimension 3100, Vecco Instruments, Santa Barbara, CA) in contact mode with a commercial Si_3N_4 probe (radius ~ 50 nm) at a

scan size of 60 μm ✖ 60 μm with 256 ✖ 256 data points. All surface roughness parameters reported were obtained from the AFM images. Contact angles were measured by taking high magnification digital pictures of 8 μL MilliQ water droplets on each sample using a CCD camera.

Acknowledgements

References

[1]   W. Barthlott, C. Neinhuis, *Planta* **1997**, *202*, 1.

[2]   Y. T. Cheng, D. E. Rodak, C. A. Wong, C. A. Hayden, *Nanotechnology* **2006**, *17*, 1359.

[3]   X. J. Feng, L. Jiang, *Advanced Materials* **2006**, *18*, 3063.

[4]   J. Ji, J. Fu, J. Shen, *Advanced Materials* **2006**, *18*, 1441.

[5]   S. Wang, L. Feng, L. Jiang, *Advanced Materials* **2006**, *18*, 767.

[6]   N. Zhao, J. Xu, Q. D. Xie, L. H. Weng, X. L. Guo, X. L. Zhang, L. H. Shi, *Macromolecular Rapid Communications* **2005**, *26*, 1075.

[7]   G. Zhang, D. Y. Wang, Z. Z. Gu, H. Mohwald, *Langmuir* **2005**, *21*, 9143.

[8]   Q. D. Xie, G. Q. Fan, N. Zhao, X. L. Guo, J. Xu, J. Y. Dong, L. Y. Zhang, Y. J. Zhang, C. C. Han, *Advanced Materials* **2004**, *16*, 1830.

[9]   A. Nakajima, A. Fujishima, K. Hashimoto, T. Watanabe, *Advanced Materials* **1999**, *11*, 1365.

[10]   L. B. Zhu, Y. H. Xiu, J. W. Xu, P. A. Tamirisa, D. W. Hess, C. P. Wong, *Langmuir* **2005**, *21*, 11208.

[11]   K. K. S. Lau, J. Bico, K. B. K. Teo, M. Chhowalla, G. A. J. Amaratunga, W. I. Milne, G. H. McKinley, K. K. Gleason, *Nano Letters* **2003**, *3*, 1701.

[12]   J. Genzer, K. Efimenko, *Science* **2000**, *290*, 2130.

[13]   A. Hozumi, O. Takai, *Thin Solid Films* **1997**, *303*, 222.

[14]   R. Hatada, K. Baba, *Nucl. Instrum. Methods Phys. Res. Sect. B-Beam Interact. Mater. Atoms* **1999**, *148*, 655.

[15]   S. Chandrasekaran, S. Sundararajan, *Surface & Coatings Technology* **2004**, *188*, 581.

[16]   Y. Zhang, S. Sundararajan, *Applied Physics Letters* **2006**, *88*, 141903.

[17]   Y. X. Zhuang, A. Menon, *Journal of Vacuum Science & Technology A: Vacuum, Surfaces, and Films* **2005**, *23*, 434.

[18]   P. P. Joshi, R. Pulikollu, S. R. Higgins, X. M. Hu, S. M. Mukhopadhyay, *Appl. Surf. Sci.* **2006**, *252*, 5676.

[19]   J. W. Coburn, H. F. Winters, *Journal of Vacuum Science & Technology* **1979**, *16*, 391.

[20]   Y. Zhang, S. Sundararajan, *Journal of applied physics* **2005**, *97*, 10356.

[21]   F. E. Bartell, J. W. Shepard, *Journal of Physical Chemistry* **1953**, *57*, 211.

[22]   C. W. Extrand, *Langmuir* **2002**, *18*, 7991.

[23]   C. W. Extrand, *Langmuir* **2003**, *19*, 3793.

[24]   N. J. Shirtcliffe, S. Aqil, C. Evans, G. McHale, M. I. Newton, C. C. Perry, P. Roach, *Journal of Micromechanics and Microengineering* **2004**, *14*, 1384.

[25]   M. J. Madou, *Fundamentals of Microfabrication*, CRC Press, Boca Raton, Florida **2002**.

[26]   Z. Adamczyk, L. Szyk-Warszynska, M. Zembala, M. Lehocky, *Colloids and Surfaces A: Physicochem. Eng. Aspects* **2004**, *235*, 65.

CHAPTER 7 GEOMETRICAL MODELING OF AIR-TRAPPING ON HYDROPHOBIC SURFACES GENERATED USING A HYBRID SURFACE PROCESS

Yilei Zhang and Sriram Sundararajan

Department of Mechanical Engineering, Iowa State University, Ames, Iowa, 50011

Abstract

Air-trapping is cognized as an important mechanism to increase the contact angle of hydrophobic surfaces leading to conditions of superhydrophobicity. The increased contact angle supported by air-trapping is often modeled by introducing an area fraction according to Cassie and Baxter's model, but the model does not predict under which conditions air-trapping is possible. In this paper a geometric model for sustained air-trapping on rough hydrophobic surfaces is presented. The rough surface is modeled as discrete hillock features and three process variables (hillock diameter, coverage and etching depth) as well as contact angle on flat surface are included in the model. Experimental prediction of minimum hillock coverage required for superhydrophobic behavior agrees reasonably well with model predictions.

Introduction

Superhydrophobic (super-water repellant, water contact angle $> 140^{\circ}$) surfaces are found in nature on the leaf surfaces of many plants such as the lotus and colrabi[1]. These surfaces also exhibit self-cleaning capability by which rolling water droplets remove dirt and debris from their surfaces. Several methods have been employed to generate engineering surfaces that can mimic the structure and chemistry of natural superhydrophobic surfaces [2-15]. Polymer coatings or layer-by-layer deposited particles with both low surface energy and micro structures can be attached to the bulk to achieve superhydrophobic properties.

Microfabrication techniques are widely used to generate predetermined micro roughness while aligned carbon nanotubes have been utilized for nano scale roughness [10,11]. Since many engineering materials are hydrophilic, a further step is needed to coat the roughened substrates with a hydrophobic layer self assembled monolayers [12], polymer films[13] or diamond-like carbon films[14]. It is of interest to develop processing methods that allow a high degree of control over the resulting surface structure and that can simultaneously impart hydrophobicity to render a material superhydrophobic. The authors have developed a hybrid processing methods based on electrostatic deposition and plasma etching that can generate lotus-like superhydrophobic surfaces[15]. The generated rough surfaces exhibit hillock-like features covered by a hydrophobic thin film. It is believed that these hillock-like features contribute superhydrophobicity via an air-trapping mechanism.

The wetting behavior of superhydrophobic surfaces is governed by both their chemical composition and geometric microstructures. The relation between contact angle and surface energy was developed by Thomas Young[16], which could be written as $\gamma_{LV}\cos\theta = \gamma_{SV} - \gamma_{SL}$, where θ is contact angle, γ_{LV}, γ_{SV} and γ_{SL} are interfacial energy for liquid-vapor, solid-vapor, and solid-liquid respectively. Obviously, no surface roughness effect was considered in Young's equation. Considering that surface roughness increases the interfacial area between solid and liquid, Wenzel proposed a correction factor r for contact angle on rough surfaces, which is equal to the ratio of rough interfacial area over flat interfacial area under the droplet[17]. Wenzel's equation for contact angle on a rough surface is as follows:

$$\cos\theta^* = r\cos\theta \qquad\qquad \textbf{1}$$

where θ^* and θ are contact angle of a droplet on a rough surface and contact angle of the same droplet on the same surface without roughness that is calculated using Young's equation. Wenzel's model assumes no air-trapping under droplet, which may not necessarily be true. Cassie and Baxter[18] built a model to estimate contact angle on rough surface with air-

trapping. They assumed that a droplt is suspended on the rough structures and allows air trapping between the rough structures on a surface underneath the droplet. They introduced an area fraction ϕ_S of liquid-solid interface to the area of the whole nominal interface. The equation could be written as the following:

$$\cos\theta^* = -1 + \phi_s(1 + \cos\theta), \qquad\qquad \textbf{2}$$

where θ^* and θ are contact angles with and without (i.e. on a flat surface) considering air-trapping.

Cassie and Baxter's model uses an area fraction as a correction factor for contact angles, but does not provide a criterion to predict whether air-trapping can occur or not. Utilizing the rather simple hillock structure and the high degree of control of hillock coverage afforded by the hybrid technique, a relation between process variables, contact angle and air-trapping ability based on geometric requirement is developed, and extended it to general rough surfaces. The model predictions are compared with experimental observations.

Surface preparation

The hybrid process is briefly described here. Details can be found in the authors' former publications[19,20]. In short, a clean silicon wafer with a negatively charged native oxide layer was achieved using a Piranha etch (3:1 solution of H_2O_2 and H_2SO_4). A poly (diallyldimethyl ammonium) chloride (PDDA) monolayer was deposited via dip-coating to form a uniformly polycationic layer. Silica spheres was mixed with MilliQ water and sonicated for 20 minutes to form a colloidal solution into which the silicon substrate is immersed. The negatively charged silica particles are randomly attracted to the positively charged PDDA monolayer on the silicon surface. The coverage of particles on the substrate was varied by controlling the immersion time. After immersion, the samples were rinsed in MilliQ water flow for 5 min to remove loosely held silica particles, and then dried in clean

nitrogen flow to ensure that a monolayer of randomly dispersed particles remained on the PDDA coated surface. Next, the samples were dry etched in a (deep) reactive ion etch ((D)RIE) chamber for desired depth. During this line-of-sight etching process, particles act as temporary masks that result in "hillock"-like features on the substrate. The remaining silica particles were then removed using 49% hydrofluoric acid. Figure 1 shows the final surface topography of two samples with different coverage (33% and 53%) obtained using a SEM. For a given particle size and etching time, all hillocks had comparable dimensions and a little
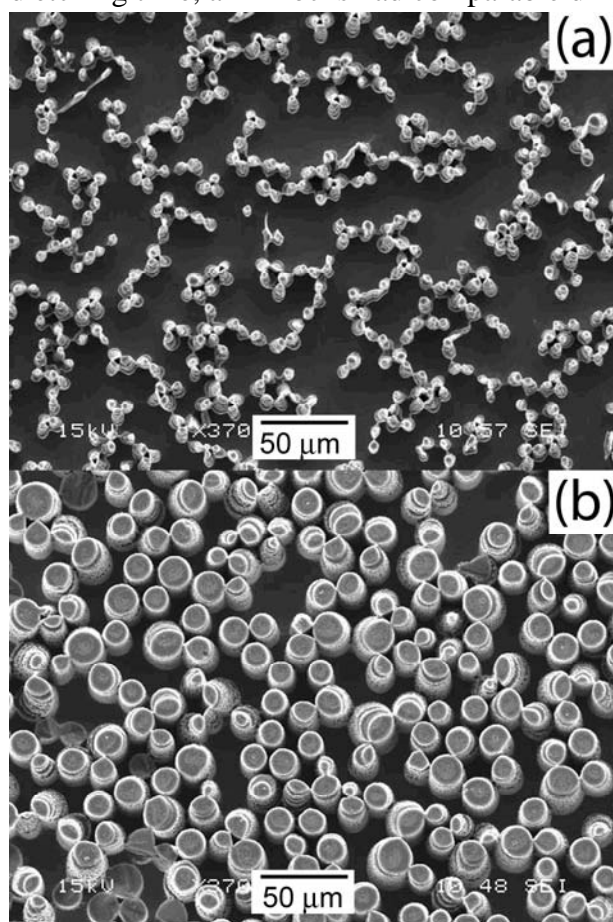
Figure 1. Scanning electron microscopy (SEM) images of final surfaces processed using silica microparticles of various diameters and using different etch depths. (a) microparticle diameter ~ 10 μm, deep reactive ion etch (DRIE) depth ~ 25 μm; (b) microparticle diameter ~ 20 μm, DRIE depth ~ 25 μm.

smaller than particle size due to undercutting. Controlling the particle size, particle coverage and etch time thus provide the ability to tune the amplitude and spatial roughness parameters [19] and hence the structure of the resulting surfaces.

During the passivation process of the etch, C_4F_8 feed gas is ionized to form C_xF_y free radicals such as CF_2, CF_3 etc., which diffuse to the substrate and polymerize to form a thin Teflon-like fluorocarbon film[21]. This fluorocarbon film is hydrophobic, with contact angles of 109° having been reported on flat silicon[21]. These thin fluorocarbon coatings are known provide complete and uniform coverage at the nanoscale[22]. Uniformity in coating thickness and coverage can be enhanced by introducing a long passivation process at the end of the etch process. Water contact angle on these surfaces can be as high as 160 degree[23], as shown in Fig.2. From Fig. 2, it can be seen that a threshold value of coverage between 3% to 15% exists, above which superhydropobic behavior is obtained. If air-trapping is considered a mechanism for this ultra-high water repellency, this threshold may be associated with the condition to sustain air-trapping. Next, an approach to model the contact angle behavior and air-trapping is described.
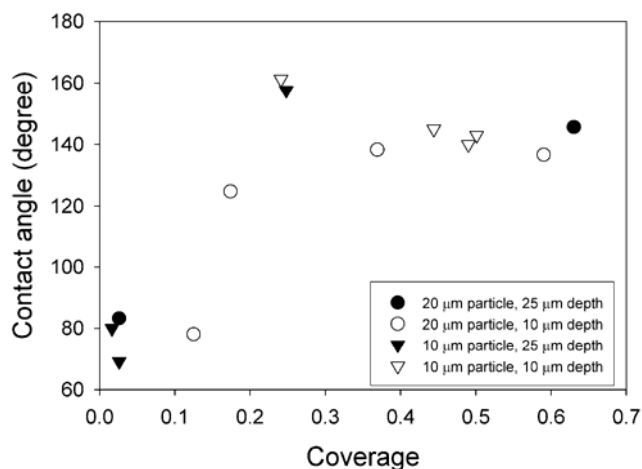
Figure 2. Contact angle of water droplet (8 μL) on hillock surfaces as a function of hillock coverage, particle size and etching depth.

Geometrical modeling

The 2D plot of the generated hillock surfaces is shown as Fig. 3. Every hillock is modeled as a pulse and a water droplet is assumed to sit on top of the hillocks. The distance between two hillocks is w, the height of hillocks is h, and hillock width is d. This kind of 2D structure has been widely used to illustrate air-trapping on a hydrophobic surface caused by roughness[24]. If a flat hydrophobic surface exhibits a water contact angle of θ, a droplet will form this same angle with the side wall as shown in Fig. 3. As the contact angle decreases, a larger portion of the droplet will occupy the well formed by a hillock and its closest neighbor. When θ reaches 90°, the diameter of the droplet will be equal to the well width, w, and exactly half of the droplet will be inside the well. This is the maximum depth (w/2) that a droplet can reach because further decrease of contact angle below 90° would mean that the sidewall is hydrophilic and the surface tension will push the droplet down to the bottom, and no air-trapping is possible. Thus, the geometric requirement for air-trapping is that the hillock height should be larger than half of the width of the well, or in other words, a minimum aspect ratio of a well for air-trapping is 0.5. Schrauth et.al developed a simple model to satisfy the aspect ratio requirement in terms of contact angle and well geometries[25], which is shown as the following equation.

$$\frac{h}{w} \geq \frac{1 - \sin\theta}{-2\cos\theta} \qquad\qquad \textbf{3}$$
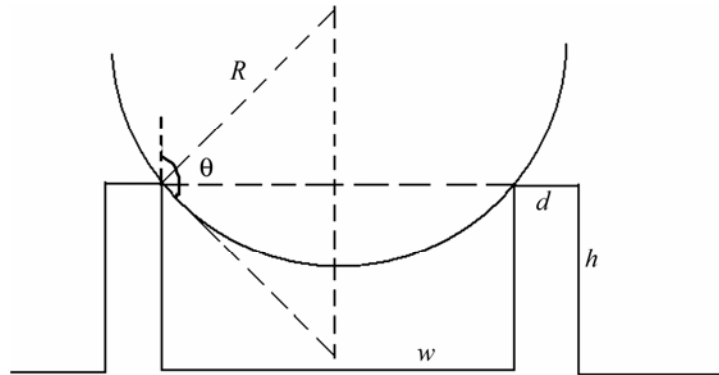

Figure 3. Illustration of air-trapping on a hillock surface.

For a surface with hillock coverage of p, the line coverage is also p. That is, $p=nd/L$, or $1-p=nw/L$ where n is the number of hillocks on a total line length of L. We can therefore obtain

$$w=d(1/p-1) \qquad\qquad\qquad 4$$

By combining Eq. 3 and Eq. 4, we can also obtain the following:

$$\frac{h}{d} \geq \frac{1-\sin\theta}{-2\cos\theta}(\frac{1}{p}-1) \qquad\qquad 5$$

Equation 5 reveals the relation among the three most important process variables of the microparticle based method, particle size (diameter, d), coverage (p) and etching depth (h), which can be reformed as the following equation.

$$\frac{hp}{d(1-p)} \geq \frac{1-\sin\theta}{-2\cos\theta} \qquad\qquad 6$$

Discussion

The terms on the left side of Eq. 6 consist of only surface descriptors and hence process variables and the right side consists of terms only related to contact angle on a flat surface, which depends on interfacial energies. This equation provides a way to establish limits for superhydrophobicity in terms of processing variables of the surface. Experimental data shows the presence of a threshold value of coverage (p) for superhydrophobic behavior and hence occurrence of air-trapping on the hillock surfaces, as shown in Fig. 2. Rewriting Eq. 6 to establish a limit for p yields the following,

$$p \geq (1-\frac{2h\cos\theta}{d(1-\sin\theta)})^{-1} \qquad\qquad 7$$

The effect of aspect ratio and contact angle is plotted in Fig. 4 based on Eq. 7. In general, the threshold value of hillock coverage decreases with the increase of hillock aspect ratio, and increases with the increases of contact angle.

Substituting values of d (20, 10 μm), h (10, 25 μm), and $\theta(109°)$[21,23], which correspond to the experimental conditions as shown in Fig. 2, the threshold values of

coverage p are obtained as shown in Fig. 4. For aspect ratios larger than unity, the calculated threshold value of coverage increases very slowly from 3.2% to 7.7%. They all fall into the observed window of coverage (3% to 18%) where the surfaces lose superhydrophobicity (and hence air-trapping). For an aspect ratio of 0.5 ($d = 20$ μm, $h = 10$ μm), experimental data shows that the transition from hydrophobic (contact angle of 120°) to hydrophobic (contact angle of 78°) lies in the coverage range between 12.5% to 17.9%. The model predicts a threshold coverage value of 14.3%, which aggress reasonably well with the experimental observation. It is important to note that some variation between experimental data and model predictions can be expected since the predicted threshold value of coverage is actually a statistical average. This is because the replacement of w with d using Eq. 4 is only true for the average values of w and d.

The air-trapping criterion can be extended to include statistical roughness parameters of the surface as well. In the authors' previous work, hillock coverage and size have been related to amplitude and spatial statistical roughness parameters of the surface[19], hillock
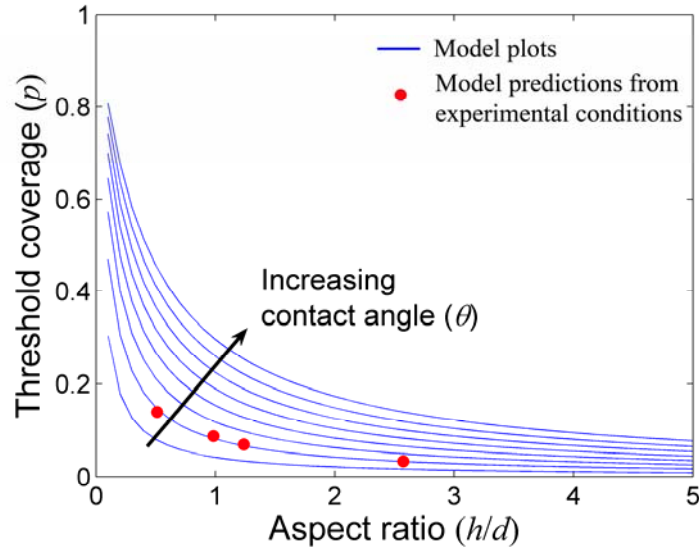
Figure 4. Threshold coverage as a function of aspect ratio (h/d) and contact angle (θ). θ values increase from 100° to 170° in steps of 10°. Experimental data agree reasonably well with model predictions.

width and coverage can be approximately related to autocorrelation length (β) of the hillock surface according to $\beta \approx \dfrac{d}{2p}$. Thus, Equation 5 can be rewritten as a function of p, h and

β as shown in the following equation.

$$\frac{h}{\beta} \geq \frac{1-\sin\theta}{-\cos\theta}(1-p)$$

8

The hillock height and coverage can be related to root mean square (σ) of the hillock surface as well[15], i.e., $\sigma = h\sqrt{p-p^2}$. Thus, Equation 8 can be rewritten as a function of p, β, and σ as shown in the following equation.

$$\frac{\sigma}{\beta} \geq \frac{1-\sin\theta}{-\cos\theta}(1-p)\sqrt{p-p^2} = \frac{1-\sin\theta}{-\cos\theta}(1-\phi_s)\sqrt{\phi_s-\phi_s^2}$$

9

Thus the air-trapping criterion (Eq. 8) is extended to use one amplitude roughness parameter (σ) and one amplitude roughness parameter (β), which are widely used in engineered surface characterization. Equation 9 provides a potential to extend the analysis to rough surfaces with other kinds of structures. Hillock coverage (p) is equal to area fraction ϕ_S in Cassie and Baxter's model. Combining the air-trapping criterion (Eq. 9) with Wenzel's model (Eq. 1) and Cassie and Baxter's model (Eq. 2), we can obtain a complete description of contact angle on rough surfaces. Starting from contact angle on flat surfaces (calculated using Young's equation), the procedure is illustrated in the following Fig. 5.

For hydrophilic surfaces ($\theta < 90^\circ$), the right side of Eq. 9 is negative, which has no physical meaning as a criterion for aspect ratio. It simply means that air-trapping is impossible on hydrophobic surfaces and Wenzel's model should be used directly to evaluate surface roughness effects on observed contact angles. For hydrophobic surfaces ($\theta > 90^\circ$), the criterion can be used to check whether air-trapping is possible, then decide whether Wenzel's model or Cassie and Baxter's model is appropriate as shown in Fig. 5.

It is important to note that satisfying the air-trapping criterion simply means that air-trapping is possible, but whether air-trapping actually occurs and whether contact angle can be calculated using Cassie and Baxter's model also depends on other conditions. For example,
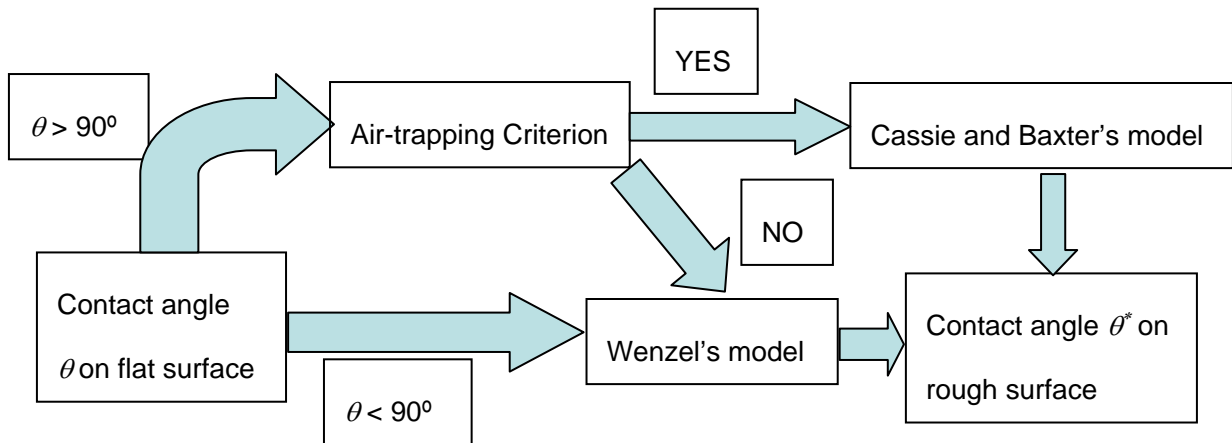
Figure 5. Flow chart for calculating contact angle on rough surfaces based on Young's equation, Wenzel's model, Cassie and Baxter's model, and the developed air-trapping criterion.

air may not be trapped on a surface that satisfies the criterion under external stimulus, like pressure[26]. Also, wetting history may lead to total wetting on superhydrophobic lotus leaves[27]. The same is true for using Wenzel's model on hydrophilic surfaces. A different approach has been reported where it has been argued that self-affine structures can make any substrate with a non-zero microscopic contact angle superhydrophobic[28].

Conclusion

In this paper, a geometric model was developed to related air-trapping ability of hydrophobic surfaces with hillock features to process variables (hillock diameter, etching depth and coverage) and contact angle. The model is shown to be able to predict minimum coverage of hillocks required for air-trapping on hydrophobic rough surfaces. The model predictions agree with experimental observations reasonably well. This model can particularly be extended to utilizing statistical roughness parameters to predict air-trapping for rough hydrophobic surfaces.

Acknowledgements

References

[1]   W. Barthlott and C. Neinhuis, Planta **202,** 1-8 (1997).

[2]   X. J. Feng and L. Jiang, Advanced Materials **18,** 3063-3078 (2006).

[3]   B. N. J. Persson, O. Albohr, U. Tartaglino, A. I. Volokitin, and E. Tosatti, Journal of Physics-Condensed Matter **17,** R1-R62 (2005).

[4]   G. Zhang, D. Y. Wang, Z. Z. Gu, and H. Mohwald, Langmuir **21,** 9143-9148 (2005).

[5]   J. Ji, J. Fu, and J. Shen, Advanced Materials **18,** 1441-1444 (2006).

[6]   S. Wang, L. Feng, and L. Jiang, Advanced Materials **18,** 767-770 (2006).

[7]   N. Zhao, J. Xu, Q. D. Xie, L. H. Weng, X. L. Guo, X. L. Zhang, and L. H. Shi, Macromolecular Rapid Communications **26,** 1075-1080 (2005).

[8]   Q. D. Xie, G. Q. Fan, N. Zhao, X. L. Guo, J. Xu, J. Y. Dong, L. Y. Zhang, Y. J. Zhang, and C. C. Han, Advanced Materials **16,** 1830-+ (2004).

[9]   A. Nakajima, A. Fujishima, K. Hashimoto, and T. Watanabe, Advanced Materials **11,** 1365 (1999).

[10]   L. B. Zhu, Y. H. Xiu, J. W. Xu, P. A. Tamirisa, D. W. Hess, and C. P. Wong, Langmuir **21,** 11208-11212 (2005).

[11] K. K. S. Lau, J. Bico, K. B. K. Teo, M. Chhowalla, G. A. J. Amaratunga, W. I. Milne, G. H. McKinley, and K. K. Gleason, Nano Letters **3,** 1701-1705 (2003).

[12] J. Genzer and K. Efimenko, Science **290,** 2130-2133 (2000).

[13] A. Hozumi and O. Takai, Thin Solid Films **303,** 222-225 (1997).

[14] R. Hatada and K. Baba, Nuclear Instruments & Methods in Physics Research Section B-Beam Interactions with Materials and Atoms **148,** 655-658 (1999).

[15] Y. Zhang and S. Sundararajan, Langmuir in press (2007).

[16] T. Young, Philosophical Transactions of the Royal Society of London **95,** 65-87 (1805).

[17] R. N. Wenzel, Industrial and Engineering Chemistry **28,** 988 (1936).

[18] A. B. D. Cassie and S. Baxter, Transactions of the Faraday Society **40,** 546 (1944).

[19] Y. Zhang and S. Sundararajan, Applied Physics Letters **88,** 141903 (2006).

[20] Y. Zhang and S. Sundararajan, Tribology Letters **23,** 1 (2006).

[21] Y. X. Zhuang and A. Menon, Journal of Vacuum Science & Technology A: Vacuum, Surfaces, and Films **23,** 434-439 (2005).

[22] P. P. Joshi, R. Pulikollu, S. R. Higgins, X. M. Hu, and S. M. Mukhopadhyay, Applied Surface Science **252,** 5676-5686 (2006).

[23] Y. Zhang and S. Sundararajan, submitted to Advanced Materials.

[24] J. Bico, C. Tordeux, and D. Quere, Europhysics Letters **55,** 214-220 (2001).

[25] A. J. Schrauth, N. Saka, and N. P. Suh, in *Development of Nano-Structured Hemocompatible Surfaces*, Daejeon, Korea, Nov. 3-5, 2004.

[26] D. Quere, A. Lafuma, and J. Bico, Nanotechnology **14,** 1109-1112 (2003).

27   Y. T. Cheng and D. E. Rodak, Applied Physics Letters **86** (2005).

28   S. Herminghaus, Europhysics Letters **52,** 165-170 (2000).

CHAPTER 8. CONCLUSIONS AND FUTURE WORK

In this research, the effect of surface roughness on contact and wetting were analyzed and a surface processing technique that can tune surface spatial and amplitude structures was developed. This process was utilized to generate low adhesion surfaces and superhydrophobic surfaces. The significant results of the various research activities are summarized below.

Contact model based on autocorrelation length

Autocorrelation length (ACL) is an important roughness parameter that provides spatial information of surface morphology. Whitehouse and Archard had developed a description of surface peak distribution based on ACL by assuming normal height distribution and exponential form of autocorrelation function. Starting from their analysis, a relation between ACL and real area of contact at low loads was presented based on statistical analysis of surface height data and Hertzian contact mechanics. The analysis showed that a surface with a smaller ACL tends to have more peaks at any given height above the mean line than for surfaces with larger ACLs, and the real area of contact increase with an increase of number of peaks in contact. Thus, surfaces with smaller ACL have a larger real area of contact compared to surfaces with larger ACL under the same contact conditions. This relation was verified by microscale friction data on silicon surfaces exhibiting different values of ACL. The predominant friction mechanism in the tests was adhesive, resulting in the friction force being directly proportional to the real area of contact. Assumptions of normal surface height distribution, elastic contact and constant material shear strength were checked to make sure that experimental conditions satisfy requirements. The data showed that the sample with a lower ACL displayed higher friction behavior than surfaces with higher ACLs. This study showed that ACL can be an effective surface parameter for peak analysis, real area of contact calculation, and adhesive friction force estimation.

Hybrid surface processing

A surface engineering method based on electrostatic deposition of microparticles and dry etching was described and shown to be able to tune both amplitude and spatial roughness parameters of the final surface. Colloidal particles, such as silica spheres in water, often carry electrical charges. By coating a substrate with a monolayer of polymer with opposite charges, colloidal particles could be attached onto the substrate by electrostatic forces. The process of deposition is random and the colloidal particles acted as random masks during subsequent dry etching using RIE or DRIE. The generated surfaces showed randomly distributed hillock features, which were decided by the size, shape and location of colloidal particles. Statistical models were developed to connect process variables to the amplitude roughness parameters center line average, root mean square and the spatial parameter, autocorrelation length of the final surfaces. By modeling the distribution of the particles as a random telegraph signal, an explicit relation between autocorrelation length and the surface coverage of the particles was built. The autocorrelation length of the final surface was found to decrease with an increase in the coverage of particles. Experimental results on silicon surfaces using silica particles were in good agreement with the model. Process variables include particle coverage, which affects both amplitude and spatial roughness parameters, particle size, which affects only spatial parameters and etch depth, which affects only amplitude parameters.

The developed hybrid process was utilized to modify the surface topography of silicon surfaces to reduce adhesion and friction force. Microscale adhesion and friction tests were conducted on flat (smooth) and processed silicon surfaces with a low elastic modulus thermoplastic rubber (Santoprene) probe that allowed a large enough contact area to observe the feature size effect. Both adhesion and friction force of the processed surfaces were reduced comparing to that of the flat surfaces.

Biomimetic superhydrophobic surfaces

The hybrid processing method was used to obtain superhydrophobic engineering materials that mimic the water repellency of naturally occurring surfaces such as the lotus leaf. Colloidal particles with diameter around 20 µm were used to generate microscale roughness; and they also cause electron diffraction to enhance the nanoscale roughness generated on top of the micron-scale features. This kind of binary roughness structures is similar to surface structures of Lotus leaves. Furthermore, the passivation processes during plasma etching produced a hydrophobic fluorocarbon layer on the surface, which is similar to the wax layer on Lotus leaves. The combination of binary roughness structure and fluorocarbon layer showed water contact angles as high as 160º. Particle coverage studies showed is the occurrence of a threshold value (~ 15% coverage) to sustain air trapping under droplets, which is believed to be the mechanism causing the observed superhydrophobic behavior.

In order to model the air-trapping ability using surface roughness parameters, a geometrical restriction for formation of air-trapping was studied on a simplified rough surface model with hillock features. A criterion was given to evaluate whether air-trapping can be formed based on RMS, ACL of rough surfaces, contact angle of liquid on flat surfaces, and hillock coverage, which are generally easy to measure. The criterion worked reasonably well when compared to experimental data.

Suggestions for future work

The research described in this dissertation included both experimental and modeling aspects and there are numerous issues that can be addressed by future work.

On the experimental side, the developed hybrid surface processing technique can be extended to using multi-disperse colloidal particle sizes in single or multiple steps. In this way, multi-scale roughness can be achieved on a given surface. Such a surface is believed to

a good substrate for superhydrophobicity. In addition, a detailed study on the hysteresis of contact angles on such surfaces needs to be determined for self-cleaning applications. New methods to precisely measure real area of contact are also desired so that contact model predictions can be compared with experimental data directly, rather than via friction forces, would also be worth pursuing.

On the theoretical side, the geometrical model for air-trapping can be extended to include force balance, such as the interaction between gravity and surface tension. This will make the model more appropriate for large droplet or fluid applications.

A better description of colloidal clustering is also desired. Based on Poisson point process, clustering can be simulated. Figure 1 shows the simulated clustering using a Matern cluster process[1], and its autocorrelation function is given in Fig. 2. During the simulation, particle size is set to be 1 μm, and particle coverage is around 10%. With the same particle size and coverage, experimental results and the corresponding autocorrelation function are shown in Fig. 3 and Fig. 4. In both simulated and experimental results, autocorrelation function decrease very quickly. In order to obtain a statistical relation between process variables (particle size, coverage and etching depth) and surface roughness parameters, more simulation results are needed. Furthermore, statistical analysis based on Poisson point process will also help develop relations between process variables and roughness parameters.
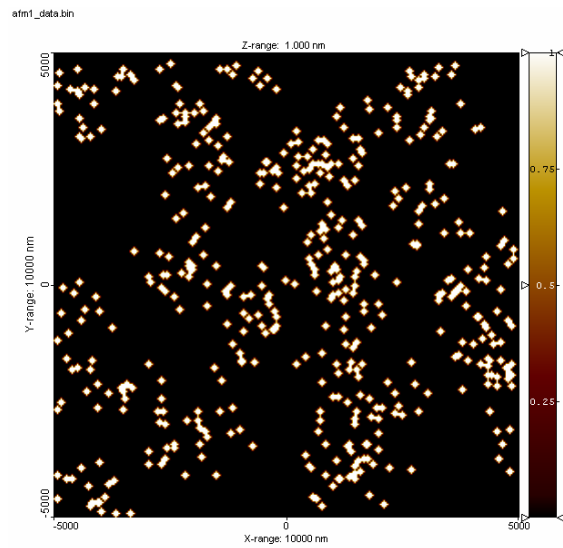
Figure 1. Simulated clustering of colloidal particles using Matern clustering process. Particles size is set to 1 μm and coverage is around 10%.
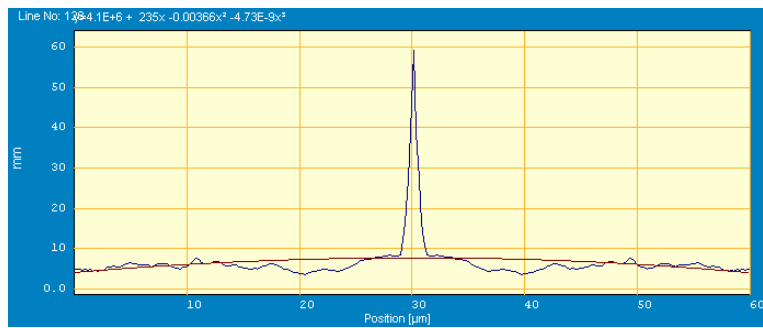

Figure 2. Autocorrelation function of simulated particle clustering in Fig. 1.
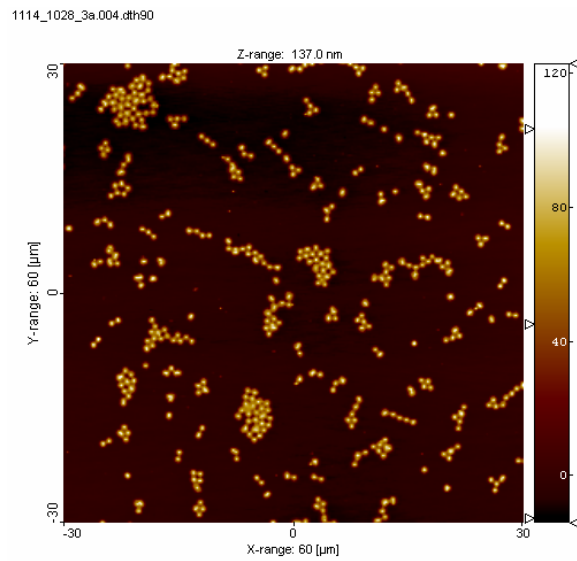
Figure 3. AFM scanning image of colloidal particles. Particles size is 1 μm and coverage is around 10%.
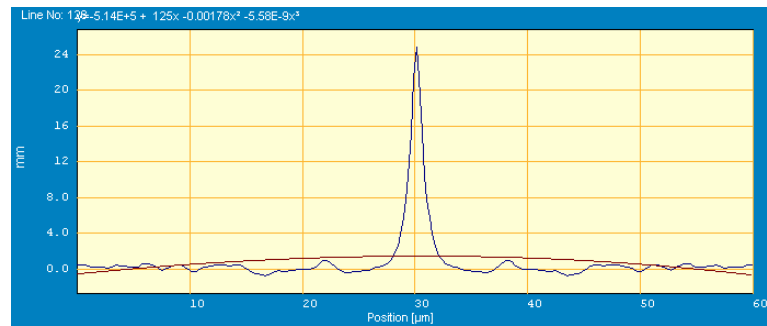

Figure 4. Autocorrelation function of experimental results shown in Fig. 3.

References

1. Adrian Baddeley, et.al, Case Studies in Spatial Point Process Modeling, New York, Springer, 2006

ACKNOWLEDGEMENTS

APPENDIX A. DETIALIED PROCESS METHODOLOGY

The detailed process of the developed hybrid processing is as the following:

1. Surface cleaning. For silicon wafer, ultrasonic cleaning in DI water for 5 minutes could be used, or use the standard wafer cleaning process (http://www.ece.umd.edu/mems/resources/sop/wafer_clean.pdf). Depending on applications, the wafer may be cut to small pieces before cleaning. Those small pieces can be used directly in RIE chamber. For DRIE chamber, those small pieces can be attached to a whole wafer using photoresist.

2. Surface charging. For example, to obtain surface with a negatively charged native oxide layer on silicon wafer, a Piranha etch (3:1 solution of H_2O_2 and H_2SO_4) could be used. The dipping time could be longer than 1 hour and you may want to heat up the solution for better effects. But be careful in handling Piranha and never store them. More details about Piranha are available online, such as http://www.bold-tech.com/technical/ piranha_etch.html.

3. Polymer coating. A poly (diallyldimethyl ammonium) chloride (PDDA) monolayer was deposited via dip coating to form a uniformly polycationic layer. This positively charged monolayer will attract negatively charged colloidal particles. The PDDA solution is used as purchased from Sigma-Aldrich. The dipping time may vary from 30 seconds to several minutes and 1 minute will be a good starting point for further refining.

4. Colloidal preparation. Silica spheres were mixed with MilliQ water and sonicated for 20 min to form a colloidal solution into which the silicon substrate is immersed. The concentration of colloidal could be varied from several mg/mL to several tens mg/mL.

5. Immersion. Put negatively charged silicon samples into the colloidal. The negatively charged silica particles are randomly attracted to the positively charged PDDA

monolayer on the silicon surface. The coverage of particles on the substrate was varied by controlling the immersion time. It may be needed to try several times to identify appropriate time for the desired coverage.

6. Rinse. After immersion, the samples were rinsed in MilliQ water flow for 5 min to remove loosely held silica particles and then dried in clean nitrogen flow to ensure that a monolayer of randomly dispersed particles remained on the PDDA coated surface. For large colloidal particles, please leave the sample into a hot oven and do not use the nitrogen gun, which will blow away particles.

7. Dry etching. Samples were dry etched in a reactive ion etch (RIE) or DRIE chamber. Etching time depends on the desired etching depth. For etching depth larger than 5 μm, only DRIE will work. During this line-of- sight etching process, particles act as temporary masks that result in "hillock-like" features on the substrate. The etching speed is around two hundred nm/hour for RIE, and one μm/min for DRIE.

8. Cleaning. After dry etching, the remaining silica particles were then removed using 49% or diluted hydrofluoric (HF) acid followed by DI water rinsing for at least 5 min. Be very careful with HF acid and take the safety training class before handling HF, which is required by I.S.U..

APPENDIX B. MATLAB CODES

Countourplot: This code calculates the average ACL in all directions on the auto correlation plot obtained from SPIP. It was used in APL paper.

```
%fid=fopen('c:\Image_data.dat'); %open file
[filename,pathname]=uigetfile('*.dat');
fid=fopen(fullfile(pathname,filename));
a=fread(fid,inf,'float');
fclose(fid);
n=sqrt(length(a));%resolution=256
l=10;%scan size=10um

%Zcontour=max(a)-(max(a)-min(a))/2.71828;
Zcontour=max(a)/2.71828;%ACL definition
Z=reshape(a,[n,n]);
%[X,Y]=meshgrid(1:1:256,1:1:256);
%[C,h] = contour(X,Y,Z,[Zcontour,Zcontour]);
[C,h]=contour(Z,[Zcontour,Zcontour]);
int i;
i=1;
while i<=C(2)
    X(i)=C(2*i+1);
    Y(i)=C(2*i+2);
    R(i)=sqrt(X(i)^2+Y(i)^2);%ACL for (X,Y)(i)
    i=i+1;
```

```
        end

        ACL=sqrt(polyarea(X,Y)/pi)*l/n  %scan size is 10um, resolution is 256

        fid=fopen('C:\ACL report.txt','a');

        fprintf(fid,'\n');

        fprintf(fid,filename);

        fprintf(fid,': %f \n',ACL);

        fclose(fid);


        %set(h,'ShowText','on','TextStep',get(h,'LevelStep')*2)

        %colormap cool
```

Realcontactarea: Calculated relation between real area of contact and normal load based on peak distribution function given by Whitehouse and Archard.

```
% assume the same peak radius and fixed ACL
clear
P=1;
R=1;
E=1;
Lscan=10;%scan length (um)
lambda=1;%ACL


ACL=[0.1,1,10,20,50];%first value is the comparing standard
rou=exp(-1./ACL);%peak radius
low=4:-.01:0;
%rou=0:.01:1;
```

```
for j=1:length(rou)

    F=@(y)1/4/sqrt(2*pi)*(1.+erf(y./sqrt(2)*sqrt((1-rou(j))/(1+rou(j))))).^2.*exp(-.5.*y.^2);

%peak distribution

    for i=1:length(low)

    k=i+(j-1)*length(low);

    %N(k)=1/pi*atan(sqrt((3-rou(j))/(1+rou(j))));

    %N(k)=1;

    %Cbar(k)=(3-rou(j))*(1-rou(j))^(1/3)/2/N(k)/sqrt(pi());

    %Cbar(k)=1;

    %F=@(y)1/(1/pi*atan((3-rou(j))/(1+rou(j)))^.5)/(4*sqrt(2*pi))*(1.+erf(y./sqrt(2).*sqrt((1-
rou(j))/(1+rou(j))))).^2.*exp(-.5.*y.^2);

    Q(k) = quad(F,low(i),100);%integrate above low(i)

    if i==1

        Ncontact(k)=Q(k); %number of peaks in contact

    else

        Ncontact(k)=Q(k)-Q(k-1);

    end

end

end


%calculate real area of contact at different cascade level, i.e., ncontact


%calculate loads at every cscade level i: Pload(i)

for i=1:length(low)*length(rou)

    Pload(i)=0;

    Ncascade(i)=0;
```

```
    Arac(i)=0;
end


%calculate number of contact points at every casade level for every ACL
for j=1:length(rou)
    for i=1:length(low)
        Ncascade(i)=i;
    k=i+(j-1)*length(low);
    for l=(j-1)*length(low)+1:k
    Pload(k)=(k-l+1)^(1.5)*Ncontact(l)+Pload(k);
    end
    RPload(k)=Pload(k);
    end
end


for j=2:length(rou)
    for i=1:length(low)
    k=i+(j-1)*length(low);
    for l=1:length(low)
    if Ncascade(k)==0 & Pload(k)<=Pload(l)
        Ncascade(k)=l;
        RPload(k)=Pload(l);
    end
    end
    end
end
```

```
%calculate real area of contact

for j=1:length(rou)

    for i=1:length(low)

    k=i+(j-1)*length(low);

    for l=(j-1)*length(low)+1:(j-1)*length(low)+Ncascade(k)

    Arac(k)=(k-l+1)*Ncontact(l)+Arac(k);

    end

    end

end

Arac=Arac*pi*(3*P*R/4/E*sqrt(Lscan/lambda))^(2/3);


for i=1:length(ACL)

    for j=1:length(low)

    if Pload((i-1)*length(low)+j)<minload

        PPload(j)=Pload((i-1)*length(low)+j);

        A(j)=Arac((i-1)*length(low)+j);

    end

    end

    plot(PPload,A);

    hold on

end

xlabel('Normalized load, P/(4/3E^*R^{1/2}\sigma^{3/2})')

ylabel('Normalized real area of contact, A/(R\sigma)')

hold off
```